8-2016

Materials design and band gap engineering of complex nanostructures using a semi-empirical approach : low dimensional boron nanostructures, h-BN sheet with graphene domains and holey graphene.

Cherno Baba Kah

MATERIALS DESIGN AND BAND GAP ENGINEERING OF COMPLEX
NANOSTRUCTURES USING A SEMI- EMPIRICAL APPROACH: LOW
DIMENSIONAL BORON NANOSTRUCTURES' h - BN SHEET WITH GRAPHENE
DOMAINS AND HOLEY GRAPHENE

By

Cherno Baba Kah
M.S, University of Louisville, 2013
M.S, Clark Atlanta University, 2011
B.S, University of The Gambia, 2009

A Dissertation
Submitted to the Faculty of the
College of Arts and Sciences of the University of Louisville
in Partial Fulfillment of the Requirements
for the Degree of

Doctor of Philosophy
in Physics

Department of Physics and Astronomy
University of Louisville
Louisville, Kentucky

August 2016

MATERIALS DESIGN AND BAND GAP ENGINEERING OF COMPLEX
NANOSTRUCTURES USING A SEMI-EMPIRICAL APPROACH: LOW
DIMENSIONAL BORON NANOSTRUCTURES, h-BN SHEET WITH GRAPHENE
DOMAINS AND HOLEY GRAPHENE

By

Cherno Baba Kah
M.S, University of Louisville, 2013
M.S, Clark Atlanta University, 2011
B.S, University of The Gambia, 2009

A Dissertation approved on

July 20, 2016

by the following Dissertation Committee:

_____
Dr. Ming Yu (Dissertation Director)

_____
Dr. Chakram S. Jayanthi

_____
Dr. Gamini Sumanasekera

_____
Dr. Xiao-An Fu

DEDICATION

This dissertation is dedicated to the loving memories of my parents Al Hadji Mbackeh Kah

and Adji Isatou Jallow for all their sacrifice and guidance during the short time they lived

with us and for teaching us to believe and trust in Allah, as well as to always work hard to

achieve success.

This is also dedicated to my newly born daughter Adji Aissatou (I can't wait to hold

you in my arms); may you live a successful life full of blessings and in line with the

teachings of the Prophet Muhammad (SAW).

ACKNOWLEDGMENTS

ABSTRACT

MATERIALS DESIGN AND BAND GAP ENGINEERING OF COMPLEX
NANOSTRUCTURES USING A SEMI-EMPIRICAL APPROACH: LOW
DIMENSIONAL BORON NANOSTRUCTURES, h-BN SHEET WITH GRAPHENE
DOMAINS AND HOLEY GRAPHENE

Cherno Baba Kah

July 20, 2016

This dissertation will explore the potential of a semi-empirical Hamiltonian, developed by the research group at the University of Louisville, in predicting the existence of new families of low-dimensional boron nanostructures based on icosahedral α-B_{12} clusters, and in tuning the band gaps of h-BN sheets with graphene domains and holey graphene. This semi-empirical Hamiltonian models electron-electron and electron-ion interactions using environment-dependent (ED) functions, and ion-ion interactions via usual pairwise terms. Additional features of our approach are that it uses a linear combination of atomic orbitals (LCAO) framework to describe the Hamiltonian and it calculates the charge distribution around a site self-consistently (SC). Throughout this dissertation, we will refer this semi-empirical Hamiltonian using the acronym SCED-LCAO.

Our first application on boron nanostructures using SCED-LCAO revealed that one and two-dimensional nanostructures (referred as α, δ_4 and δ_6 sheets) based on icosahedral α-B_{12} clusters were structurally stable. A relative stability with respect to δ_6 was also

determined for the two-dimensional sheets with the strength of the stability in the order of $\delta_4 < \alpha < \delta_6$. The infinite one-dimensional chain (which is the least stable among the low dimensional Boron structures predicted) as well as δ_4 and δ_6 sheets are found to have semiconducting properties while α sheet has metallic properties.

With recent reports on the synthesis of an ultra-thin layer of α-tetragonal B_{50} structure, we delved into a second project that focused on investigating the structural stabilities and properties of a single layer of α-tetragonal B_{50}. We found that, the α-tetragonal B_{50} does not keep its two-dimensional nature but prefers to exhibit symmetry breaking. Our prediction is inconsistent with experimental observations but this may be due to experiments discerning double or multi-layer structures of α-tetragonal B_{50}. We note that the stability of multi-layer α-tetragonal B_{50} structure requires further investigation.

A third application studied includes the band gap engineering on h-BN sheet by creating in it graphene domains of different shapes (triangular, circular, hexagonal and rectangular) and sizes with the aim of reducing the energy gap of pristine h-BN. For this project, the parametrization of the SCED-LCAO Hamiltonian corresponding to the nitrogen element was developed as a first step towards the investigation of pristine h-BN sheets and h-BN sheets embedded with graphene domains. The results of our study of h-BN sheets embedded with graphene domains reveal that the density of states are dependent on the shapes and sizes of the graphene domains and that hexagonal and circular graphene domains are good candidates for engineering the gap of a pristine h-BN sheet.

A fourth application of SCED-LCAO method focused on a study of the band gap of holey graphene sheets, *i.e.,* graphene sheets carved with different types of geometrical

holes. We found holey triangular graphene sheets to have the smallest possible energy gap with its biggest size being the most stable and having $0.11\ eV$ for gap. Holey circular graphene sheet has also a stable structure with a possible gap of $0.35\ eV$ while the most stable structure among the holey rectangular sheets was found to have a gap of $0.4\ eV$.

Computational studies undertaken in this dissertation demonstrate that the SCED-LCAO method is a powerful technique for designing materials with desired properties, which can guide the experimentalists to synthesize novel complex materials. The novel structures and properties predicted in this work for boron icosahedra chains and sheets, holey graphene sheets and h-BN with graphene domains await experimental confirmation.

TABLE OF CONTENTS

LIST OF TABLES

LIST OF FIGURES

xiv

CHAPTER I
INTRODUCTION

This dissertation will focus mainly on structural and electronic properties of low-dimensional materials, mostly, one- and two-dimensional materials. The electronic and transport properties often undergo drastic changes, and new phenomena emerge, when the system is reduced in size (from 3D to 2D, 1D, or 0D). This is because quantum confinement of electrons occurs in one or two dimensions. These reduced-dimensional systems and nanostructures manifest interesting physical properties and phenomena, which are beginning to spur interesting nanoscale device applications.

There has been tremendous progress in synthesizing low-dimensional materials. Atomically thin quasi-2D materials have been created by mechanical exfoliation or other techniques such as molecular beam epitaxy, chemical vapor deposition (CVD), etc. Examples of 2D or quasi-2D materials that have already been synthesized include graphene, few-layer crystals of hexagonal BN, transition metal dichalcogenides, phosphorene, etc. Unlike graphene, these 2D materials can be semiconductors or good metals.

Computational studies have kept pace with these developments, providing valuable physical insights at the microscopic level. Often, computational studies have also paved the way to experimental discoveries. In order for computational studies to be predictive, it is important to describe interactions present in the system accurately. The structure and

properties of condensed matter systems are usually dictated by the outer valence electrons of its constituent atoms. The mutual interactions of these electrons and their interactions with the ions determine the electronic structure of the system, which in turn determines many of the properties of the material. Understanding material properties from first principles involves solving an interacting quantum many-body Hamiltonian. The exact solutions to the quantum many-body Hamiltonian are impracticable. A particular formalism, called Density Functional Theory (DFT) [1], for solving this many-electron problem in an ab-initio fashion has become a method of choice for determining the electronic ground state of the system. This formalism transforms the many-electron problem to one of a self-consistent field one-particle problem for ground-state properties. While DFT methods is reliable for predicting ground state structures of systems, one limitation of this method is that it is computationally expensive to deal with nanoscale systems containing thousands of atoms. Therefore, semi-empirical methods that mimic DFT based methods have become the method of choice for studying large-sized nanostructures, containing thousands of atoms, and low-dimensional systems with reduced symmetries.

There are several flavors of semi-empirical methods that are loosely referred as "tight-binding" methods. One common feature of all tight-binding methods is that they use atomic-like states or linear combination of atomic orbitals as the framework to describe the interaction Hamiltonian with the matrix elements of this interaction Hamiltonian parameterized (hence the name "semi-empirical"). Additionally, a tight-binding method can use an orthogonal or a non-orthogonal basis set to describe its Hamiltonian. Within the non-orthogonal tight-binding schemes, some methods will have the overlap functions

calculated in a given basis set ("Gaussian", "fire-ball", etc.) or modeled via cleverly chosen functions.

The particular flavor of the tight-binding or semi-empirical approach used in this dissertation is called as the Self-Consistent Environment-Dependent LCAO (linear combination of atomic orbitals) [2-4]. The details of this formalism will be developed in full glory in chapter 2 of this dissertation.

Recent advances in nanoscale characterization and device fabrications, in particular, the groundbreaking experiments regarding the two-dimensional material graphene [5], have opened up new opportunities for 2D materials in nanoelectronics and optoelectronics. 2D atomic layered materials, which possess a high degree of anisotropy with nanoscale thickness (*e.g.*, one or a few atomic layers) and infinite length in other dimensions, hold enormous promise as a novel class of ultrathin 2D materials with various unique properties, and hence exhibit great potential as lithographic nanoelectronics devices and conversion systems that are substantially different from their respective 3D bulk forms. The most widely studied atomic layered 2D nanomaterial is graphene, a single layer of carbon atoms only one atom thick and packed in a hexagonal lattice. Graphene exhibits exceptional strength and possesses extraordinary electronic properties. Its electronic, thermal, and mechanical properties make it attractive for a variety of potential applications. However, graphene lacks a band gap that is essential for many electronic applications. Thus, researchers have been struggling to build electronic circuits beyond graphene. In the process of searching 2D nanostructures beyond the graphene, interesting questions have been raised as to whether other pure 2D materials with band gaps exist or the combination of the graphene with other 2D materials can open up the band gap of graphene and whether

its band gap can be tuned further? Encouraged by such exciting challenges, my research efforts for the doctoral dissertation focused on the following projects: (i) predicting novel forms of 2D Boron nanostructures, (ii) assessing whether the band gap of *h*-BN sheet, which is a wide-band gap semiconductor with 5 eV gap, can be tuned by inserting graphene domains, and, finally, whether band gap in graphene sheet can be opened up through functionalization or considering holey graphene sheets.

The reason why we are interested in searching new boron 2D materials is because of the different polymorphic structures exhibited by bulk boron that contain 12-atom cage structures arranged in the form of an icosahedron in its building block. Boron, being an electron deficient element, it forms both localized two-center-two-electron bonds (2c-2e) and three-center-two-electron bonds (3c-3e) that result in both planar and quasi-planar atomic clusters. While there have been several theoretical studies on 2D boron sheets containing elemental boron, in this work, we will be investigating 2D boron sheets that contain icosahedral B_{12} clusters as their building unit.

Previous studies of two-dimensional monolayer structures of boron have predicted a variety of structures (α', β_1, β_2, β_3, δ_5, δ_6). The α' structure in ref. [6] was found to have the highest cohesive energy compared to other boron sheets and it possesses semiconducting properties but it is structurally slightly buckled. It was obtained from further relaxation of another α structure in ref. [7] with high cohesive energy (i.e., an unstable structure with negative phonon frequencies). Another predicted monolayer of boron structure is β_1 with the second highest cohesive energy and flat structure; this structure was found to have metallic properties. In the work cited in ref. [6] other monolayer sheets of boron were predicted such as β_2 and β_3 which were buckled with

metallic properties, δ_6 which is a stable buckled triangular sheet and δ_5 with the highest cohesive energy among δ sheets and is planar. These theoretically predicted Boron 2D monolayer structures, however, have not been synthesized successfully so far, mostly due to complicated chemical bonding nature when the boron atoms aggregate to form infinite 2D and 3D structures.

In our proposed project, we considered alternative strategies in searching the new Boron 2D materials. We are looking for the existence of other types of low dimensional structures based on the icosahedral B_{12} cluster using the robust parameters obtained for the Boron SCED-LCAO Hamiltonian [4]. Our motivation is based on the fact that the Boron crystalline structures are the most stable structures among boron allotropes and the icosahedral B_{12} cluster is the building block of the crystalline structures [8]. For instance, a linear or planar directional cut of the α-Boron structure will result in a one-dimensional or two-dimensional structure based on the icosahedral B_{12}. Three different two-dimensional icosahedral α-B_{12} based structures, referred as α, δ_4 and δ_6, were found to be structurally stable with δ_4 and δ_6 to be semiconductors and α to be metallic. To validate our results for both infinite and two-dimensional α-B_{12} sheet, first-principles DFT with (Vienna Ab-initio Simulation Package – VASP) [9] package is used.

An ultrathin single-crystalline Boron nanostructure has recently been successfully synthesized [10]. High-resolution TEM and the selected-area electron diffraction pattern have demonstrated that the single-crystalline structure is like a few layered tetragonal α-B_{50} film. Motivated by this new discovery, we investigated the existence and the stability of a single-layered tetragonal α-B_{50}. The semi-empirical SCED-LCAO method and the DFT method with two different pseudopotentials (e.g., ultra-soft and PAW) were used. It

was observed that irrespective of the method and size of the supercell used, the single layered tetragonal α-B_{50} sheet has a symmetry breaking due to distortion of some of the icosahedral B_{12} and is slightly a buckled sheet. By examining the bulk structure of tetragonal α-B_{50}, we understood that due to the presence of a single Boron atom with dangling bonds on the surface, the possible stability of the structure might indeed be questioned. We propose that two or multi-layers of α-tetragonal B_{50} will be more stable, but that requires further investigation and a preliminary result will be reported in this dissertation.

The reason why we are interested in engineering the band gap by inserting graphene domain in the h-BN sheet is because h-BN and graphene are known to have similar structural properties, but quite different electronic properties. The h-BN sheet has a wide band gap of about 5 eV while, graphene is a gapless material. The combination of the two types of structures is expected to give rise to new types of hybridization and also complementary electronic properties. Recent experimental results showed that synthesized 2D hybrid structures of boron nitride and graphene domains reveal the optical gap narrowed to ~1.62 eV, as the carbon content in the hybrid BNC sheet increased to an atomic percent of 65% [11]. This experiment demonstrates that by controlling the domain size of graphene domains, one can tune the energy gap in a hybrid BNC sheet composed of BN and graphene domains. Motivated by these experimental observations, I systematically study the band gap narrowing by embedding the graphene domains in the h-BN sheet with different shapes and sizes. The nitrogen parameters developed for SCED-LCAO Hamiltonian were used for the band gap engineering of h-BN sheet with the graphene domains. Different studies have also been carried out on how to open the gap of a graphene

sheet. Part of such studies are done on porous graphene materials such as graphene nanomesh [12, 13] which can be used in supercapacitors, crumpled graphene [14] which can be used in the diffusion or transport of electrons during a rapid charge or discharge process, and the graphene foam [14] which can be used for energy storage as in batteries. Motivated by these results, I have systematically investigated how to open the gap in graphene by creating holes of triangular, circular and rectangular shapes with different sizes on a graphene sheet, and the effect of these hole structures on the band gap of graphene.

The organization of this dissertation is as follows. Chapter II will provide a detailed account of the formalism behind our semi-empirical approach and the functional forms of various interaction terms present in our self-consistent and environment-dependent LCAO Hamiltonian. We will also discuss in detail how to obtain optimized parameters of the SCED-LCAO Hamiltonian for several group III and IV elements of the periodic table. Chapter 3 will discuss the application of SCED-LCAO to boron based system. In this chapter, we will use SCED-LCAO to predict the existence of low dimensional boron nanostructures with icosahedral B_{12} cluster as building units. Our results will be validated using a DFT package (VASP). Chapter IV describes the parameterized SCED-LCAO Hamiltonian for nitrogen using different strategies. The first strategy involves determining optimized parameters of the SCED-LCAO Hamiltonian for nitrogen using a database containing B_nN_m and C_nN_m clusters, while the second strategy uses a database containing Ga_nN_m clusters. A third strategy contained an expanded database containing all three sets of clusters, namely, B_nN_m, C_nN_m and Ga_nN_m. Three different sets of parameters were obtained for the SCED-LCAO Hamiltonian corresponding to nitrogen. The robustness of

these parameterized SCED-LCAO Hamiltonian containing nitrogen elements was tested by performing computational studies of h-BN sheet, w-BN bulk and w-GaN bulk. In chapter V, we study the band gap engineering of functionalized h-BN sheets with carbon domains and graphene sheets carved with holes of different shapes and sizes ("holey graphene"). In the concluding chapter, we highlight the major results obtained in this work and offer suggestions for future work.

CHAPTER II

METHODOLOGY

2.1 Quantum Mechanics based simulations.

In the field of material sciences, computational based methods have been used extensively for the study and understanding of the structures as well as electronic properties of different materials. Based on the sizes or expensiveness in terms of time and memory, different methods of quantum mechanics based simulations have been developed mainly including the first principles which is either wavefunction based ab-initio methods (mostly used in quantum chemistry) or the charge density based density functional theory (DFT) methods (used in both quantum chemistry and condensed matter physics) [3] and semi-empirical simulations methods either orthogonal or non-orthogonal tight binding. The first principles based molecular dynamics simulation methods have the particularity of been accurate or reliable but can handle a limited size of structures, between tens of atoms in ab-initio based methods and not more than hundreds of atoms in a given system when using DFT based methods. The simulation time in first-principles methods is usually in the order of a few picoseconds (ps). The first-principles methods also have rather good predictive power that is they have the ability of determining structural and electronic properties of unknown materials and they can also reproduce results from other methods of calculations or properties of materials already synthesized. Disadvantages or limitations of first-principles methods are, they are slow even though accurate, the methods require very large

computational time and memory and more importantly these methods cannot be used for very large systems like complex chemical reactions, biological systems and nanostructures with low or no symmetry [2].

In contrast to the first-principles simulations based methods, the semi-empirical simulations methods have the capacity of handling large or very big sizes of materials, in the order of tens of thousands of atoms with a simulation time of a few nanoseconds (ns) but they are not easily transferable. Namely, the conditions or parameters sets for a given system can only be used for that specific system, and if a new material is to be considered, one will have to create new sets of conditions or parameters. Thus, such semi-empirical methods have limited predictive power. Disadvantages of such semi-empirical methods or traditional non-orthogonal tight binding methods are due to that (1) only two-center interactions were included within the calculations for a given system, and (2) the charge redistribution within the systems under considerations is also calculated using such semi-empirical methods without self-consistency consideration.

2.2 Why SCED-LCAO?

As stated in section 2.1, the traditional non-orthogonal tight binding (TB) methods have limited transferability due to the fact that only two-center interactions are included in their calculations and also the charge redistributions is not done using self-consistency [2]. A number of solutions have been proposed to improve the transferability and at the same time include self-consistency and or environment-dependency [2]. In some of these newly developed methods, such as in a self-consistent charge density-functional based tight-binding method (DFTB) developed by Frauenheim T, et al. [15] for predictive materials

simulations in physics, chemistry and biology, the charge redistribution is calculated using self-consistency through an eigenvalue equation with a Hamiltonian having a two-center interaction term. But in this method, the environment dependency which is necessary in having a transferable Hamiltonian is only considered if the systems have charge fluctuations. But if no charge fluctuation is involved, the environment dependency term disappears making it not totally transferable. Hence the Condensed Matter Theory (CMT) group of the University of Louisville thought it necessary to develop a semi-empirical method that would be accurate, fast, reliable, robust, and transferable and also has a predictive power and can handle large systems of atoms. The Self-Consistent and Environment-Dependent Hamiltonian within the framework of the Linear Combination of Atomic Orbitals or SCED-LCAO Hamiltonian was therefore proposed [2-4]. The particularity of this method is that the charge redistribution is calculated using self-consistency and also not only two-center interactions are considered within its Environment-Dependent term but multi-center interactions as in electron-electron, electron-ion and ion-ion interactions are also considered. The electrons screening effects are therefore considered during simulations. A thorough optimization and robust testing of parameters for SCED-LCAO Hamiltonian ensures its transferability. SCED-LCAO Hamiltonian is expected to not only solve the issues or shortcomings of traditional non-orthogonal tight binding methods by calculating charge redistribution through self-consistency and at the same time take care of environment dependency but it is also expected to overcome limitations in terms of size and time mentioned in first-principle methods [3].

2.3 Detailed discussion about SCED-LCAO.

By definition, we know that the many-body Hamiltonian is given as:

$$H = -\sum_l \frac{\hbar^2}{2m} \nabla_l^2 - \sum_i \frac{\hbar^2}{2M_i} \nabla_i^2 + \sum_{l,i} v(\vec{r}_l - \vec{R}_i) + \sum_{l,l'} \frac{e^2}{4\pi\epsilon_0 r_{ll'}} + \sum_{i,j} \frac{Z_i Z_j e^2}{4\pi\epsilon_0 R_{ij}}$$ (1)

where $ll' = \vec{r}_l - \vec{r}_{l'}$; $R_{ij} = \vec{R}_i - \vec{R}_j$; $v(\vec{r}_l - \vec{R}_i)$ is the potential between an electron at site $\vec{r}_l$ and an ion at site $\vec{R}_i$ and Z_i is the number of valence electrons associated with the ion at site $\vec{R}_i$. The solutions for this many-body Hamiltonian are rather impracticable hence the need was felt to simplify the expression of the Hamiltonian to a single self-consistent one electron problem for the ground state properties.

$$H = -\frac{\hbar^2}{2m} \nabla^2 + V_{eff}$$ (2)

where V_{eff} is defined as the effective potential and, in the first-principles methods of simulations the effective potential is express within the Kohn-Sham [1] approximation as:

$$V_{eff}^{KS} = V(\vec{r}) + e^2 \int \frac{n(\vec{r}\prime)}{|\vec{r} - \vec{r}\prime|} d\vec{r} + \frac{\delta}{\delta n(\vec{r})} E^{XC}[n(\vec{r})]$$ (3)

with the exchange correlation energy E^{XC} being a functional of the charge density $n(\vec{r})$. In the semi-empirical methods of quantum mechanics based simulations however, the effective potential is expressed in terms of defined parameters. All these methods of calculations use atomic-like states or the linear combinations of atomic orbitals (equation 4) as a framework to describe the interaction of the Hamiltonian with the matrix elements.

$$|\psi_\lambda(\vec{r})\rangle = \sum_i \sum_\alpha C_{i\alpha} |\varphi_\alpha(\vec{r} - \vec{R}_i)\rangle$$ (4)

The general eigenvalue problem intended to be solved is:

$$\hat{H}|\psi_\lambda(\vec{r})\rangle = \epsilon_\lambda |\psi_\lambda(\vec{r})\rangle$$ (5.1)

$$\langle\varphi_{i\alpha}|\hat{H}|\varphi_{j\beta}\rangle C_{i\alpha}^\lambda = \epsilon_\lambda C_{i\alpha}^\lambda \langle\varphi_{i\alpha}|\varphi_{j\beta}\rangle$$ (5.2)

or

$$\langle\varphi_{i\alpha}|\hat{H}|\varphi_{j\beta}\rangle C_{i\alpha}^{\lambda} = \epsilon_{\lambda}C_{i\alpha}^{\lambda}S_{i\alpha,j\beta} \qquad (5.3)$$

In the new generation of SCED-LCAO [4] the Hamiltonian is defined in terms of parametrized matrix elements with its diagonal and off diagonal elements being respectively:

$$\hat{H}_{i\alpha,i\alpha} = \varepsilon_{i\alpha} + \sum_{k\neq i}W_{i\alpha}(R_{ik}) + (N_i - Z_i)U_i + \sum_{k\neq i}\{N_kV_N(R_{ik}) - Z_kV_z(R_{ik})\} \quad (6.1)$$

$$\hat{H}_{i\alpha,j\beta} = \frac{1}{2}\left[\varepsilon'_{i\alpha} + \varepsilon'_{j\beta}\right]K(R_{ij})S_{i\alpha,j\beta}(R_{ij}) + \frac{1}{2}\left[\sum_{k\neq i}W_{i\alpha}(R_{ik}) + \right.$$

$$\left.\sum_{k\neq j}W_{j\beta}(R_{jk})\right]K(R_{ij})S_{i\alpha,j\beta}(R_{ij}) + \frac{1}{2}\left[(N_i - Z_i)U_i + (N_j - Z_j)U_j\right]S_{i\alpha,j\beta}(R_{ij}) +$$

$$\frac{1}{2}\left[\sum_{k\neq i}\{N_kV_N(R_{ik}) - Z_kV_z(R_{ik})\} + \sum_{k\neq j}\{N_kV_N(R_{jk}) - Z_kV_z(R_{jk})\}\right]S_{i\alpha,j\beta}(R_{ij}) \quad (6.2)$$

The Hückel energies terms $\varepsilon'_{i\alpha}$ and $\varepsilon'_{j\beta}$ in equation 6.2 are adjustable parameters. The first term (in between square brackets) in the expression of the off-diagonal matrix elements of the Hamiltonian (equation 6.2) includes the two-center interaction term followed by the expression with the W term that takes into account the possible occupation of the excited local orbitals in an atomic aggregation and therefore, the effects of interactions with neighboring atoms. The on-site electron-electron interactions both in equation 6.1 (third term) and equation 6.2 (third term in between square brackets) provide the framework for the charge redistribution calculation and the fourth terms for both equations 6.1 and 6.2 take care of the environment dependence and multicenter interactions also called the environment dependent term defined by the different potential functions V_N and V_Z.

As already mentioned, the particularity of the SCED-LCAO is its ability to calculate the charge redistribution through self-consistency. The self-consistency is

determined through the eigenvalue problem stated in equation 5.2. Following the construction of the SCED-LCAO Hamiltonian with the different parameters, the general eigenvalue problem will be solved for this Hamiltonian as in equation 7.

$$\langle \varphi_{i\alpha} | \widehat{H} | \varphi_{j\beta} \rangle = H_{i\alpha,j\beta}^{SCED-LCAO}\left(N_i, N_j, \{V_{ki}^N\}, \{V_{kj}^N\}, \{V_{ki}^z\}, \{V_{kj}^z\}\right) \tag{7}$$

The charge projected on each site will be obtained from the solution of the eigenvalue problem (Eq. (8)) and will be inserted back in the eigenvalue equation via Eq. (7).

$$N_i = \sum_{\lambda}^{occ} \sum_{\alpha} \sum_{j\beta} C_{i\alpha}^{\lambda} C_{j\beta}^{\lambda} n_{\lambda} S_{i\alpha,j\beta} \tag{8}$$

The cycle repeated until the self-consistency is reached between the input and output charges. In summary the self-consistency calculation can be described by:

$$\langle \varphi_{i\alpha} | \widehat{H} | \varphi_{j\beta} \rangle C_{i\alpha}^{\lambda} = \epsilon_{\lambda} C_{i\alpha}^{\lambda} \langle \varphi_{i\alpha} | \varphi_{j\beta} \rangle \qquad \longrightarrow \qquad N_i = \sum_{\lambda}^{occ} \sum_{\alpha} \sum_{j\beta} C_{i\alpha}^{\lambda} C_{j\beta}^{\lambda} n_{\lambda} S_{i\alpha,j\beta}$$

$$N_i^{in} \Leftrightarrow N_i^{out}$$

N_i^{in} is the input number of valence electrons at a site i

$$\langle \varphi_{i\alpha} | \widehat{H} | \varphi_{j\beta} \rangle = H_{i\alpha,j\beta}^{SCED-LCAO}\left(N_i, N_j, \{V_{ki}^N\}, \{V_{kj}^N\}, \{V_{ki}^z\}, \{V_{kj}^z\}\right)$$
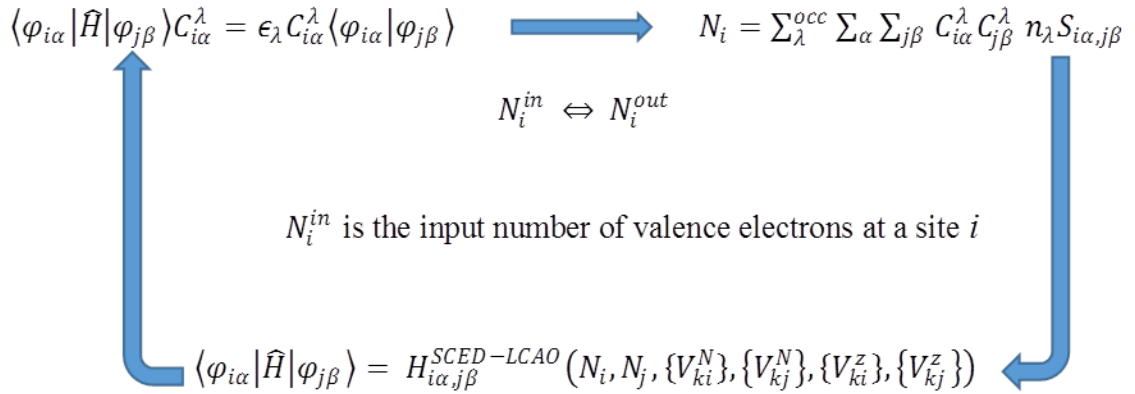
Figure 1. Schematic description of the Self-Consistency calculations in SCED-LCAO

The SCED-LCAO Hamiltonian is a parametrized function with 6 different parametric functions. The first is a scaling function which gives a reliable description of the two-center interaction term's dependence to the separation R_{ij} [4].

$$K(R_{ij}) = K_{ij}^0 e^{\alpha_{ij,k} R_{ij}} \tag{9}$$

The W term is used as an additional term on minimal basis sets when an aggregate of atoms exists and it tends to zero as the separation approaches infinity.

$$W_{i\alpha}(R_{ij}) = W_{i\alpha}^0 e^{-\alpha_{i\alpha,w}R_{ij}} \tag{10}$$

The third parametric function used in the SCED-LCAO Hamiltonian is the overlap matrix element

$$S_{ij,\tau}(R_{ij}) = \left(A_{ij,\tau} + B_{ij,\tau}R_{ij}\right)\frac{1+e^{-\alpha_{i\alpha,\tau}d_{ij,\tau}}}{1+e^{-\alpha_{i\alpha,\tau}(d_{ij,\tau}-R_{ij})}} \tag{11}$$

where the term τ in equation 11 indicating the different overlapping orbitals $ss\sigma, sp\sigma, pp\sigma$ and $pp\pi$.

For a heterogeneous system, the different parameters for different species are obtained from the corresponding fitting parameters associated with the atom at a site i and those associated with another atom at another site j. The parameters used for a heterogeneous system are then:

$$\alpha_{ij,K} = \delta_{ij}\alpha_{i,K} + (1 - \delta_{ij})\alpha_{j,K} \tag{12}$$

$$A_{ij,\tau} = \frac{\delta_{ij}|\varepsilon_{i,\mu}|A_{i,\tau} + (1-\delta_{ij})|\varepsilon_{j,\nu}|A_{j,\tau}}{\delta_{ij}|\varepsilon_{i,\mu}| + (1-\delta_{ij})|\varepsilon_{j,\nu}|} \; ; \quad \alpha_{ij,\tau} = \frac{\delta_{ij}|\varepsilon_{i,\mu}|\alpha_{i,\tau} + (1-\delta_{ij})|\varepsilon_{j,\nu}|\alpha_{j,\tau}}{\delta_{ij}|\varepsilon_{i,\mu}| + (1-\delta_{ij})|\varepsilon_{j,\nu}|}$$

$$B_{ij,\tau} = \frac{\delta_{ij}|\varepsilon_{i,\mu}|B_{i,\tau} + (1-\delta_{ij})|\varepsilon_{j,\nu}|B_{j,\tau}}{\delta_{ij}|\varepsilon_{i,\mu}| + (1-\delta_{ij})|\varepsilon_{j,\nu}|} \; ; \quad d_{ij,\tau} = \frac{\delta_{ij}|\varepsilon_{i,\mu}|d_{i,\tau} + (1-\delta_{ij})|\varepsilon_{j,\nu}|d_{j,\tau}}{\delta_{ij}|\varepsilon_{i,\mu}| + (1-\delta_{ij})|\varepsilon_{j,\nu}|}$$

$$\tag{13}$$

where for $\tau = ss\sigma$ $\varepsilon_{i,\mu} = \varepsilon_{i,s}$ and $\varepsilon_{j,\nu} = \varepsilon_{j,s}$

for $\tau = sp\sigma$; $\varepsilon_{i,\mu} = \varepsilon_{i,s}$ and $\varepsilon_{j,\nu} = \varepsilon_{j,p}$

for $\tau = ps\sigma$; $\varepsilon_{i,\mu} = \varepsilon_{i,p}$ and $\varepsilon_{j,\nu} = \varepsilon_{j,s}$

for $\tau = pp\sigma$; $\varepsilon_{i,\mu} = \varepsilon_{i,p}$ and $\varepsilon_{j,\nu} = \varepsilon_{j,p}$

and for $\tau = pp\pi$; $\varepsilon_{i,\mu} = \varepsilon_{i,p}$ and $\varepsilon_{j,\nu} = \varepsilon_{j,p}$

The term δ_{ij} represents a parameter that allows a weighted average of the parameters characterizing the overlap matrix elements in a heterogeneous environment with one type of atom located at site i and another type located at site j. It accounts for the chemical potential differences between two different atomic species [2] and has values in the range $0 < \delta_{ij} < 1$. $\delta_{ij} = \frac{1}{2}$ when the two sites i and j are occupied by the same type of atom.

The fourth, fifth and sixth parametric functions defined in the SCED-LCAO Hamiltonian are the potential function describing the electron-electron interaction V_N, the potential function describing the electron-ion interaction V_Z and the short range function ΔV_N. The two terms V_N and V_Z represent the weighted averages over the corresponding terms for elemental systems that occupy sites i and j respectively and their respective expressions are:

$$V_N(R_{ij}) = \delta_{ij}V_{i,N}(R_{ij}) + (1 - \delta_{ij})V_{j,N}(R_{ij})$$

$$V_Z(R_{ij}) = \delta_{ij}V_{i,Z}(R_{ij}) + (1 - \delta_{ij})V_{j,Z}(R_{ij})$$

(14)

where:

$$V_{i,N}(R_{ij}) = V_{i,Z}(R_{ij}) + \Delta V_{i,N}(R_{ij})$$

$$V_{i,Z}(R_{ij}) = \frac{E_0}{R_{ij}}\left[1 - (1 + B_{i,Z}R_{ij})e^{-\alpha_{i,Z}R_{ij}}\right]$$

(15)

$$\Delta V_{i,N}(R_{ij}) = (A_{i,N} + B_{i,N}R_{ij})\frac{1 + e^{-\alpha_{i,N}d_{i,N}}}{1 + e^{-\alpha_{i,N}(d_{i,N}-R_{ij})}}$$

and

$$V_{j,N}(R_{ij}) = V_{j,Z}(R_{ij}) + \Delta V_{j,N}(R_{ij})$$

$$V_{j,Z}(R_{ij}) = \frac{E_0}{R_{ij}}\left[1 - \left(1 + B_{j,Z}R_{ij}\right)e^{-\alpha_{j,Z}R_{ij}}\right] \tag{16}$$

$$\Delta V_{j,N}(R_{ij}) = \left(A_{j,N} + B_{j,N}R_{ij}\right)\frac{1 + e^{-\alpha_{j,N}d_{j,N}}}{1 + e^{-\alpha_{j,N}(d_{j,N} - R_{ij})}}$$

With the corresponding parameters being

$$A_{i,N};\ B_{i,N};\ B_{i,Z};\ d_{i,N}\ \text{and}\ \alpha_{i,Z}\ \text{where}\ \alpha_{i,Z} = \frac{U_i - A_{i,N}}{E_0} - B_{i,Z} \tag{16.1}$$

$$A_{j,N};\ B_{j,N};\ B_{j,Z};\ d_{j,N}\ \text{and}\ \alpha_{j,z}\ \text{where}\ \alpha_{j,z} = \frac{U_j - A_{j,N}}{E_0} - B_{j,Z} \tag{16.2}$$

with $E_0 = \frac{e^2}{4\pi\varepsilon_0}$ being the ground state energy.

The total energy of an atom of the system at a given site is:

$$E_{total} = \sum_{\lambda}^{occ} n_\lambda \varepsilon_\lambda + \frac{1}{2}\sum_i(Z_i^2 - N_i^2)U_i - \frac{1}{2}\sum_i\sum_{j\neq i} N_i\,N_j V_N(R_{ij}) +$$

$$\frac{1}{2}\sum_i\sum_{j\neq i} Z_i\,Z_j\frac{E_0}{R_{ij}} \tag{17}$$

and the lth component (where $l = x, y$ or z) of the force acting on the atom at a given site k is:

$$F_k^l = -\sum_{\lambda}^{occ}\sum_{i\alpha}\sum_{j\beta} n_\lambda\left(C_{i\alpha}^\lambda\right)^* C_{j\beta}^\lambda\left[\frac{\partial H_{i\alpha,j\beta}^{SCED-LCAO}}{\partial x_k^l} - \varepsilon_\lambda\frac{\partial S_{i\alpha,j\beta}}{\partial x_k^l}\right] + \frac{1}{2}\sum_i\sum_{j\neq i}\frac{\partial\left(N_iN_jV_N(R_{ij})\right)}{\partial x_k^l} -$$

$$\frac{1}{2}\sum_i\sum_{j\neq i} Z_i\,Z_j\frac{\partial\left(\frac{E_0}{R_{ij}}\right)}{\partial x_k^l} \tag{18}$$

The parameters given in the above stated equations are important in determining the SCED-LCAO Hamiltonian. To ensure of their reliability, an optimization or fitting scheme based on global least-squares defined in Ref. [2] of these parameters is required. In the framework of fitting the SCED-LCAO parameters, their transferability is first investigated by setting up a database for physical properties such as bond lengths or geometries and binding energies of stable structures like small clusters, sheets, bulk phases

obtained from reliable first-principle calculations, experimental results and metastable configurations obtained by first principles calculations [2]; then these set of parameters will be optimized for the SCED-LCAO Hamiltonian and finally compare the results with ab-initio calculations and or experimental results. If transferability is confirmed the next step on fitting is the robust test which is done by calculating the physical properties for more complicate or complex structures using optimized set of parameters obtained and the results are compared with ab-initio and or experimental results. A summary of the framework for fitting SCED-LCAO scheme is given in figure 2 below.

$$H_{i\alpha,j\beta}^{SCED-LCAO}\left(N_i, N_j, \{V_{ki}^N\}, \{V_{kj}^N\}, \{V_{ki}^z\}, \{V_{kj}^z\}\right)$$

Transferability of Parameters:
1. Set up database for small clusters, sheets, bulk phases...
2. Optimize set of parameters
3. Compare results with ab-initio and or experimental

Robust Test:
1. Calculate physical properties for more complicated or complex structures
2. Compare with ab-initio and or experimental results
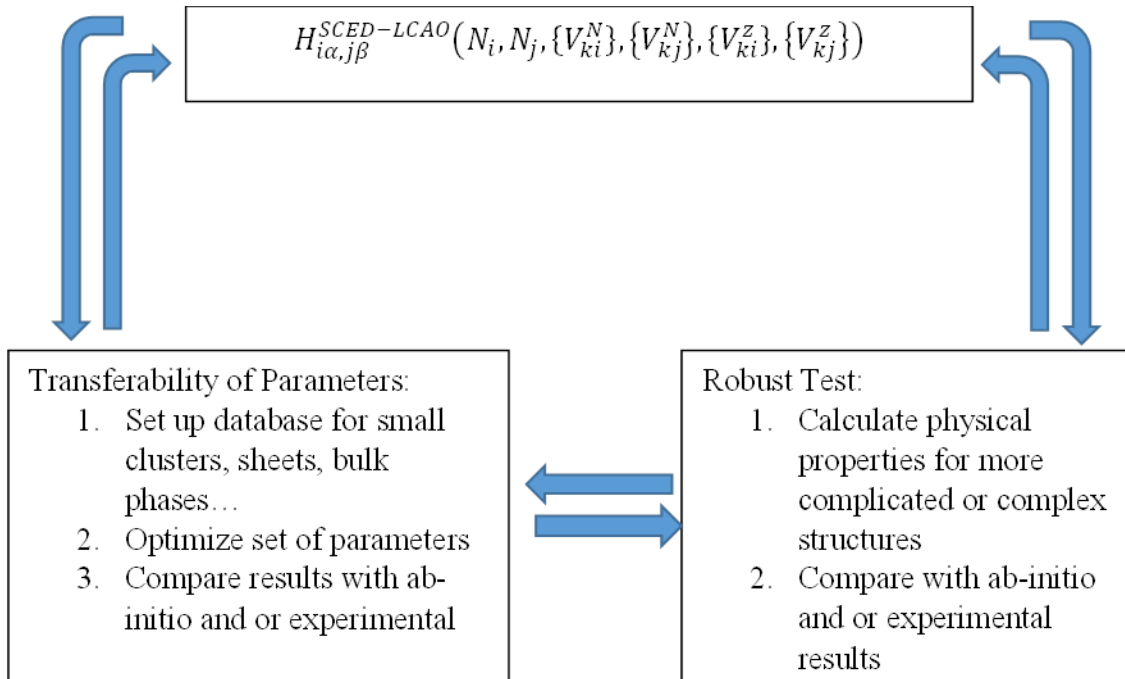
Figure 2. Scheme for fitting SCED-LCAO parameters.

The accuracy of SCED-LCAO Hamiltonian was compared to DFT and previously reported semi-empirical methods that included within their expressions only two-center interactions such as in the old model of ref. [15] and also in the models reported by ref. [16-18] or when the method included two-center interactions with no self-consistency but

having also an environment dependency term as in models [19-22]. It was shown that the SCED-LCAO Hamiltonian was more in agreement with DFT using local density approximation (LDA) for total energy calculations for Si bulk phases than the non-orthogonal tight binding semi-empirical based methods mentioned earlier. We can note that in the new model of DFTB [15], the environment dependency treatment depends on whether there is charge redistribution or not. If there is charge redistribution, then the environment dependency is included, if there is no charge redistribution the environment dependency part disappears. Hence there is no need to improve the Si bulk phase diagram since the environment dependency term of their new model will have no effects on the results.
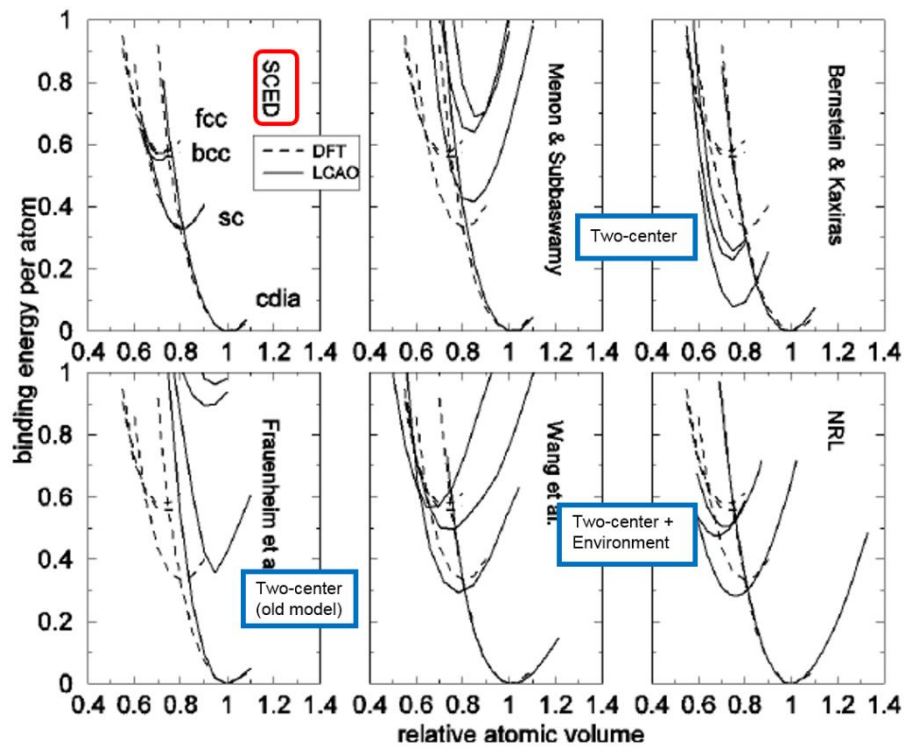
Figure 3. Si bulk phase diagram [2] comparison between SCED-LCAO and DFT with other semi-empirical methods having only two-center interactions or two-center interactions and environment-dependency involved.

The SCED-LCAO was shown to be an accurate and transferable Hamiltonian. To ensure that SCED-LCAO Hamiltonian is a necessary within the field of theoretical physics, the computational wall time and memory usage required for simulation with SCED-LCAO should be more efficient than the other semi-empirical methods and or first-principles methods. In reference [3] it was proven that SCED-LCAO required five times less memory and was also thirty times faster than VASP in calculations of small clusters of Si. When very large systems of structures are involved, the order-N algorithm (O(N)) is also proven to be a good tool. The particularity of SCED-LCAO molecular dynamic is that it can be used to calculate structures of complex molecules, quasi-one-dimensional structures, crystalline structures and crystalline structures with defects through parallel computing as mentioned in [3] where results of calculations on silicon nanowires with diameters d ranging $3 \leq d \leq 15 nm$ were shown and it was also shown that the execution time and the memory required were scaling linearly as the size of the nanowires were increasing. At the same time, it was also shown that the computational speed-up was system-size dependent.

The fitted parameters for carbon, silicon, boron and gallium have been tested extensively and have been reported in literature (for carbon, silicon and boron). In table 1 we will summarize the different Hamiltonian parameters fitted for each of the elements mentioned above.

Hamiltonian Parameters	CARBON	SILICON	BORON	GALLIUM
$\varepsilon_s(eV)$	-17.360	-13.550	-13.460	-11.55396
$\varepsilon_p(eV)$	-8.329	-6.520	-8.430	-5.673576
$\varepsilon_s'(eV)$	-37.274639	-13.779244590	-16.410946500	-15.89942562
$\varepsilon_p'(eV)$	-21.689008816	-7.778834550	-14.529140600	-9.78502345
$w_s^0(\text{Å}^{-1})$	0.839858480	1.277531550	-0.920581500	-0.00445490
$w_p^0(\text{Å}^{-1})$	-0.614966730	-1.093182750	0.182560680	-0.10498407
$\alpha_{s,w}(\text{Å}^{-1})$	1.666784180	1.813967100	2.171829850	1.32305085
$\alpha_{p,w}(\text{Å}^{-1})$	1.780814610	1.337365470	1.225140150	1.39086822
$U(eV)$	13.940753510	7.997116560	18.586169640	13.66059628
$\alpha_K(\text{Å}^{-1})$	-0.071034140	0.274291720	0,172647010	0.09070368
$A_N(eV)$	-2.629122940	-0.759899550	-2.075105160	-1.40923471
$B_N(\text{Å}^{-1})$	-1.577483080	0.214034770	-1.143059360	-1.74623609
$\alpha_N(\text{Å}^{-1})$	3.523180590	2.420667900	2.502264520	2.38478380
$d_N(\text{Å})$	0.696949050	2.209409220	-0.597076730	-0.04540130
$B_Z(\text{Å}^{-1})$	2.259314750	1.962774350	2.916817290	1.57855854

Table 1.1. Hamiltonian fitted parameters for carbon [23], silicon [23], boron [24] and gallium [25]

Overlap Parameters	CARBON	SILICON	BORON	GALLIUM
$B_{ss\sigma}(\text{Å}^{-1})$	1.010909470	0.000678000	0.317921800	-0.17126234
$\alpha_{ss\sigma}(\text{Å}^{-1})$	2.655122460	2.074621740	1.476503650	1.71417826
$d_{ss\sigma}(\text{Å})$	0.498627150	1.405027960	0.520118300	1.66785074
$B_{sp\sigma}(\text{Å}^{-1})$	-0.523238020	-1.076298970	0.465862790	0.49124563
$\alpha_{sp\sigma}(\text{Å}^{-1})$	2.422573570	2.043994870	1.819749840	2.04314742
$d_{sp\sigma}(\text{Å})$	1.254380770	1.002657780	1.118493150	1.68594570
$B_{pp\sigma}(\text{Å}^{-1})$	-1.214184510	-0.841175340	-0.906133270	-0.61936298
$\alpha_{pp\sigma}(\text{Å}^{-1})$	2.171554140	2.193129270	3.634107780	2.57254048
$d_{pp\sigma}(\text{Å})$	1.211609000	1.895552620	1.528827550	2.36229832
$B_{pp\pi}(\text{Å}^{-1})$	-0.109556040	-0.163947800	-0.305454380	-0.11258717
$\alpha_{pp\pi}(\text{Å}^{-1})$	2.038494880	2.108168830	1.425364160	1.69590206
$d_{pp\pi}(\text{Å})$	0.804059930	1.617996160	0.326449510	1.29280440

Table 1.2. Overlap fitted parameters for carbon [23], silicon [23], boron [24] and gallium [25]

It has then been proven both in refs. [2-4] that SCED-LCAO as a semi-empirical method has transferable Hamiltonian parameters and is at the same time reliable. It was also shown that it can be used in more complex environments due to its environment-dependency term taking care of the electron screen effects in an aggregate of atoms. SCED-LCAO also has a very large scale that is it can handle systems of tens of thousands of atoms (~20000 atoms system) and also has a much more relative simulation time compared to DFT based ab-initio methods and finally SCED-LCAO has a good predictive power

CHAPTER III

LOW DIMENSIONAL α-B$_{12}$ STRUCTURES – AN APPLICATION OF SCED-LCAO

HAMILTONIAN FOR BORON ELEMENT

3.0 Background.

Boron as an element occupies the fifth (5th) position in the periodic table of elements. It is a non-metal with low chemical reactivity at room temperature, a very high melting point of $2450K$, and low volatility of ordinary temperatures [26]. Boron also displays some of the most remarkable physical and chemical properties of any element in the periodic table. Its position in the periodic table suggests that boron is an electron-deficient element and has the tendency of forming three-center two-electron bonding type or covalent bonding type; it is also used as a dopant in the semiconducting industry. Boron has been of great interest to researchers and the development of newly discovered materials and allotropes of boron have been reported in the literature including (1) linear, planar, quasi-planar, convex, ring and icosahedral clusters for small sizes of B$_n$ ($n \leq 14$) clusters [27, 28]; (2) planar, quasi-planar, and double rings for sizes of B$_n$ clusters with $n \leq 42$ [29-36]; (3) fullerene, cage, and core-shell structures for intermediate sizes of B$_n$ clusters ($n \leq 180$) [37-45]; and (4) compact structures for larger sized of B$_n$ clusters ($n > 180$) [4], respectively.

In particular, we have to note that the B$_{80}$ fullerene has been part of the most famous cage structures of boron with the debate being centered on its most stable isomer. Initially

B_{80} with I_h symmetry was predicted as the most stable boron cage [38] and energetically more stable than boron double rings which were already considered as building blocks of boron nanotubes. The I_h B_{80} was also compared to B_{72} and B_{92}, and these were found to be less stable. Subsequently, the report from ref. [42] claimed that if geometry optimization was performed without any symmetry constrains, a new symmetry namely T_h symmetry will be found to have a more stable in energy, and more importantly this new symmetry has two isomers depending on the capping atoms at the center of the 20 hexagons. The contributions of these capping atoms were studied in ref. [40] through their bonding nature. Using density functional formalism, ref. [39] studied the vibrational stability of B_{80} fullerenes and found that B_{80} with I_h was vibrationally unstable with two sets of imaginary modes, while the B_{80} with T_h symmetry was vibrationally stable. Through the use of dispersion-corrected density functional calculations on B_{80} with I_h symmetry, ref. [44] compared it to the two B_{80} isomers namely T_h-A and T_h-B and it was confirmed that the B_{80} I_h has imaginary vibrational modes, but by inclusion of density functional dispersion correction, all vibrational modes were positive and the energy order was reversed with I_h symmetry becoming more stable than T_h-A. Hence according to ref. [44] I_h is reinstalled as the lowest energy conformation among the buckyball structures with the van der Waals dispersion forces greatly impacting on the geometry of the capping atoms. Ref. [41], as an erratum to ref. [38], gave a number of local minima isomers of B_{80} namely I_h, T_h, and, C_1 was reported as a new lower minimum. The stability of B_{80} was also considered in ref. [4] as a robust test for the boron SCED-LCAO Hamiltonian. SCED-LCAO MD simulation was performed on the B_{80} with initial I_h symmetry. It was found that the system was transformed to a T_h symmetry before stabilizing to C_{2h} symmetry.

The newly discovered materials and allotropes of boron for large size of B_n clusters with $80 \leq n < 770$ have been reported by the CMT group at the University of Louisville [4] as compact boron structures. The stability and energetics of nearly 230 compact boron clusters ranging from 100 to 768 atom systems have been investigated using SCED-LCAO molecular dynamics. These compact boron clusters were divided into random structures of B_n with over 90 stable boron clusters considered; and rhombohedral structures of B_n with a total of 80 rhombohedral clusters including chain-like, sheet-like and bulk-like were also considered. Another type of compact structures considered was the spherical icosahedral structure of B_n obtained through spherical cut from α-B. A SCED-LCAO molecular dynamics was performed on such structures and it was found that the spherical cuts were still more stable than the cage and chain like cuts when the boron atoms are larger than 200, concluding that the more bulk-like the compact structures are the more stable for large B_n clusters.

Boron nanowires have already been successfully synthesized according to [46-48], and simultaneously, on the theoretical side, tubular and monolayer sheet structures have been predicted [6, 7, 49-54]. With the synthesis of a two-dimensional carbon structure, graphene [5], the search for the possible existence of two-dimensional structures based on boron have been intense. Recently a two-dimensional sheet of type α has been predicted, using ab-initio calculations by refs. [7, 52], to be the most stable monolayer boron sheet among all monolayer sheets, followed by β-types of boron sheets [55]. Quite recently ref. [6] used PBE0 hybrid functional within first-principles to do a global search for new lowest energy polymorphs of two-dimensional boron sheets. Different types of boron monolayer sheets have been considered with the classification of the types depending on the

coordination number of boron atoms, i.e., α-, β-, χ-, ψ-, and δ-types, respectively. The α-type (same as in ref. [7]) was found to have the greatest cohesive energy but exhibited negative phonon frequencies which were removed after a new relaxation of the structure. The newly relaxed structure was found to be slightly buckled and named α'. It was reported to have greater cohesive energy compared to α and both sheets exhibited semiconducting properties using the hybrid PBE0, in contrast to the metallic properties found in the calculations using the hybrid PBE [6, 7]. In the β-type, β_1, β_2, and β_3 are reported to be metallic with β_1 being planar and having the second greatest cohesive energy after α' while β_2, and β_3 are slightly buckled. δ_5 was found to be planar and also having the greatest cohesive energy among the δ-type of boron monolayer sheets but buckled δ_6 was more stable among δ sheets. Therefore, the predicted monolayer sheets were found to have great cohesive energies with semiconducting properties such as the buckled α' sheet in the α-type, the planar and metallic β_1 sheet in the β-type, and the buckled δ_6 sheet in the δ-type. These predicted 2D boron monolayer sheets have not yet been synthesized successfully, and raise an interesting issue to search for new types of 2D boron structures in the boron family.

As mentioned earlier, in crystalline boron the icosahedral boron 12 units or α-B_{12} are the building blocks of boron crystalline structures [8] and they have bonding type of three-center two-electrons (i.e., each pair of electrons is explicitly shared by three bonded B atoms). Even though the isolated icosahedral α-B_{12} was found to be less favorable or stable energetically compared to the quasi-planar B_{12} or ring structures B_{12} clusters [4] as shown in table 2, it was more favorable when icosahedral α-B_{12} units are aggregated with the bond lengths of about 1.71Å [26], which are stronger than their intra-icosahedral bonds

(which are the bonds between Boron atoms within the same icosahedron unit (1.73 to 1.79Å [26])), and hence it is more suitable in forming stable or metastable polymorphs.

Our main aim in this chapter was to use the well fitted Hamiltonian parameters for boron element [4] to investigate the possibility of having low dimensional boron structures built by icosahedral α-B_{12} units and systematically study their structural and electronic properties. These low dimensional structures will have their initial structures derived from the rhombohedral α-B in which as mentioned earlier, a given icosahedron has the possibility to form strong covalent bonds with other six neighboring icosahedra. The structural properties of rhombohedral α-B are its lattice parameter $a_0 = 2.83$ Å and the apex angle α. Using a linear truncation of rhombohedral α-B along (001) direction, one-dimensional icosahedral structures referred to as one-dimensional icosahedral chains were created. To obtain a two-dimensional icosahedral sheet, a cut at one of the faces of the rhombohedral α-B will be needed. A more detailed discussion on how to obtain the two-dimensional sheets will be given in sub-section 3.1 of this chapter.
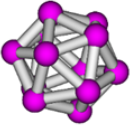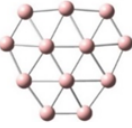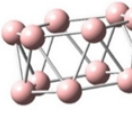
B_{12} Structures	Cohesive Energy (eV)
α-B_{12}	-3.873
Planar B_{12}	-3.929
Ring B_{12}	-3.999

Table 2. Energy stability comparison between icosahedral α-B_{12}, planar B_{12} and ring structured B_{12}. With α-B_{12} > planar B_{12} > ring B_{12}. [where > stands for "less stable energetically than"]

3.1 Finite icosahedral α-B_{12} chains.

The structural and electronic properties for finite chains of icosahedral α-B_{12} were investigated by use of the boron SCED-LCAO Hamiltonian parameters given in Table 1 in CHAPTER II. This was done by first creating the chain structures through a linear truncation of rhombohedral α-B along the (001) direction (referred as 1x1xn). The shortest possible finite chain considered was a dimer with a total of 24 atoms and a two-center two-electron bond joining the two α-B_{12} making the chain. The lengths of the chains were then increased along the (001) direction by n units of α-B_{12}. Hence the considered finite chains have lengths defined by the number n of α-B_{12} in it where n ranges between 2 and 26. Structure relaxations were performed through 3000 MD steps with 1.20 fs per MD steps at 0K. The relaxation was done until the forces were less than 10^{-2} eV/atom and as it was performed, we found that there was freedom of movement for the balls along the chain direction and that freedom of movement lead to extension of the chains in the covalent bonds. We note that the bonds became longer for the short chains. For longer chains the bonds at the center or near the center of the chain were much stronger than the covalent bonds at the extremes. The dimer and 1x1x9 can be taken as examples. In the dimer, the single two-center two-electron bond after relaxation extends to 1.745 Å which is even longer than the 1.71 Å in α-B reported in ref. [26]. While for the chain with 9 balls, the two covalent bonds at the center of the chain are about 1.733 Å but at the ends of the chain, the bonds become weaker with the bond length of about 1.740 Å which are slightly elongated compared to the central ones. To be more convinced about this we also examined a longer chain with 14 balls. We found that after relaxation the balls at the extremes of the chain have their bonds extended to 1.731 Å, as compare to the most central bond with a length

of 1.702 Å. Hence we can say that structurally, for a given chain, the two-center two-electron type of bonding is strong as one gets closer to the center of the chain. In a more general way as the length of the chains increases, the strengths of the covalent bonds between the icosahedral units also increase. Figure 4 gives a summary of the different bonding discussed above after 2 MD steps and after full relaxation.
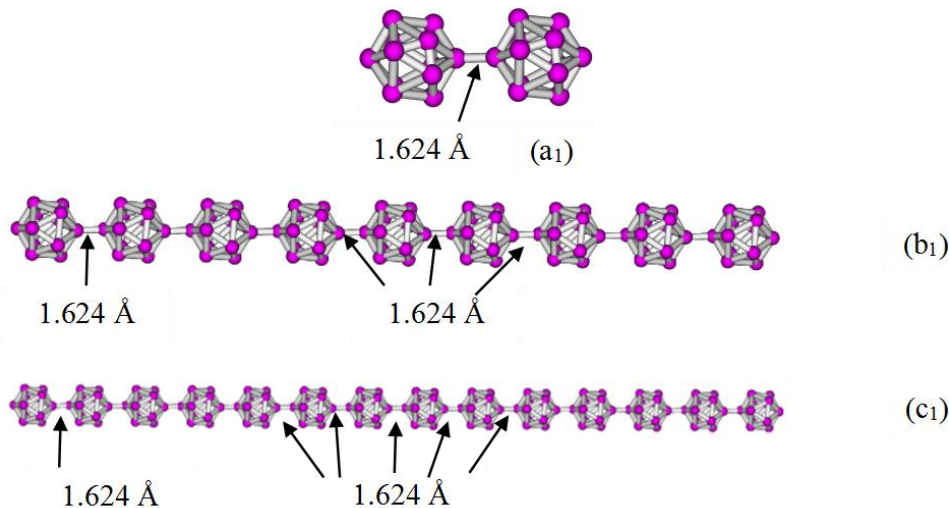
Figure 4.1. Two-center two-electron bonding for finite α-B_{12} chains ((a) dimer, (b), 1x1x9 finite chain and (c) 1x1x14 finite chain). The numbers denote the bond lengths after 2 MD steps.
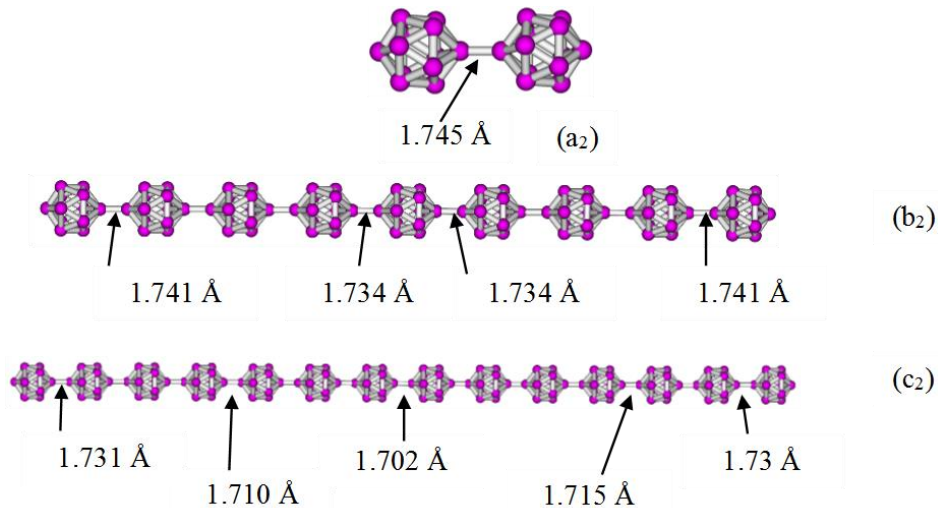
Figure 4.2. Two-center two-electron bonding for finite α-B_{12} chains ((a) dimer, (b), 1x1x9 finite chain and (c) 1x1x14 finite chain). The numbers denote the bond lengths after full relaxation.

The structural stability of the icosahedral finite chains was also determined by finding the relative energy for a given chain length with respect to the energy of a single α-B_{12} and as can be seen from figure 5, the relative chain energies converges as the length of the chains increase.
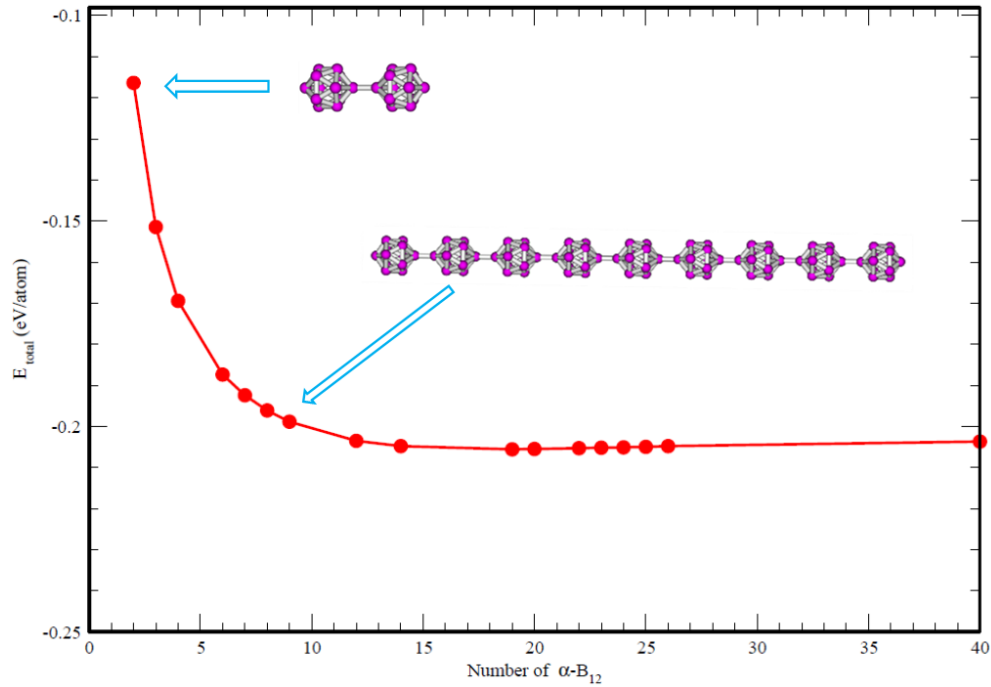
Figure 5. Energies of finite α-B_{12} chains relative to a single α-B_{12} ball.

An illustration of the structures of chains with lengths 2 and 9 are shown in the inset with the arrows pointing to their respective energies. The distribution of the charges with a given finite chain was also investigated by performing local analysis of the structures. The ball will be divided into two halves and the average charge of each half was determined. We found that the unboned halves of the units (i.e., the two distinct ends of a given chain) tend to lose charges compared to the inner parts or the other halves of the unit, and as the length/number of α-B_{12} balls increases, the average charges at the center of the chain tend to be uniform to $3.0e$. For an illustration, figure 6 shows the average charge distribution of some finite chains.
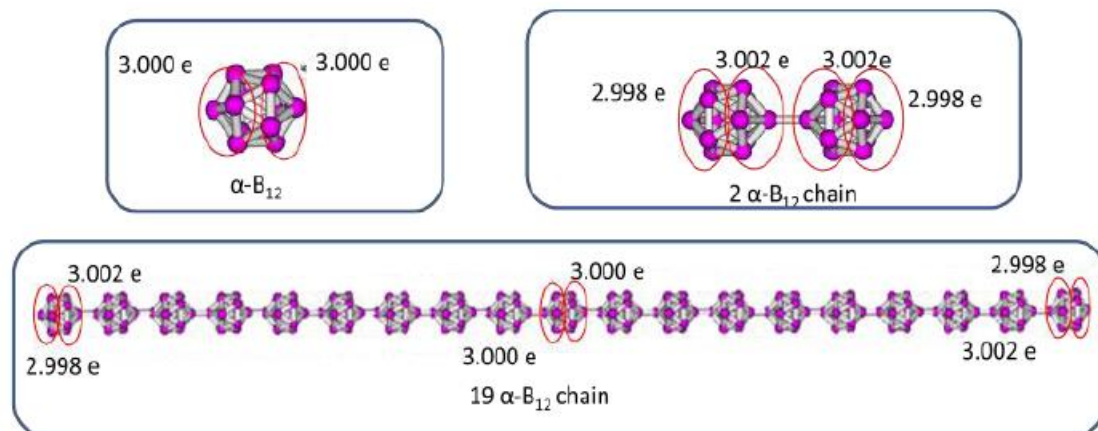
Figure 6. Charge distribution for an average of 6 atoms indicated by the red circles. The structures are single α-B_{12}, α-B_{12} dimer, and the finite chain with 19 α-B_{12} balls, respectively.

The electronic properties of the finite chains were studied from their respective electronic densities of states. It was observed that the finite chains were all displaying metallic behaviors as can be seen from figure 7. We also noticed that moving from the single α-B_{12} ball to the dimer and subsequently increasing the length of the chains, there is the appearance of some states just around the top of the valence bands which are associated with the presence of the two-center two-electron bonds (see the states marked by red circles in Fig. 7). By having a closer look at the states around the top of the valence band and the bottom of the conduction band (see Fig. 8), it was observed that the existence of states around the Fermi level (see the states marked by red circles in Fig. 8) is attributed to the bonding states at the end of the chain and such states tend to disappear as the length of the chains increases.
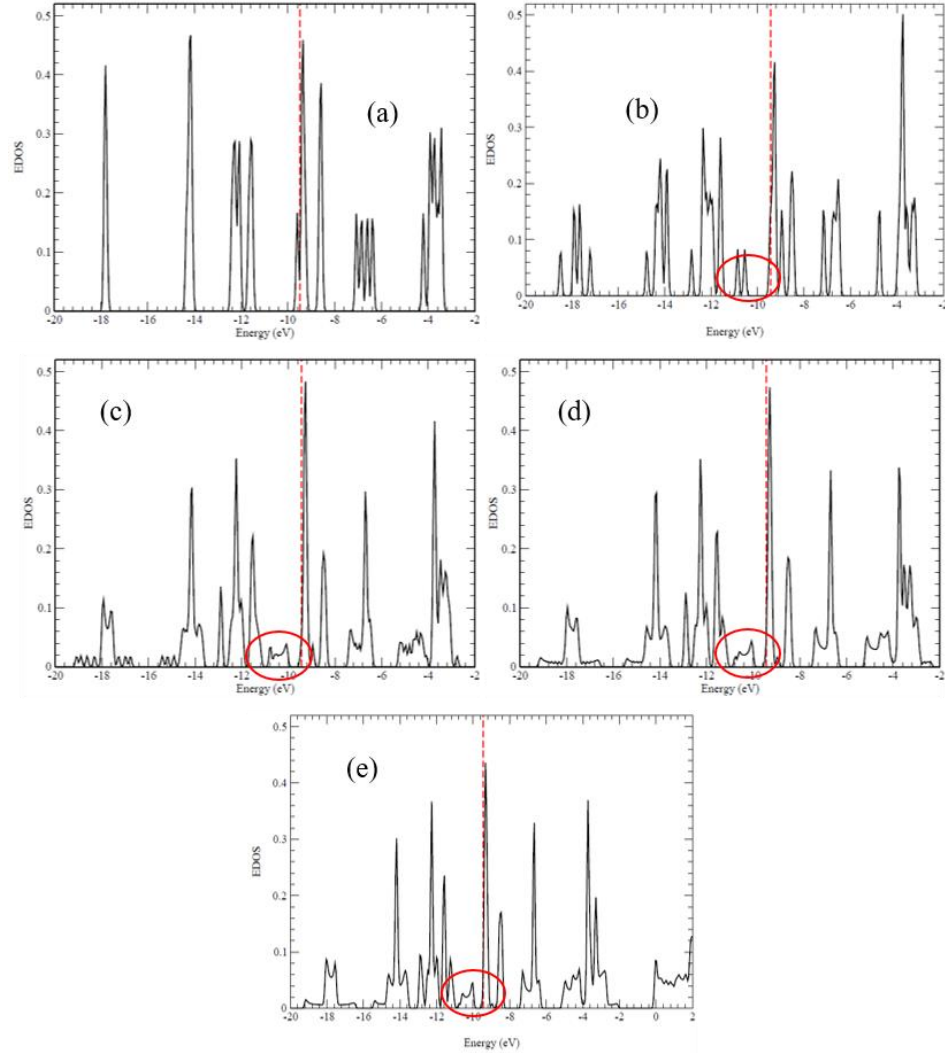
Figure 7. The electronic density of states (EDOS) of a single α-B$_{12}$ (a) ball and a selected number of finite chains. The red circles show the states associated with the presence of the inter-icosahedral bonds between 2 balls in a given chain; note that (b) is the EDOS for the dimer; (c) is for the chain with 9 balls, (d) is for the one with 19 balls and (e) is the chain with 40 balls.

The finite chains are found to be all metallic. By comparing the EDOS of the single ball (Fig. 8 (a)) we noticed that those states start to decrease as the chains are formed and increased, and the Fermi level shifts towards the left that is near the bottom of the conduction band as shown in figure 8 (b)-(e) highlighted by the red dashed line.
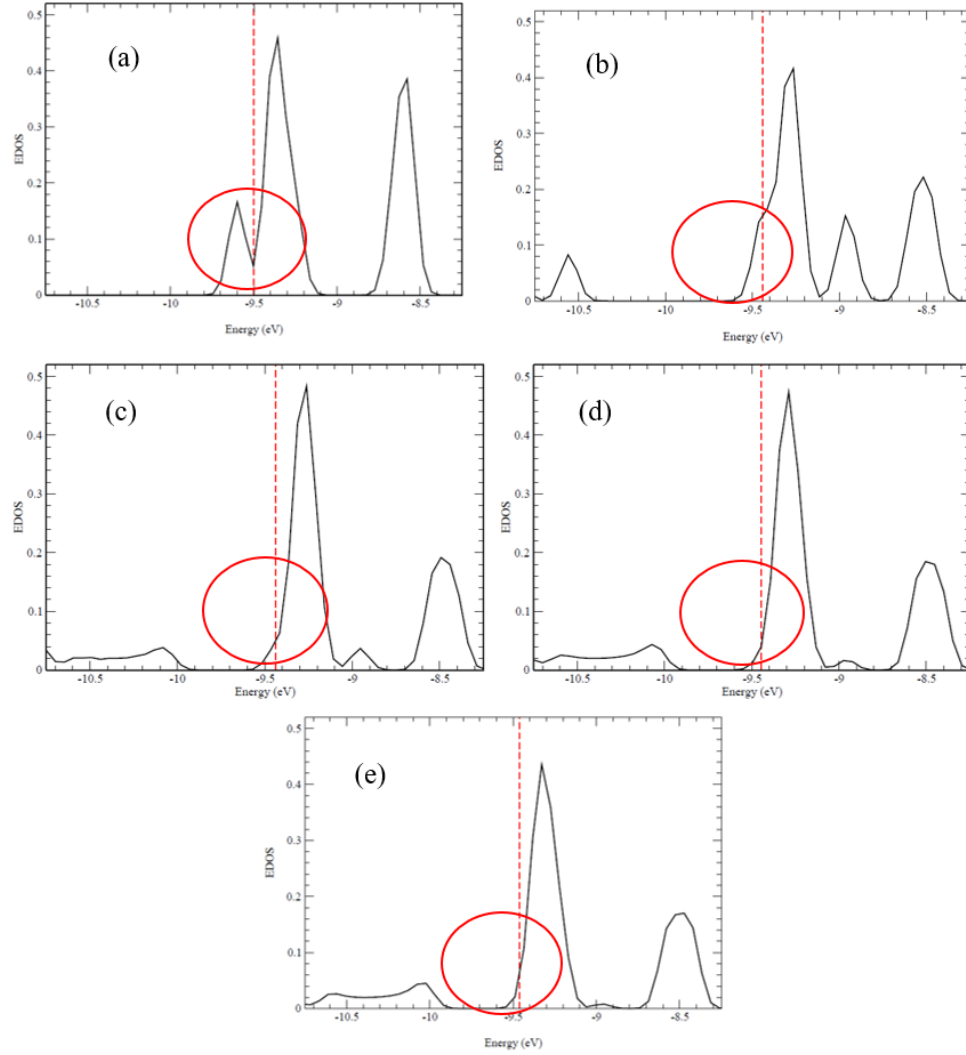
Figure 8. Zoomed in EDOS for (a) a single α-B$_{12}$ ball, (b) a dimer of α-B$_{12}$, (c) a finite chain with 9 balls, (d) a finite chain with 19 balls and (e) a finite chain with 40 balls, respectively. The red circle is highlighting the states associated with the bonding at the end of the chains.

Hence for the finite chains we discovered that the inter icosahedral bonds become shorter therefore stronger as the lengths of the chains increase, the charge distribution was also related to the length of the finite chain since the average charges at the center of the chains were found to be more uniform as the chain length increases. In terms of electronic properties, the finite chains were metallic due to the appearance of states accounting for the inter icosahedral bonds. Another observation was the smoothening of the states at the bottom of the conduction band with the Fermi energy shifting towards that end. These

33

results have been presented in the APS March Meeting in 2013 [56]. All these observations made us question of what will happen if we have chain as long as possible. Would its structural and electronic properties be similar to that of the shorter finite chains or would it be totally different?

3.2 Infinite icosahedral α-B$_{12}$ chain.

The infinite icosahedral chain is built through a linear truncation of rhombohedral α-B along the (001) direction. The structural and electronic properties of the infinite chain will be investigated by lattice constant optimization, local analysis to determine the bonding nature, the charge redistribution, and the electronic density of states. The optimization of the infinite icosahedral chain was done by scaling the lattice parameter a of its individual structures to the optimized lattice constant a_0 of α-B. The subsequent structures are then relaxed and their final energies compared to obtain the one with the lowest energy as the optimized chain structure. Figure 9 shows the total energy per atom vs the ratio of the lattice parameter a over that of the lattice constant a_0. The optimized lattice constant is $a^* = 1.057 * a_0$ with $a_0 = 2.834$ Å.
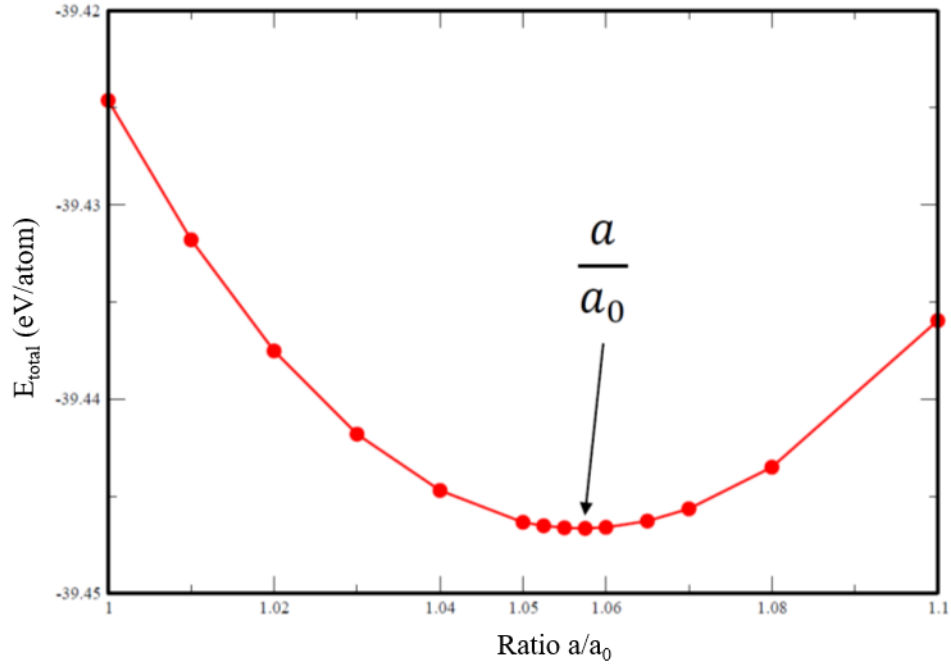
Figure 9. Lattice constant optimization for infinite α-B_{12} chains with $a_0 = 2.834$ Å and the optimized lattice constant obtained for the infinite chain being $a^* = 1.057 a_0$

The structural stability and the existence of the infinite chain was also investigated by calculations of its phonon frequencies using density functional theory based VASP [9] and we found that the lowest vibrational frequencies occur at 43.599 cm^{-1} which indicates that the infinite chain is stable and can also exists if synthesized under proper conditions. Other structural properties to be considered are the bonding nature, the pair and angle distribution functions. As mentioned earlier, the chains have two types of bonds, inter-icosahedral and intra-icosahedral bonds. For the infinite chains, the intra-icosahedral bonds were found in the range between 1.62 and 1.75 Å which is close to that of the isolated α-B_{12} (i.e., between 1.61 and 1.75 Å) but shorter than the intra-icosahedral bonds in the bulk α-B (i.e., between 1.73 and 1.80 Å), which can be explained as the existence of dangling bonds in the icosahedra B_{12}. As for the inter-icosahedral bonds, the bond lengths (1.762 Å)

are uniform along the chain and longer than that in the finite chains and in the bulk α-B as indicated in figure 10.
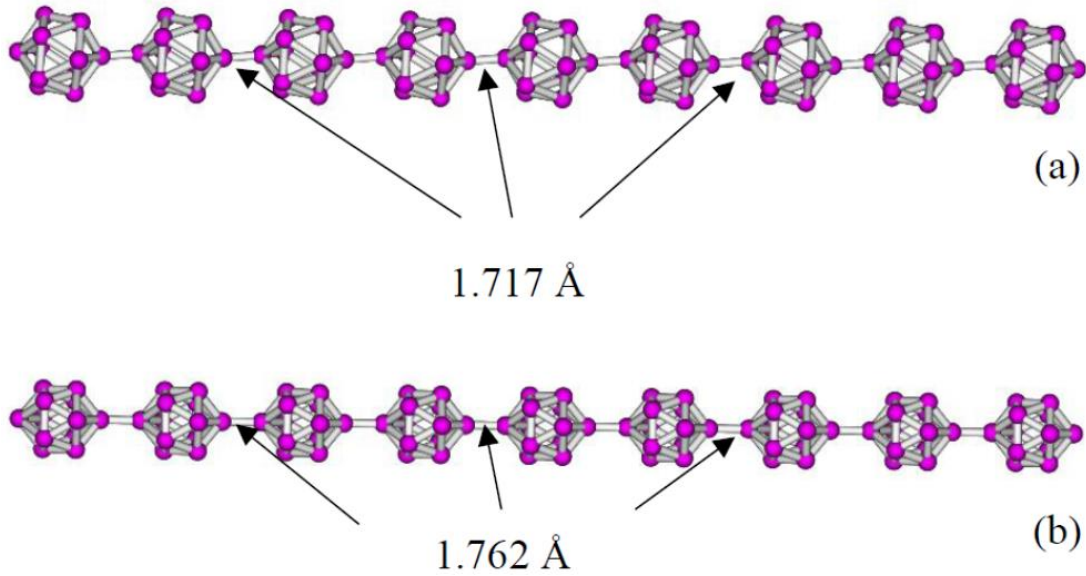
Figure 10. Inter-icosahedral bonds lengths for infinite α-B_{12} chains. (a) after 2MD steps and (b) after fully relaxation.

Pair and angle distribution functions were also compared to those of the isolated B_{12} to fully account for the different bonds and angles within the infinite chain. As can be seen from the pair distribution function plot (figure 11.1), the periodicity of the icosahedral infinite α-B_{12} chain is characterized by the pronounced peaks at greater distances with the presence of second and third nearest neighbors being more apparent in the infinite chain than in the isolated icosahedron. The small shoulder that appeared at the first peak in the infinite chain reveals the inter-icosahedral bonds.
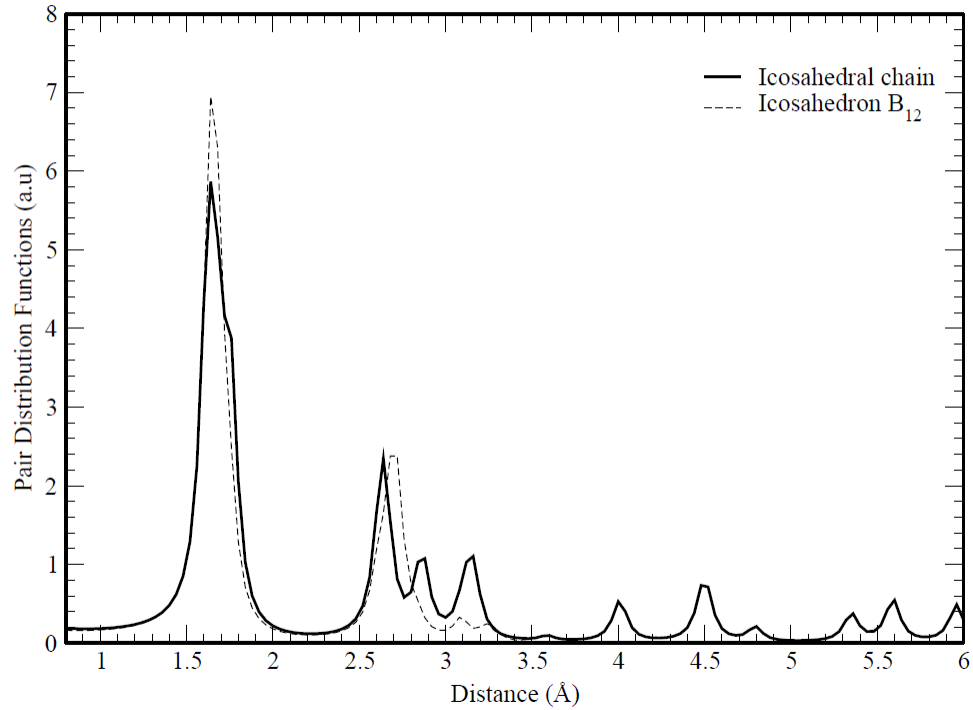
Figure 11.1. Pair distribution function for infinite chain and isolated icosahedron B_{12}

For the angle distribution in figure 11.2, we can see that the isolated icosahedral B_{12} has a single dominant peak at around 60° associated to the triangular structures inside the B_{12} ball. But that dominant peak is split into several sub-peaks in the infinite chain which is due to the deformation of the triangles and subsequent symmetry reduction for the balls along the infinite chain axis. Such deformation is also characterized by their elongation as identified by the peaks around the angles 96° and 128° as shown in figure 11.2.
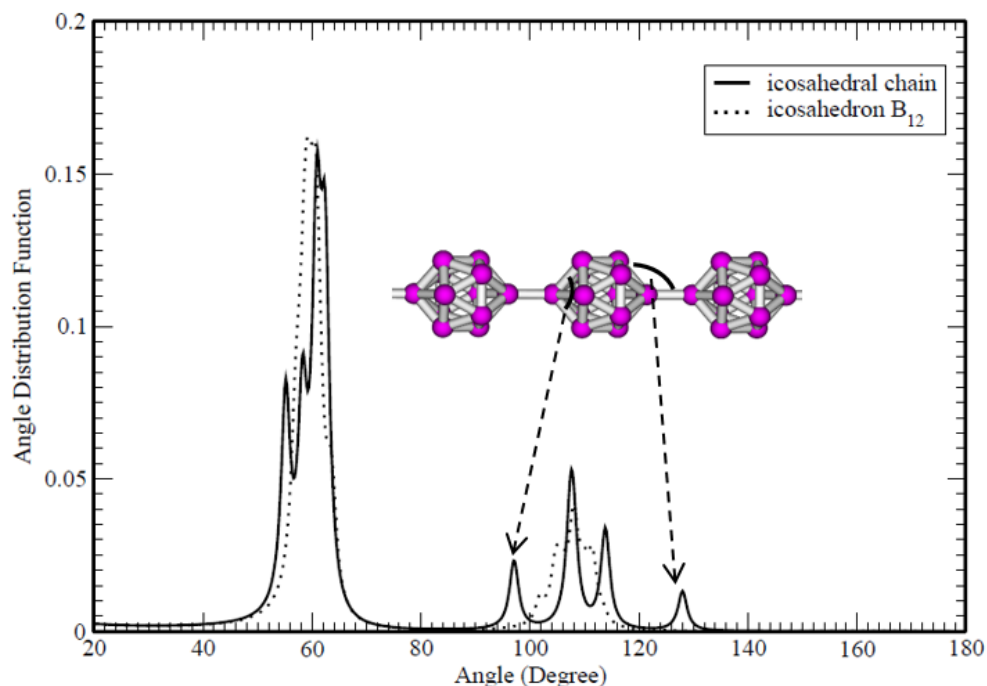
Figure 11.2. Angle distribution functions for infinite chain and icosahedron B_{12}. The two arrows are showing the 96° and 128° bonding angles within the chain.

The electronic properties of the infinite chain will be evaluated by first looking at the charge transfer along the chain axis as was done with the finite chains. Since for the infinite chain there is no unboned half due to the periodicity a uniform charge distribution throughout the length of the infinite chain is confirmed as shown in figure 12 below.
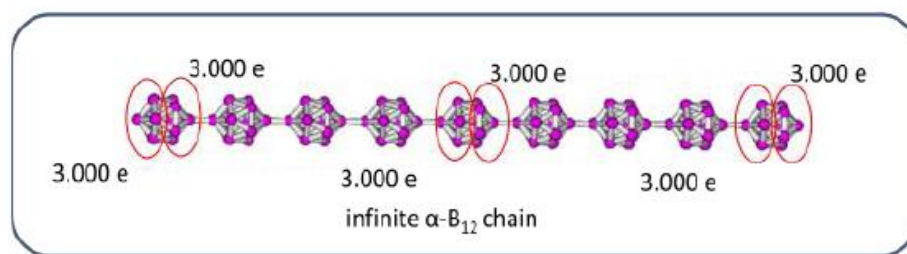
Figure 12. Average charge distribution throughout the length of the infinite chain. The red circles depict the atoms being averaged.

The electronic structure of the infinite chain was obtained through the calculations of the electronic density of states (see Fig. 13). We confirmed that the states associated to the inter-bond between balls in the finite chain (e.g., the red circle in figure 7) still exist in

the infinite chain (e.g., the red circle in figure 13 (a)), and the states associated with the bonding at the end of the finite chains (see figure 8) disappear in the infinite chain (see figure13 (b)). In particular, with a continuation of the shifting of the Fermi energy from the bottom of the conduction band towards the top of the valence band, as the chain from finite length to the infinite, a subsequent gap of 0.74 eV is opened, clearly indicating that the infinite chain exhibits semiconducting behaviors even though it is small compared to the bulk α-B (1.90eV [57] close to the optical gap of 2.0 eV). The results for the infinite icosahedral chain have been published in nanotechnology in 2015 [58].
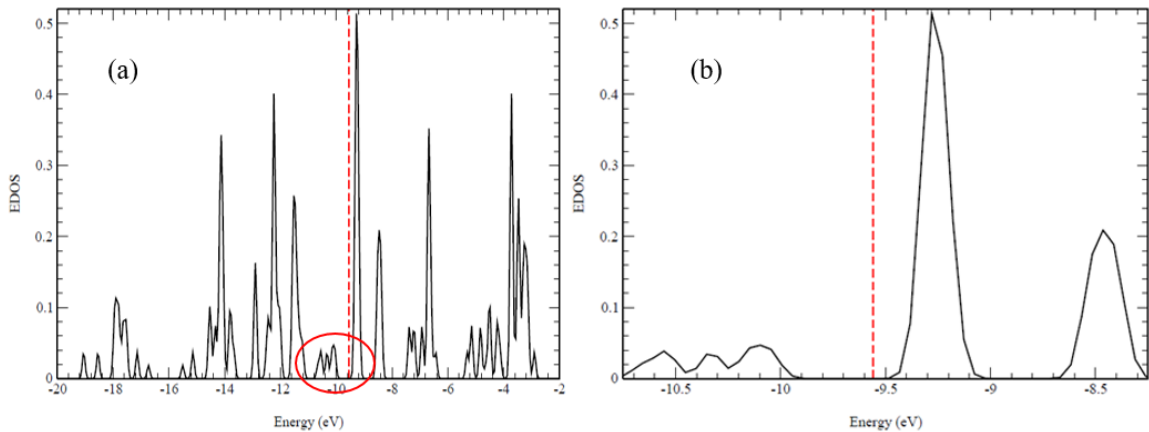
Figure 13. EDOS for infinite chain. (a) red circle shows the existence of covalent bonds along the axis of the chain and (b) Energy gap opens and states associated with the chain ends with the finite length disappear.

3.3 Icosahedral α-B_{12} ring structures.

With the interesting structural and electronic properties of the one dimensional icosahedral α-B_{12} chains especially the infinite chain, the question arose of what will happen if we tried to form ring structures of different shapes and sizes? Would the structural and electronic properties of such structures be interesting? The different sizes of rings that were considered are constructed by 4, 5, 6, 7, 8 and 9 balls. Due to the restrictions in movements for the B_{12} balls in 0 K, we decided to heat the structures to 300 K hence

providing more freedom for the balls to either rotate or vibrate and finally cool down from 300 K to 0 K. We found that consistently, there are more inter icosahedral bonds between two and three balls due to the rotation of the balls, as compared to the chains. We also found that rings having 4, 6 and 8 balls keep the plane, while rings with 5, 7 and 9 balls tend to move out of plane and they have the tendency of joining together. The types of inter icosahedral bonds, cohesive energy, and energy gap of each structure are given in Table 3 below. The number of bonds is indicated as S for single, D for double or two bonds, and T for triple or three bonds.
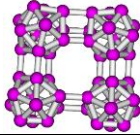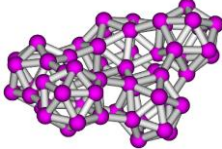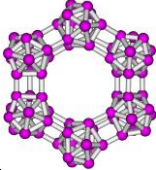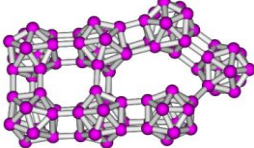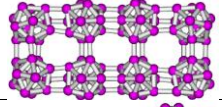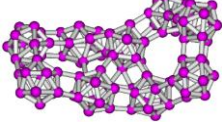
Ring structures	Cohesive Energy (eV)	Energy gap (eV)	Bond Types
	-4.291	0.682	1D, 3T
	-4.202	0.863	1S, 1D, 3T
	-4.317	0.744	6T
	-4.317	0.704	1S, 1D, 6T
	-4.347	0.087	2D, 8T
	-4.318	0.675	7S, 1D, 9T

Table 3. Cohesive and gap energies for different icosahedral ring structures with the different number of bond types. S is for single, D for double and T is for three or triple bonds.

As can be noticed from the final stabilized structure, the icosahedron symmetries are well kept. Even after the rotations they go through for a reconstruction of the rings, except for rings with 5 B_{12} balls and 9 B_{12} balls in which one of the icosahedron has its symmetry broken. Ring with 8 balls has the structure of two ring 4 joined together with the most favorable energy among all rings but has metallic properties as can be seen from table 3. We found that ring with 6 balls was the most interesting among all the rings considered. The structure has been found to be very rigid after the first relaxation at 0 K and even heating it to 300 K and cooling back to 0 K, it did not change the bonding configuration. Ring with 6 balls is, therefore, structurally stable, energetically favorable, and has semiconducting properties. Hence the question was what would happen if two such relaxed structures are placed adjacent to each other? Very interestingly, we found that after 3000 MD steps, a new stable structure of 12 icosahedrons is formed with a favorable cohesive energy of -4.346 eV which is 0.029 eV lower than that of the single ring of 6 icosahedrons but with metallic properties. The total energy per atom with respect to the number of MD steps is shown in figure 14 below. We have presented these results on APS March Meeting in 2014 [59].
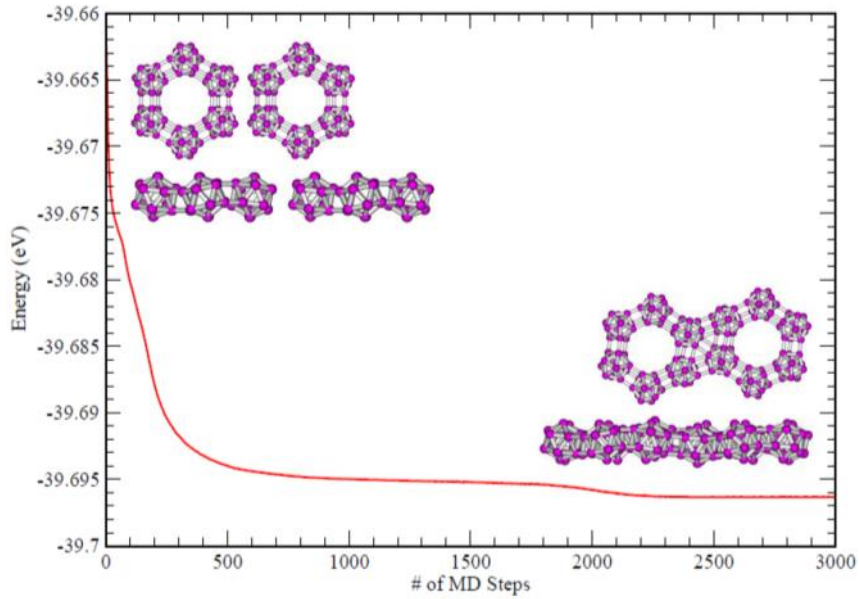
Figure 14. Energy vs number of MD steps for relaxation of two isolated ring 6 structures with the top and side views of the initial and final structures shown by the insets.

3.4 Two-dimensional icosahedral α-B_{12} structures.

Due to the structural stability and semiconducting properties found with the 6 membered rings in our studies, we had the question about the possible existence of two dimensional structures based on icosahedral B_{12} and also what would be their possible electronic properties. To create the different two dimensional B_{12} based structures, a planar cut was done on the α-B structure and a sheet of purely B_{12} structures was obtained. From the obtained B_{12} structure, a primary unit cell was defined and based on the nomenclature in [6] such structure was named δ_6 sheet.
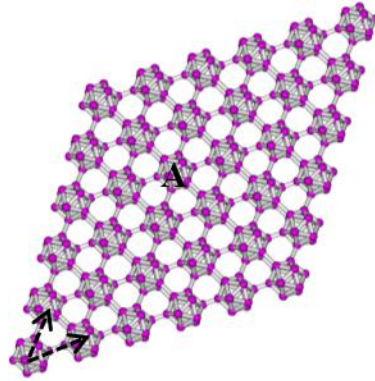
Figure 15. Initial triangular 6x6 icosahedral B_{12} based structure called δ_6. The black dashed arrows show the lattice vectors of the primary unit cell.

From the triangular structure δ_6, two other B_{12} based structures are obtained through a creation of different vacancies on the δ_6, namely the icosahedral δ_4 and icosahedral α sheets as shown in Fig. 16. The icosahedral α sheet was obtained by creating 4 vacancies through the removal of 4 icosahedral B_{12} balls at the different corners of the triangular 6x6 sheet, while the icosahedral δ_4 based structure was obtained by creation of 9 vacancies from the triangular δ_6 sheet.
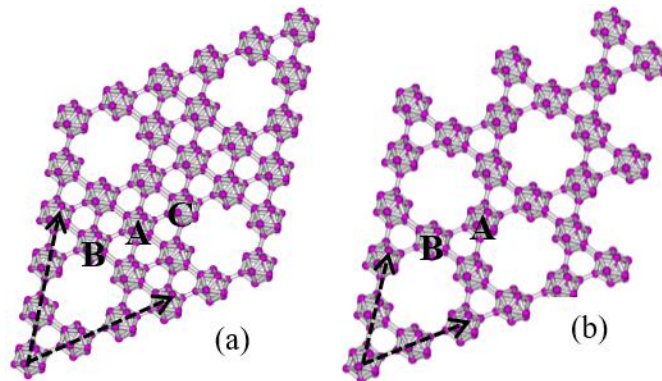
Figure 16. Input structures for icosahedral α (a) and icosahedral δ_4 (b) B_{12} based structures. The black dashed arrows show the lattice vectors of the primary unit cell for each icosahedral sheet structure.

Lattice constant optimizations for these three (α, δ_4 and δ_6) icosahedral structures were performed using both our semi empirical method (SCED-LCAO) and first principles calculations (VASP package). In the following we will give the energetics of the three sheets together with their structural and electronic analyses. To perform the lattice constant optimization in SCED-LCAO, different super cells were used depending on the structure. For the icosahedral δ_6 structure, a 6x6 super cell was used in the real space structural optimization; while for icosahedral δ_4 a 3x3 super cell was used and finally a 2x2 super cell for the icosahedral α sheet. The calculations were performed using a time step of 1.2 fs and the forces were set to less than or equal to 10^{-2} eV/Å. Structurally, the three sheets are also different in terms of the icosahedral B_{12} balls in them. For δ_6 in figure 15, all icosahedral B_{12} balls have the same types of bonds which are 4 single covalent bonds that will be denoted by the letter S and 2 two directional covalent bonds linking two different B_{12} balls that will be denoted by the letter D. Since all icosahedrons are the same in the δ_6 sheet, the ball type A (see Fig. 15) is used for them. For the icosahedral B_{12} δ_4 sheet (figure 16 (b)) two types of icosahedrons are observed, type A where the icosahedron is bonded to 4 other icosahedrons with an S bond that is it has 4 different S bonds and type B where the icosahedron has 6 total bonds 2S and 2D bonds. For the icosahedral B_{12} α sheet (figure 16 (a)) three types of icosahedrons are observed A, B and C. Type A icosahedron is analogous to the single type A in the icosahedral δ_6 sheet with 4S bonds connected to 4 different icosahedrons and 2D bonds connected to 2 different icosahedrons hence a total of 8 bonds; type B icosahedron has a total of 7 possible bonds 3S and 2D while type C has a total of 6 bonds, 4S and 1D bonds. The energetics obtained after our lattice constant optimization using SCED-LCAO are shown in figure 17 below with the optimized lattice constants for

δ_6 being 2% less than that of α-B (with $a^* = 0.98 * a_0$ or $a^* = 8.070$ Å) while both δ_4 and

α icosahedral B_{12} sheets have their optimized lattice constant 1% less than that of α-B.

From the results obtained, we found that δ_6 sheet was the one with the most favorable

energy among all three considered structures. As mentioned at the beginning of the section,

we validated our results obtained with SCED-LCAO by the DFT based package VASP.
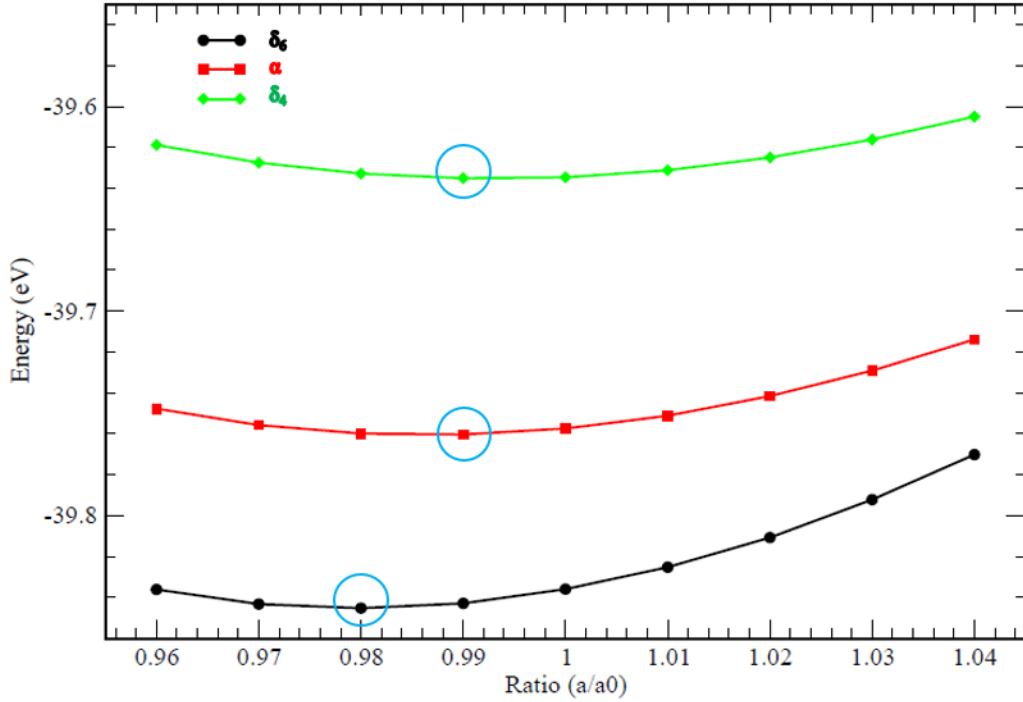
Figure 17. Lattice constant optimization using SCED-LCAO method for the icosahedral sheets based structures δ_6 (black), α (red) and δ_4 (green). Note that a_0 is obtained from α-B and is 8.23479 Å.

During our calculations with VASP, the Vanderbilt ultra-soft pseudo-potential [60, 61] was used to describe the interactions between the core and the valence electrons and for exchange-correlation potentials, the GGA PW91 [62] was used. For the convergence of our energy calculations, the cut off energy for the plane wave basis sets was fixed to be 321.5 eV and the k points were set according to the Monkhorst-Pack scheme with a k-point mesh of 6 x 1 x 6 for the icosahedral δ_6 sheet, 4 x 1 x 4 for the icosahedral δ_4 and 2 x 1 x 2

for the icosahedral α sheet with the primitive unit cell for each sheet being used to do the calculations. To avoid any interactions between two different sheets within the periodic conditions, a vacuum region of 15 Å was created. Structurally, we can point that in both methods the optimized and relaxed sheets kept the planar structure and using the first principle calculations the optimized lattice was found to be 2.5% less than that of α-B in the icosahedral δ_6 structure while for both icosahedral α and δ_4 sheets the optimized lattice constants were found to be 0.4% less than that of α-B. Figure 18 shows the relative energy per atom defined as RE:

$$RE = Total\ E/atom(system\ under\ consideration)$$

$$- Total\ E/atom\ (fully\ relaxed\ \delta_6\ sheet\ at\ equilibrium)$$

which is the difference between the total energy per atom of the system under consideration (δ_6, δ_4 and α) and the total energy per atom for the fully relaxed δ_6 sheet at equilibrium. We can note that δ_6 is the most favorable structure in terms of energies for both SCED-LCAO and DFT and at the same time in terms of the shapes of the different energy plots. The stability and also possible existence of these structures was further investigated through the calculations of their phonon frequencies using VASP by solving the dynamical matrix or the force constant matrix at the gamma point and we found that the lowest vibrational frequencies occur at 216.640 cm^{-1} for icosahedral δ_6, 38.116 cm^{-1} for icosahedral α and 34.416 for icosahedral δ_4 sheet. These positive lowest vibrational frequencies suggest that the structures are stable and can possibly be synthesized if the right conditions are met. The favorability in terms of energies of the icosahedral δ_6 sheet can be explained by its different bonding types compared to the other sheets. As mentioned earlier in the icosahedral δ_6 sheet, each icosahedron has a maximum number of 8 bonds with 4 covalent bonds of S

type and 2 directional covalent bonds of type D which means stronger interactions between any given icosahedron and its immediate neighbors.
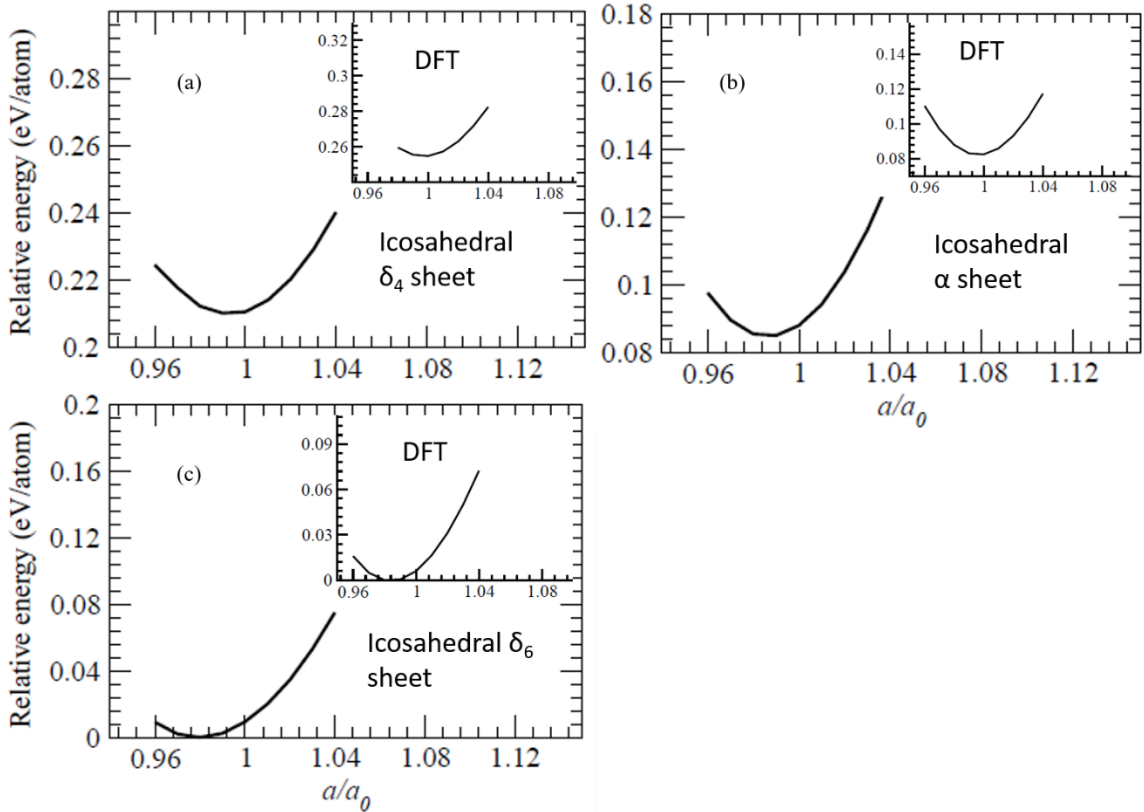
Figure 18. The relative energy per atom versus the ratio of the lattice constant of icosahedral sheets with respect to that of α-B. (a) Icosahedral δ_4 sheet, (b) icosahedral α sheet and (c) icosahedral δ_6 sheet. The insets show the DFT results for the different structures.

While in the icosahedral α sheet (figure 16(a)) the icosahedrons with type B have one less covalent bond of the type S and the B_{12} of type C have two less directional covalent bonds or one less D hence in both cases they interact with one less icosahedron compared to the δ_6 sheet; and for the δ_4 icosahedral sheet, both types A and B icosahedrons interact with 4 icosahedrons and as already discussed the type A icosahedrons have a total of 4 covalent bonds which are all S bonds while the B type icosahedron has a total of 6 bonds with 2S covalent bonds and 2D directional covalent types. The structural properties of these

two dimensional icosahedral sheets have been further determined through their pair and angle distribution functions and summary of these two functions compared to that of a single icosahedron B_{12} revealed a change in terms of intra bonding and angles. The pair distribution functions for all three structures show a broadening of the first peak which identifies the nearest neighbor bonding but not only between atoms of the same icosahedron but also between two atoms in two different icosahedrons. For the next nearest neighbors, we noticed the appearance of different peaks also identified as coming from both within a given icosahedron and also between two icosahedrons as shown by the different arrows in figure 19 (a). As the coordination number of B_{12} balls decreases, we notice that the intensities for both the nearest neighbor and next nearest neighbor peaks decrease.
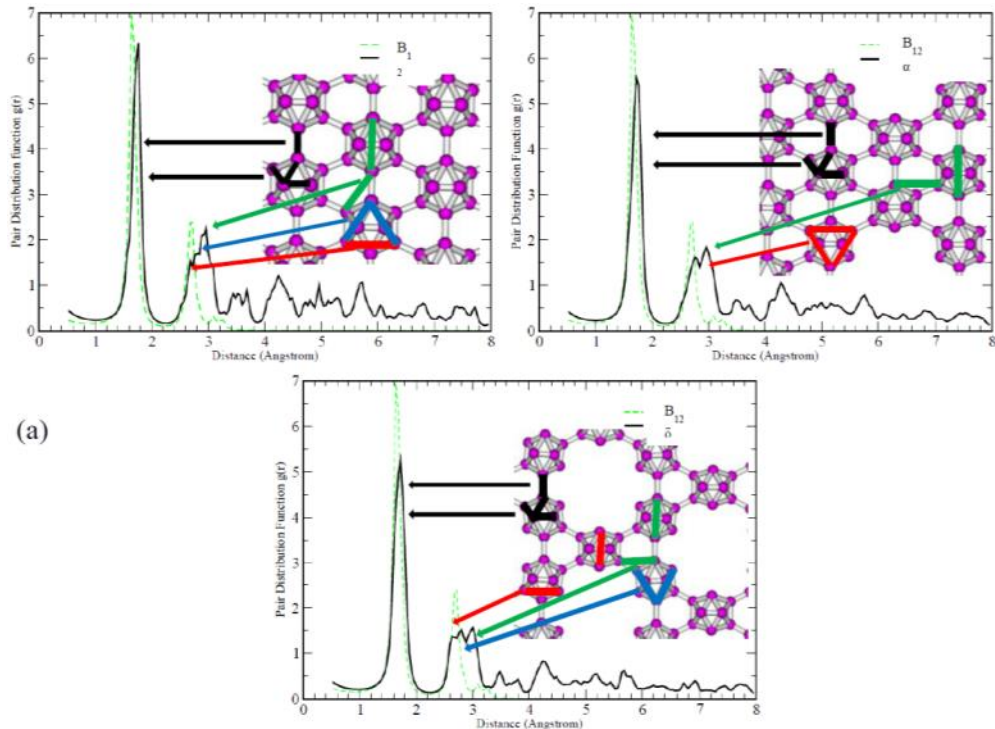
Figure 19. (a) Pair distribution function for icosahedral based sheets δ_6 (top left), α (top right) and δ_4 (bottom panel). Insets are partial cuts of the different structures with the different types of bonds identified by the arrows with black for NN and green, red and blue for the different NNN distances. The green dashed curve is the pair distribution function for isolated B_{12}.

The angle distribution functions shown in figure 19 (b) are a comparison between the sheets and a single icosahedron and it can be noticed that the small deformations on the icosahedrons due to the different types of interactions with their neighbors are shown by the smaller angles accounting for triangles less than 60º which are the dominant angles in a single icosahedron. For the angles between 98º and 130º, in a single icosahedron they are represented by a single broad peak while for our two dimensional icosahedral based sheets, we have distinct peaks identifying this range of angles within a single icosahedron of a given sheet but also angles between two different icosahedrons.
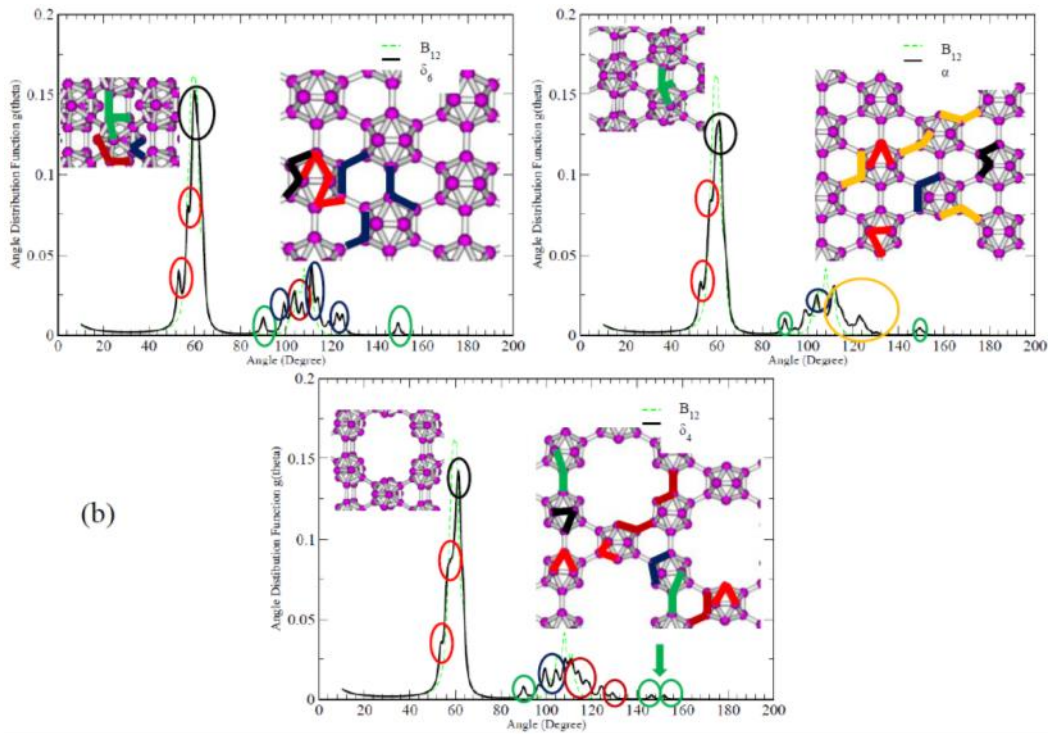
Figure 19. (b) Angle distribution functions for icosahedral based sheets δ_6 (top left), α (top right) and δ_4 (bottom panel). Insets are partial cuts of the different structures. Angles are shown by the different colored circles with light red and black for angles within an icosahedron between 50 and 60º, dark red, dark blue and yellow for angles between the ranges 98 to 130º and green for 90º and 150º angles. The green dashed curve is the pair distribution function for isolated B_{12}.

Two particular angles are the 90º and the 150º angles shown by the green circles in figure 19 (b). Both of them are angles along one of the directional covalent bonds from one icosahedron to another forming either a right angle when connected to the second atom forming another directional bond or when connecting with one of the vertices of the icosahedron. It can be noticed that both angles are not present in the angle distribution of a single icosahedron and their intensities decreases as the coordination number of icosahedral B_{12} decreases and will tend to disappear as the interactions between the icosahedrons weaken. In figure 19 (c), a synthesis of the pair and angle distribution functions of the three icosahedral sheets under consideration compared to α-B bulk is shown. From the pair distribution function curve, the broadening of the curves for the three sheets earlier discussed can be observed when compared to that of the α-B which can be explained by the deformation as already stated of the icosahedrons in the different sheets. Another noticeable different between the curves of the α-B and that of the sheets is the small peak appearing at around 2.0 Å in the α-B curve while disappearing in the sheets' curves. This peak accounts for the directional covalent bonds which are longer in the α-B bulk in the order of 2.03 Å while shorter in the sheets between 1.75 to 1.82 Å.

The bond lengths distributions of the icosahedral sheets compared to that of a single icosahedron B_{12}, α-B and the finite icosahedral chain is summarized in table 4 where the intra-icosahedral bonds are denoted by b_{intra}, b_{inter} for the inter-icosahedral bonds and the total number of S bonds for a given icosahedral type is identified as N^S and N^D for the total number of directional bonds. As stated above, the slight deformation of the icosahedrons in the two dimensional sheets suggested by the broadening of their respective pair distribution curves which is also confirmed by their wider ranges compared to both the

single icosahedron B_{12} and the α-B. The inter-icosahedral bonds on the other hand the sheets have agreements with α-B in the S type covalent bonds while the infinite chain has longer S bonds and for the directional D bonds as already mentioned have shorter therefore more interactions compared to α-B.
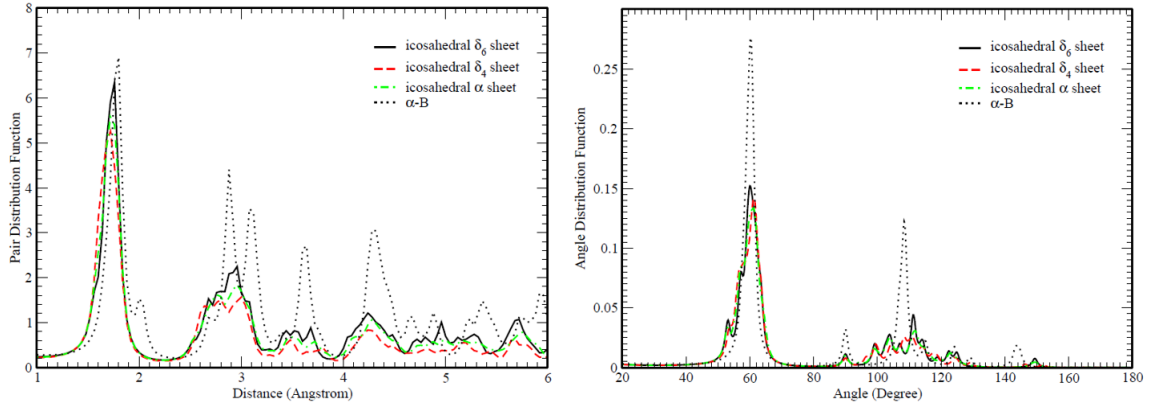
Figure 19. (c) Pair and angle distribution functions for icosahedral $δ_6$ sheet (solid black), icosahedral $δ_4$ sheet (dashed red), icosahedral α sheet (dashed green) and α-B (dotted black)

System		b_{intra} (Å)	b_{inter} (Å)	N^S	N^D
Icosahedron B_{12}		1.61-1.75	NA	NA	NA
α-B		1.73-1.80	1.67 (S); 2.03 (D)	6	4
Icosahedral chain		1.62-1.75	1.76 (S)	2	0
Icosahedral sheets	$δ_6$	1.56-1.77 (Type A)	1.69 (S); 1.80 (D)	4	2
	α	1.56-1.77 (Type A)	1.69 (S); 1.82 (D)	4	2
		1.57-1.80 (Type B)	1.69-1.72 (S); 1.82 (D)	3	2
		1.59-1.79 (Type C)	1.69-1.72 (S); 1.75 (D)	4	1
	$δ_4$	1.59-1.79 (Type A)	1.68 (S)	4	0
		1.59-1.80 (Type B)	1.68 (S); 1.82 (D)	2	2

Table 4. Structural properties for icosahedron B_{12}, α-B, infinite icosahedral chain and icosahedral sheets ($δ_6$, α and $δ_4$). b_{intra}, b_{inter}, N^S and N^D are defined in the text.

The electronic properties of the two dimensional icosahedral based sheets was also investigated and through the calculations of their electronic density of states, we found that the icosahedral $δ_6$ and $δ_4$ sheets have semiconducting properties with their calculated gap energies being 0.520 and 0.385 eV respectively while the icosahedral α sheet have a near gapless energy at 0.018 eV. Compared to their monolayer counterparts, which were found

to have metallic like energy gaps, we found that the sheets have interesting electronic properties even though the obtained gaps are smaller to that of α-B which was found to be close to the optical gap of 2.0 eV. The different density of states of the three sheets together with that of the infinite icosahedral chain and the α-B are presented in figure 20 below.
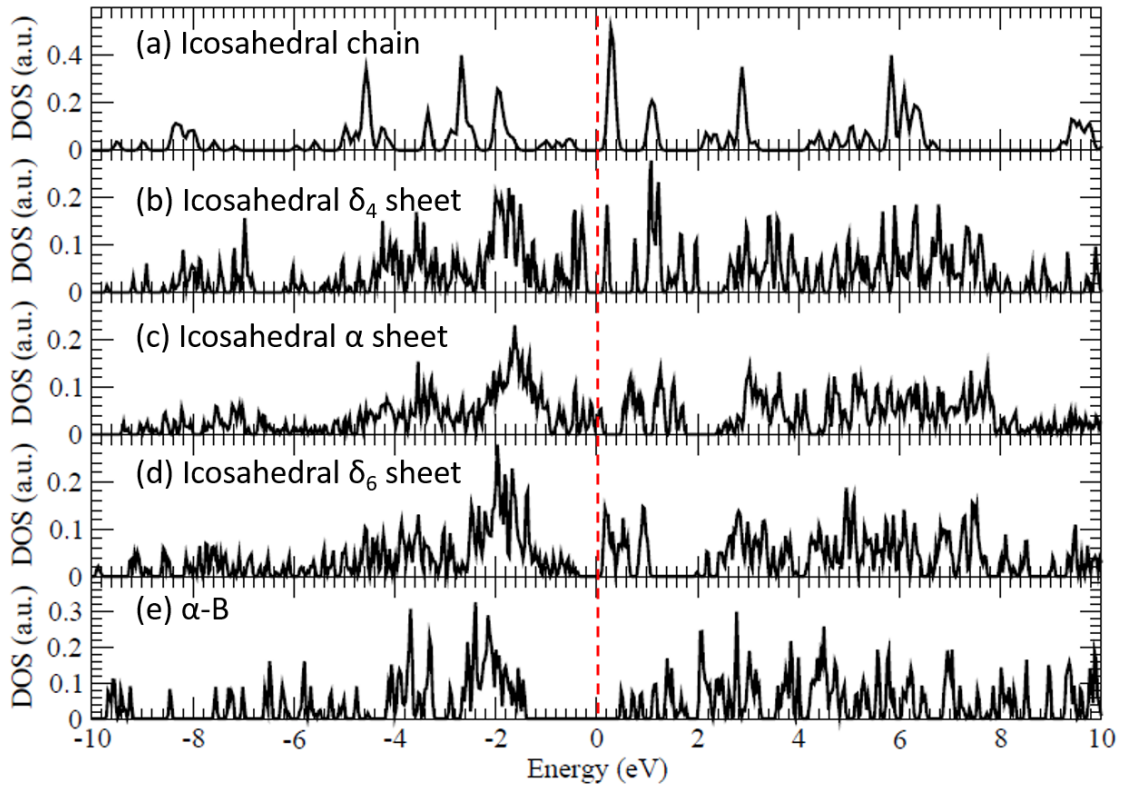
Figure 20. Density of states for icosahedral B_{12} based structures; (a) icosahedral infinite chain, (b) icosahedral δ_4, (c) α, (d) δ_6 sheets and (e) crystalline α-B. The Fermi Energy was set at 0 and is shown by the red dashed line.

3.5 Energy barriers

The calculations of the vibrational frequencies for the two-dimensional structures (δ_6, α and δ_4) in the previous sub-section (3.4) revealed that they all have positive lowest frequencies suggesting possibilities for the structures to be synthesized. The two-dimensional δ_6 however was found to be the most stable among all three structures, hence the need to find possible pathways to create α and δ_4 sheets from an existent δ_6 sheet. To

52

make the transition from δ_6 to α, four icosahedral B_{12} were gradually removed (as indicated in sub-section 3.4) from the 6x6 unit cell of the δ_6 sheet along the direction perpendicular to the sheet (see Fig. 21(a)). The transition from δ_6 to δ_4 was made by gradual removal of nine icosahedral B_{12} units (as in sub-section 3.4) from the 6x6 unit cell of the δ_6 sheet along the direction perpendicular to it (see Fig. 21(b)). Likewise, the transition from α to δ_4 was made by gradually removing five icosahedral B_{12} units from the 2x2 unit cell of the α structure along the direction perpendicular to it and at the same time by moving three icosahedral units towards the center of an adjacent hexagonal hole (see Fig. 21(c)). Such transition procedures were performed until further moves along the perpendicular directions to δ_6 or α do not change the energy of the combined systems. To estimate the energy barriers, the energy difference between the initial stage (δ_6 when transition is $\delta_6 - \alpha$ or $\delta_6 - \delta_4$ and α when transition is $\alpha - \delta_4$) and the final stage is calculated. The energy of the final stage is defined as the combination of the energy of the system under consideration (α or δ_4) plus the energy of the number of icosahedral units removed along the perpendicular direction (4, 9 or 5). We found that the transition from δ_6 to α requires $0.17\ eV/atom$ ($\sim1700\ K$), the transition from δ_6 to δ_4 requires $0.38\ eV/atom$ ($\sim3800\ K$) and the transition from α to δ_4 requires $0.27\ eV/atom$ ($\sim2700\ K$) (as shown in Fig. 21 (d)). It was therefore found that it requires more energy to make the transition from δ_6 to δ_4. With the high-energy barriers reported above, the icosahedral sheets are considered to be energetically and thermally stable and a possible pathway would be to produce α from δ_6 since the energy barrier between the two is lower and then produce δ_4 from α sheet. We have published all the results for the two-dimensional icosahedral sheets in Nanotechnology in 2015 [58].
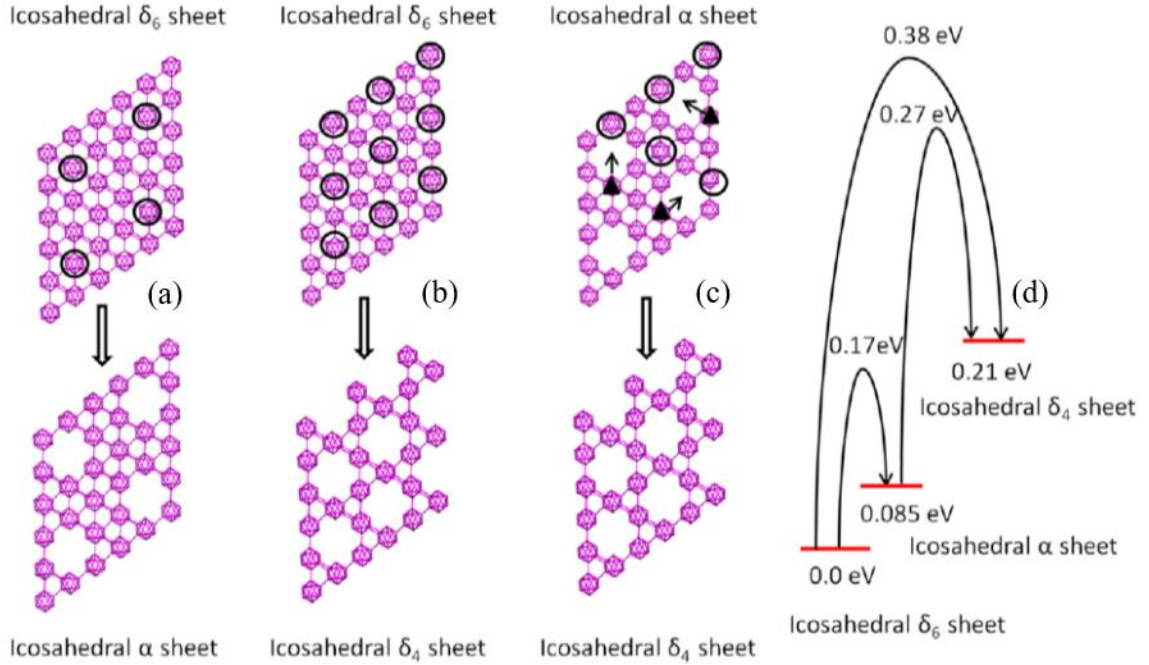
Figure 21. Transition paths (a) δ_6 (top) – α (bottom), (b) δ_6 (top) – δ_4 (bottom) and (c) α (top) - δ_4 (bottom). Black circles indicate the removed icosahedral units and black triangles in top panel of (c) indicates the direction of movement of the icosahedral balls.

3.6 Single layered α-Tetragonal B$_{50}$

Bulk α-tetragonal B$_{50}$ [63] is made up of four icosahedral B$_{12}$ centered at $\left(\frac{1}{4}, \frac{1}{4}, \frac{1}{4}\right)$; $\left(\frac{3}{4}, \frac{3}{4}, \frac{1}{4}\right)$; $\left(\frac{3}{4}, \frac{1}{4}, \frac{3}{4}\right)$ and $\left(\frac{1}{4}, \frac{3}{4}, \frac{3}{4}\right)$ and two individual Boron atoms at positions $\left(0, 0, \frac{1}{2}\right)$ and $\left(\frac{1}{2}, \frac{1}{2}, 0\right)$ with lattice constants $a_0 = 8.75$ Å and $c_0 = 5.06$ Å. Figure 22 shows the structures of the bulk α-Tetragonal B$_{50}$.
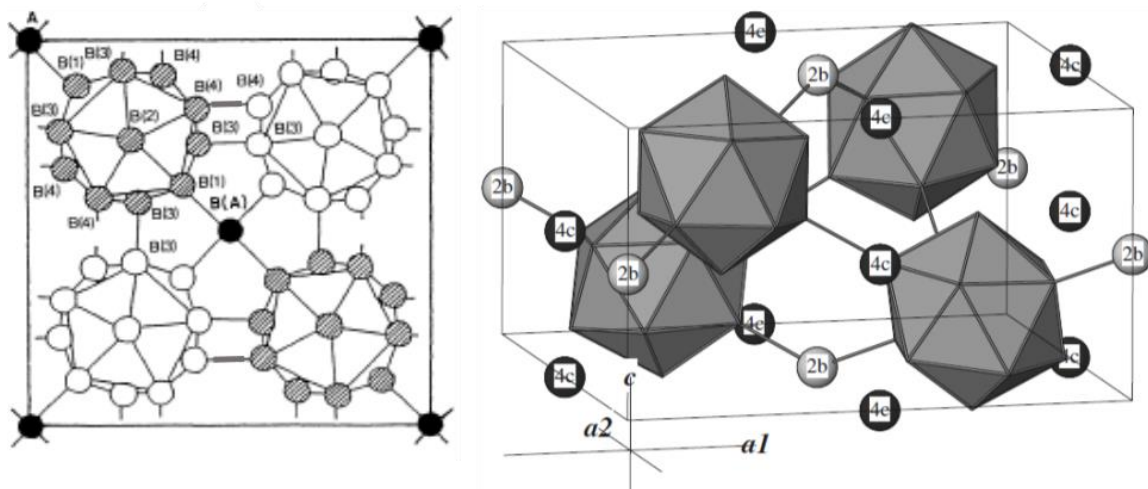
Figure 22. Top (left) [64] and 3D (right) [63] views of α-Tetragonal B_{50} structure. For notations on figure see corresponding references.

There are three types of co-ordination which can be seen from the figure 22: the fivefold intra-icosahedral co-ordination at the boron atoms inside the icosahedron, the sixfold inter-icosahedral bonding at the boron atoms bonding the neighboring icosahedrons, and the fourfold bonding at the single isolated boron atoms in the interstitials. The third type of bonding is unique in linking the icosahedrons together to form a three-dimensional network in the bulk α-tetragonal B_{50}. Compared to rhombohedral α-B, bulk α-tetragonal B_{50} was not stable at ambient temperature and pressure, and can only be synthesized at high temperature (1200-1300 ℃) and high pressure (8-9 GPa) [63]. The reason why we are attracted by this system is because more recently, Xu, J., et al., [10] have successfully synthesized ultrathin single-crystalline boron nanosheets. The Raman spectrum and the HRTEM image provide that the structure of these sheets can be attributed to the (002) and (200) lattice planes of α-tetragonal B_{50} phases [10]. The ultrathin nature of their structure was also confirmed by the almost transparent image of the structure and behaves as a p-type semiconductor with high carrier mobility (see Fig. 23).
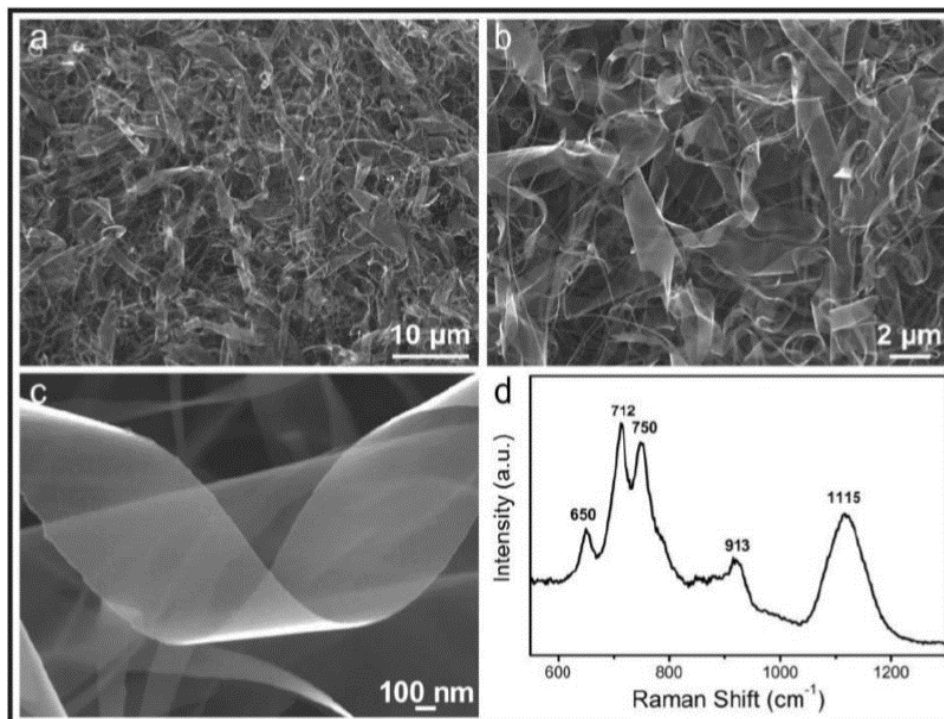
Figure 23. SEM pictures at different magnifications in a and b, enlarged image in c and Raman spectrum in d for Ultrathin Boron Nanosheets presented by [10].

This was the first time to show experimentally the existence of the 2D boron sheet formed by the icosahedron B_{12}. This experimental observation intrigued us to undertake a study that aims to explore whether a single layered α-tetragonal B_{50} sheet is stable in computational studies based on SCED-LCAO and DFT. Should this investigation find the single-layered structure of B_{50} to be unstable, this would imply that experiments are observing multiple layers or a thin film of B_{50}. In this case, theoretical studies should determine the critical thickness (or layers) when B_{50} becomes stable.

The structure of unrelaxed single layered α-tetragonal B_{50} sheet is shown Fig.24.
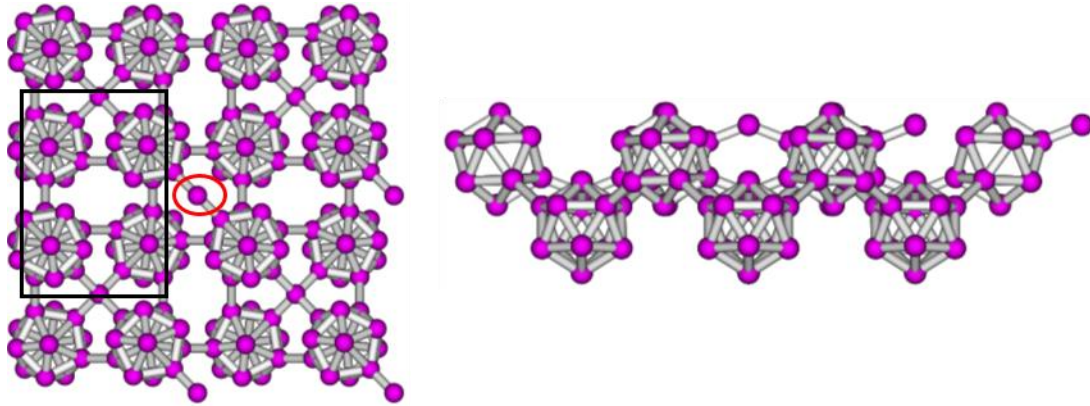
Figure 24. Top view (left) and side view after a 45° angle rotation (right) for a single layered α-tetragonal B_{50} sheet.

It can be seen from Fig. 24 that the bonding nature in the single layered α-tetragonal B_{50} sheet is quite different from their bulk counterpart. For instance, one of the double inter-icosahedral bonds between B_{12} balls in the bulk disappeared in the single layered sheet (*e.g.*, as indicated by the black square in Fig. 24), and some of the isolated boron atoms also lost their bonds to the neighboring icosahedron which is key in linking the icosahedrons together to form a three-dimensional network (see red circle in Fig. 24). In particular, the icosahedrons are not located in the plane but up and down alternatively (see the side view in Fig. 24). Therefore, there are many dangling bonds on the icosahedrons, including isolated boron atoms in a single layered α-tetragonal B_{50} sheet, implying the sheet might be unstable and a surface reconstruction to stabilize the sheet is required. To test the stability of this sheet, we optimized the structure based on SCED-LCAO molecular dynamics as well as using the DFT method as implemented in the VASP package.

In SCED-LCAO calculations, we used a 2x2 super cell in real space and the optimized structure were determined with forces converging to $< 10^{-2}\ eV/atom$. On the

other hand, in DFT-VASP calculations, we used a 1x1 super cell with similar force convergence criterion. We tested our DFT results with two different types of pseudopotentials and exchange correlation potentials. In one case, we used an ultra-soft (US) pseudopotential [60, 61] with generalized gradient approximation GGA PW91 [62] for exchange correlation and in the other case, we used the projector augmented wave (PAW) [65] with PBE [66] for exchange correlation. The typical k-point mesh used in energy calculation was 3x3x1. The optimized lattice constant (see Fig. 25) for the B_{50} sheet with SCED-LCAO was found to be $0.96a_0$ while for VASP we found $0.97a_0$ and $0.98a_0$ for US and PAW respectively, where $a_0 = 8.75$ Å is the predicted lattice constant given by [67].
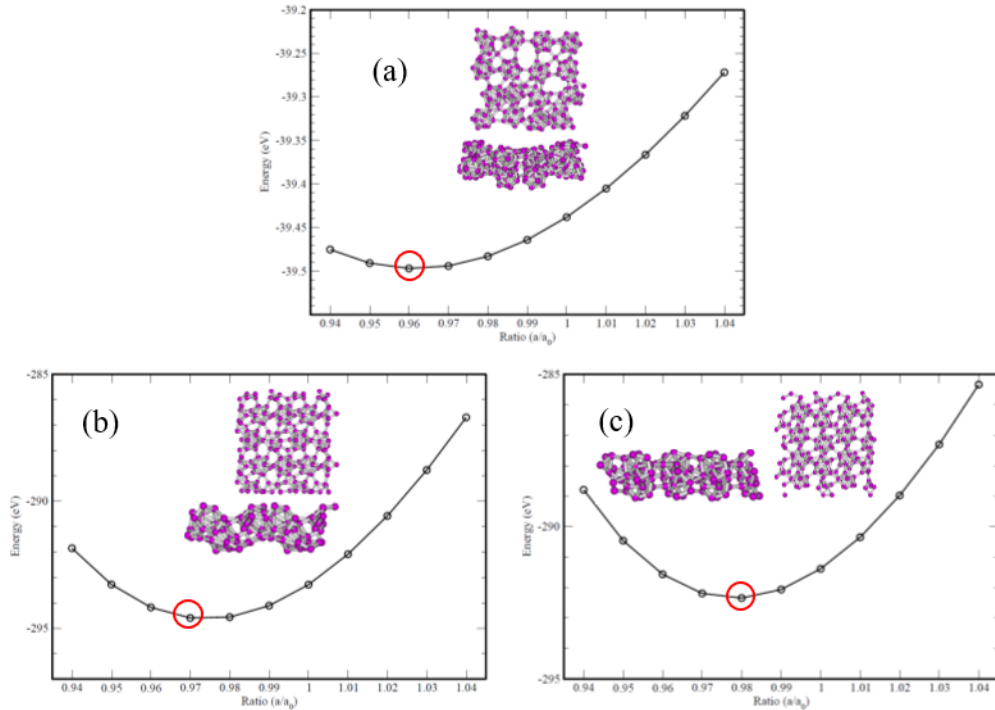
Figure 25. Lattice constant optimization for a single layered α-tetragonal B_{50} sheet using (a) SCED-LCAO, (b) DFT (US/GGA) and (c) DFT (PAW/PBE). The bulk lattice constant value used here is $a_0 = 8.75$ Å [67].

It was found that, after full relaxation (see the insets in Fig. 25), the reconstructed single layered sheet is structurally stable with positive vibration frequencies, but it totally lost its initial symmetry, and the degree of the distortion is different in all three cases. In all of the three cases we found buckling of the whole structure and a deformation of some of the icosahedral B_{12} clusters. The boron atoms with dangling bonds try to relocate to increase their co-ordination. But, due to the deformation of some icosahedral clusters, the relaxed α-tetragonal B_{50} sheets have two types of intra-icosahedral bonding: one is within a deformed icosahedral cluster and the other is within a regular icosahedral cluster. We also found that for the inter-icosahedral bonds there are single and double bonding types, while for the bonds between the B_{12} clusters and two single boron atoms there are also two different types of the bonding with the isolated or not isolated B atom.

SCED-LCAO

US
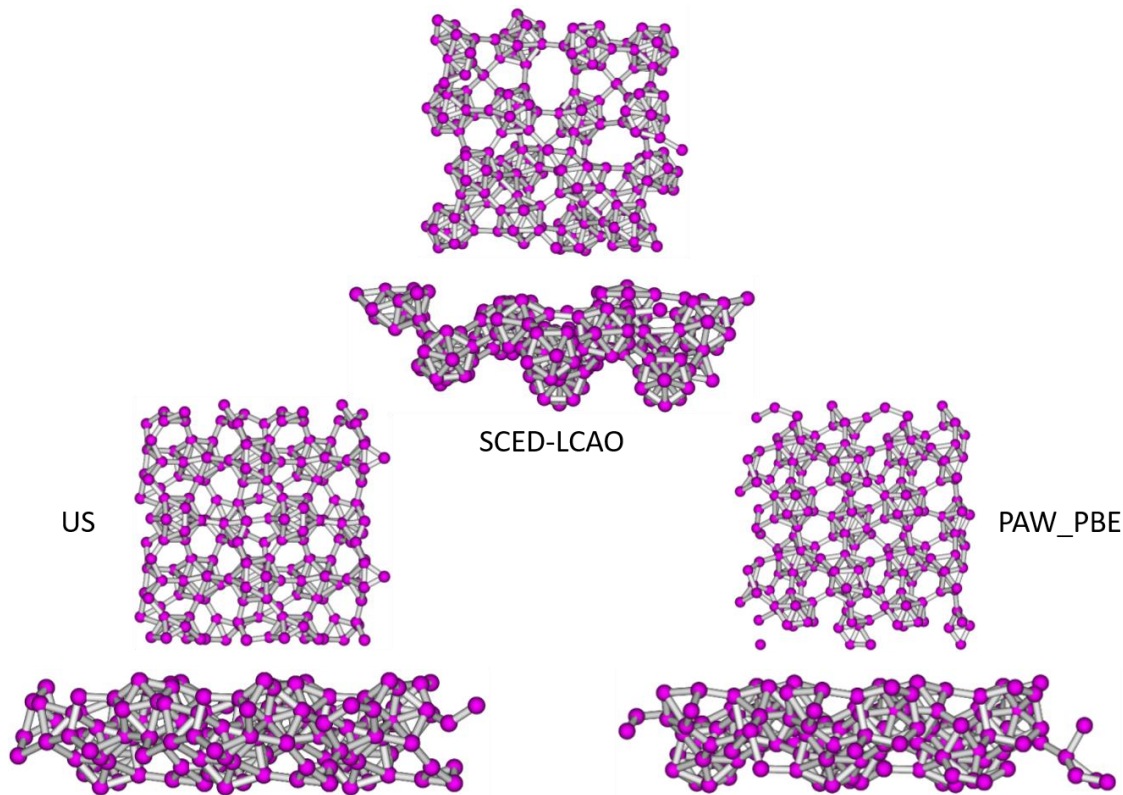
PAW_PBE

Figure 26. Relaxed structures for α-Tetragonal B_{50} sheet using SCED-LCAO, VASP-US and VASP-PAW_PBE

Our simulations suggest that a stable single-layered α-tetragonal B_{50} sheet broke the α-Tetragonal B_{50} symmetry because of the existence of many dangling bonds associated with the isolated boron atoms and icosahedrons. The stability in the α-tetragonal B_{50} symmetry could is expected to be improved in a multi-layer or a thin film of α-tetragonal B_{50} because of the opportunity to reduce the number of dangling bonds in such a system and because it is energetically favorable to reduce the surface to volume ratio. Experimentally synthesized ultrathin sheets have a thickness of about 8-12 nm which translates to about 20 layers. Therefore, we plan to investigate the structural stability of multi-layer sheets starting from two-layered α-tetragonal B_{50}.

CHAPTER IV

PAREMERIZATION OF THE SCED-LCAO HAMILTONIAN FOR GROUP V

ELEMENTS: A ROBUST TEST FOR NITROGEN AS A CASE STUDY

This chapter will focus on developing the parameters characterizing the SCED-LCAO Hamiltonian for the element nitrogen. Since one of the goals of this dissertation is to study the bandgap engineering of h-BN sheets inserted with graphene domains, it is necessary to develop the SCED-LCAO Hamiltonian for the element nitrogen. Prior researchers in the group have developed the SCED-LCAO Hamiltonian for silicon, carbon, and boron. There were also some preliminary attempts to develop the SCED-LCAO Hamiltonian for nitrogen using GaN in the database. In this work, we will expand the database to include other systems and compounds (BN and CN systems) containing nitrogen and we will carry out a systematic study so that the parameters associated with the SCED-LCAO Hamiltonian for nitrogen are robust and transferable.

4.1   Fitting for Nitrogen SCED-LCAO parameters
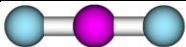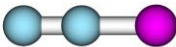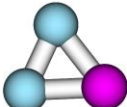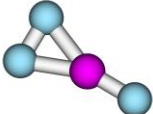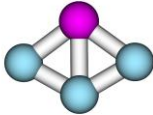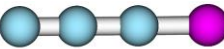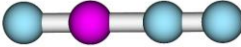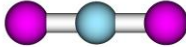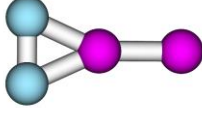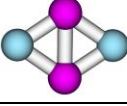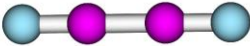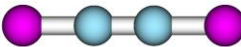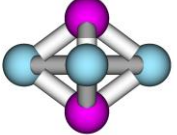
To develop SCED-LCAO parameters for nitrogen element, a database of different types of heterogeneous clusters that contain nitrogen and another element will be used. The database used in our study consists of properties such as bond lengths and cohesive energies, which are obtained using ab-initio approaches (either VASP or Gaussian). For each of the clusters in our database, we calculate properties, such as the bond-length and

cohesive energies, both via SCED-LCAO and ab-initio approaches and then we use a least square method (Marquadt algorithm) for minimizing the residue. We randomly generate several parameter sets of the SCED-LCAO Hamiltonian, and use the Marquadt algorithm to get the lowest possible residue. The optimization code for finding the best set of parameters for SCED-LCAO Hamiltonian was originally written by a previous graduate student, Dr. Chris Leahy, which was subsequently modified by another graduate student, Dr. Lyle Smith, to circumvent some of the charge self-consistency issues encountered during these optimizations.

Two different strategies were considered for the fitting, depending on the type of nitrogen based clusters during the optimization. One strategy was to use BN and CN clusters while the other strategy used GaN clusters. In both cases the total residue of the different optimizations is monitored with the aim of always having a residue as small as possible with an improvement in the values of the parameters when compared to a previous set. Throughout the fitting, three particular parameters are closely monitored in determining the parameters of the SCED-LCAO Hamiltonian for nitrogen. They are the two off-site Hückel energies described by parameters ε_s' and ε_p' , and the Hubbard term U which describes the strength on-site electron correlations. Our experience shows that the difference in values between ε_s' and ε_p' must be very close to the difference in values between the two onsite orbital energies ε_s and ε_p. We find that either too large or too low values of U will not describe the charge transfers correctly, resulting in incorrect ground state structure and predicting incorrect relative energy of structures.

4.1.1　Nitrogen parameters optimized with BN and CN clusters

As already stated, one approach for obtaining the optimized parameters for SCED-LCAO Hamiltonian for Nitrogen uses a database of properties containing several types of BN and CN clusters. We considered a total of 22 B_nN_m clusters and 17 C_nN_m clusters (n+m ≤10) in the fitting procedure. Tables 5.1 and 5.2 show the database containing clusters of different symmetries and their properties corresponding to B_nN_m and C_nN_m clusters. The physical properties for these clusters were calculated from first-principles methods, and the corresponding results for the optimized parameters of the SCED-LCAO Hamiltonian are shown to assess the quality of the fitting for clusters containing nitrogen. It can be seen clearly from these tables that the SCED-LCAO results are consistent with the DFT results [25], clearly indicating that our SCED-LCAO Hamiltonian for nitrogen can correctly characterize the interactions present in the nitrogen element. The properties given in the database contain all characteristic bond lengths representing a given cluster and its corresponding binding energy (shown within parenthesis).

Clusters (BₙNₘ)	Symmetry	Database References Å, (eV) [25]	SCED-LCAO Results Å, (eV)
	D_{ih}	0.659675 (-0.088449)	0.57696801 (-0.08985155)
	D_{ih}	1.323160 (-0.116296)	1.33959339 (-0.13124683)
	C_{iv}	1.143163 1.456700 (-0.126543)	1.15522522 1.44828062 (-0.12271019)
	C_{2v}	0.648227 1.255078 (-0.126553)	0.62192704 1.22006672 (-0.12032262)
	C_{2va}	0.583497 1.272920 1.456654 (-0.142195)	0.58551443 1.25607078 1.45337274 (-0.14876831)
	C_{2vb}	1.156522 0.858636 0.671727 (-0.130590)	1.16150972 0.81891018 0.62033131 (-0.12337348)
	C_{iva}	1.369382 1.203877 1.122779 (-0.141462)	1.39541651 1.21509313 1.13703854 (-0.14290138)
	C_{ivb}	1.259239 1.395666 1.112110 (-0.154901)	1.22607933 1.46434972 1.13573563 (-0.16097148)
	D_{ih}	1.311856 (-0.141881)	1.24591301 (-0.12675317)
	C_{2v}	0.615391 1.537884 1.341462 (-0.128828)	0.61148444 1.537884 1.25322429 (-0.12721283)
	D_{2h}	1.181049 0.798394 (-0.149559)	1.13197994 0.78632948 (-0.15414776)
	D_{iha}	0.782703 1.310395 (-0.134575)	0.81305716 1.29218386 (-0.13683636)
	D_{ihb}	0.596192 1.413008 (-0.119698)	0.68565586 1.413008 (-0.11660460)
	C_{2vb}	1.170906 0.871357 1.299613 0.019619 (-0.133577)	1.17956408 0.83134489 1.26333222 0.03449571 (-0.12733551)
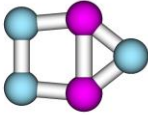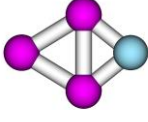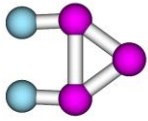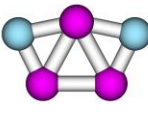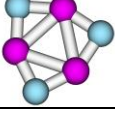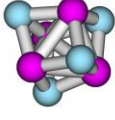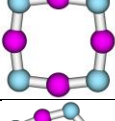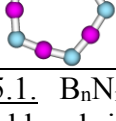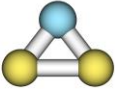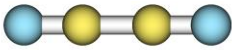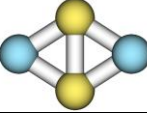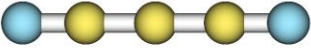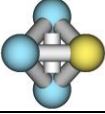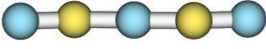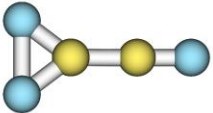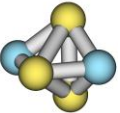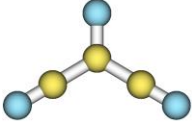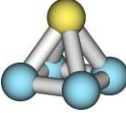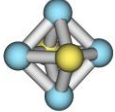
	C$_{2vf}$	0.841462 0.718120 1.060525 1.408541 (-0.150901)	0.88408457 0.70893295 1.01865124 1.43643509 (-0.14975781)
	C$_{2v}$	1.077058 1.418147 0.864972 (-0.138497)	1.08097937 1.39871494 0.864972 (-0.13083305)
	C$_{2va}$	0.964237 0.899674 1.320332 1.306801 (-0.130675)	1.00346356 0.86729849 1.27499972 1.29071038 (-0.12353820)
	C$_{2ve}$	1.403723 0.810052 0.288643 1.200235 (-0.164109)	1.36766111 0.82262378 0.34084446 1.19505750 (-0.16099290)
	D$_{3h}$	1.096560 1.514849 (-0.189761)	1.14535173 1.48036298 (-0.18679473)
	D$_{2d}$	0.919119 1.173999 0.650063 0.830255 (-0.174808)	0.91847910 1.18674703 0.64945912 0.83915222 (-0.18478289)
	D$_{4h}$	1.491329 1.879734 (-0.203256)	1.55925778 1.81894145 (-0.19679969)
	D$_{5h}$	1.916653 2.253138 (-0.209663)	1.97060645 2.18608135 (-0.20129187)

Table 5.1. B$_n$N$_m$ clusters in different symmetries with geometries and binding energies obtained by ab-initio [25] and SCED-LCAO calculations. B (purple) and N (indigo). The ab-initio calculations (Gaussian package) were done by Dr. Lyle Smith.

Clusters (C_nN_m)	Symmetry	Database References Å, (eV) [25]	SCED-LCAO Results Å, (eV)
	C_{2v}	0.790381 1.032042 (-0.152305)	0.790381 1.032042 (-0.15768115)
	D_{ih}	1.375569 1.152190 (-0.200156)	1.24791463 1.24721882 (-0.19502662)
	D_{2h}	0.737351 1.147029 (-0.158600)	0.85994201 1.08621712 (-0.16851971)
	D_{ih}	1.309768 1.182964 (-0.195146)	1.22822829 1.28001647 (-0.21731863)
	C_{3v}	0.885050 1.078976 (-0.113750)	0.86336069 1.11860677 (-0.10038047)
	C_{2va}	1.147810 1.092002 0.597800 0.423120 (-0.183823)	1.11809448 1.12815664 0.50565470 0.51020701 (-.15290536)
	C_{2vb}	1.411641 1.150442 1.039574 0.784888 (-0.170241)	1.411641 1.22782363 1.10012744 0.72738546 (-0.18210087)
	D_{3h}	1.020275 1.054562 (-0.145869)	0.98413625 1.12871523 (-0.17230773)
	C_{2v}	1.240676 0.990182 1.263540 0.736694 0.584440 (-0.191604)	1.12347032 1.06002346 1.263540 0.736694 0.59007508 (-0.19637876)
	C_{4v}	0.985652 1.317528 (-0.120716)	1.09090095 1.23596939 (-0.10434597)
	D_{4h}	1.156781 1.163554 (-0.087302)	1.17961463 1.08059809 (-0.11078869)
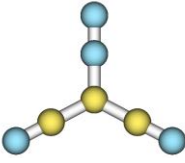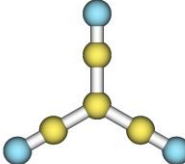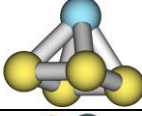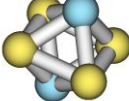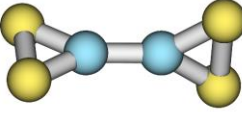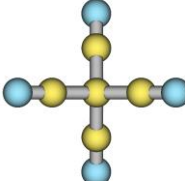
	Symmetry	Ab-initio	SCED-LCAO
	C$_{2v}$	1.251150 1.017708 1.327555 1.118334 0.657546 0.542555 (-0.192238)	1.251150 1.017708 1.327555 1.10346494 0.66854482 0.58796384 (-0.20099080)
	D$_{3h}$	1.405862 1.157188 (-0.204757)	1.30488327 1.21550396 (-0.21735430)
	C$_{4v}$	1.013399 1.249088 (-0.140432)	1.03337243 1.249088 (-0.18533345)
	D$_{4h}$	1.181593 1.041468 (-0.132661)	1.12033221 1.03219016 (-0.17051836)
	D$_{2d}$	0.685372 1.089384 0.761442 (-0.150744)	0.60147098 1.09619391 0.67131896 (-0.21472773)
	T$_d$	1.482883 1.146910 (-0.203655)	1.35417934 1.18486524 (-0.21564890)

Table 5.2. C$_n$N$_m$ clusters in different symmetries with geometries and binding energies obtained by ab-initio [25] and SCED-LCAO calculations. C (yellow) and N (indigo). The ab-initio calculations (Gaussian package) were done by Dr. Lyle Smith.

One particular function to be evaluated during the fitting of different parameters in SCED-LCAO code is the overlap function as defined in equation 11. The overlap function is expected to have the general shape of any overlap curves obtained from ab-initio calculations, and as already indicated in [24], the following constraints must be met:

- The normalized overlap cannot exceed unity;

- The overlap curve must decay to nearly zero within a cutoff to ensure localized behaviors of the Hamiltonian matrix elements defined in Eq. 6.2.
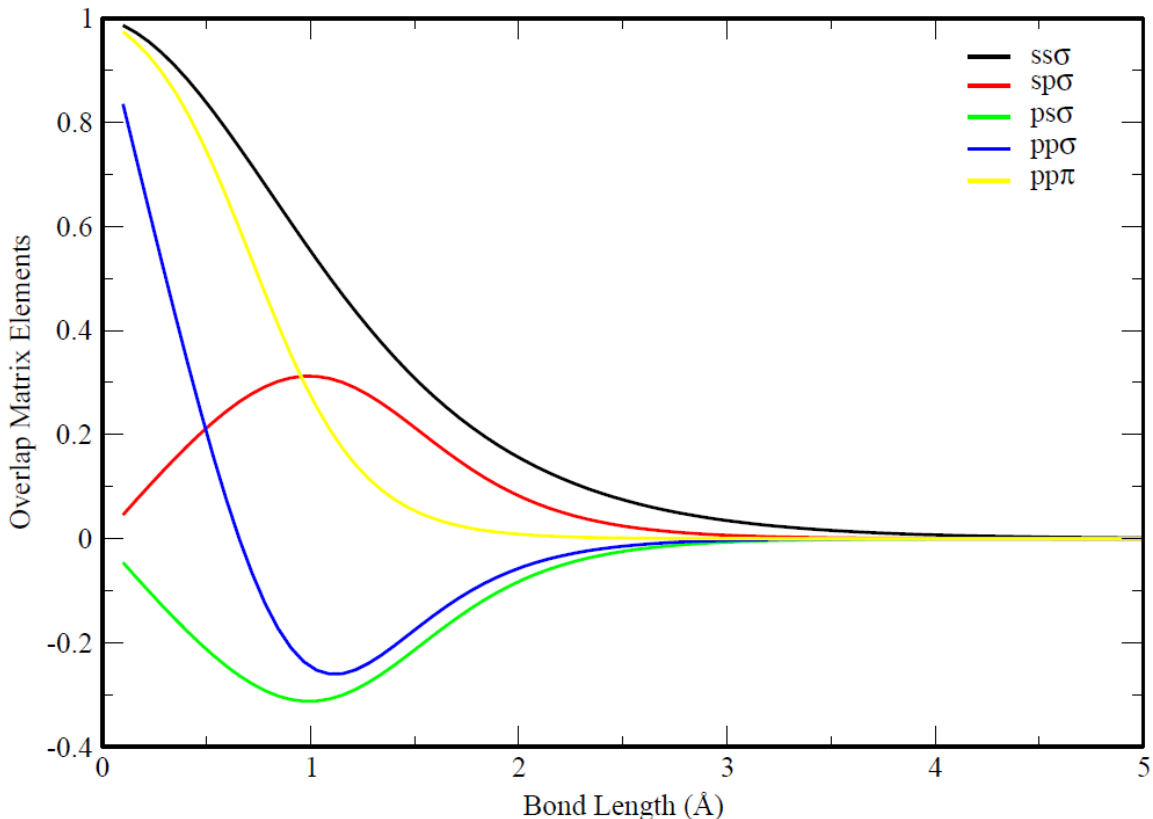
Figure 27. Overlap matrix elements functions for Nitrogen element vs the bond lengths in Å. Color coding shown in the legend of the curves.

A plot of the overlap matrix elements obtained for this first set of presented results is shown in Fig. 27. We can note that only four of the five functions of the overlap matrix elements were fitted for Nitrogen which means that the $ps\sigma$ function was subjected to the condition $S_{ps\sigma} = -S_{sp\sigma}$. Also note that $A_\tau = 1$ for $\tau = ss\sigma$, $pp\sigma$ and $pp\pi$ while $A_\tau = 0$ for $\tau = sp\sigma$, or $ps\sigma$ hence the a total of 12 parameters for the overlap matrix elements will be optimized. The conditions of not exceeding unity and nearly zero tails beyond 5 Å are met within the cut off 8 Å for SCED-LCAO Hamiltonian for nitrogen (see Fig. 27 and 28).
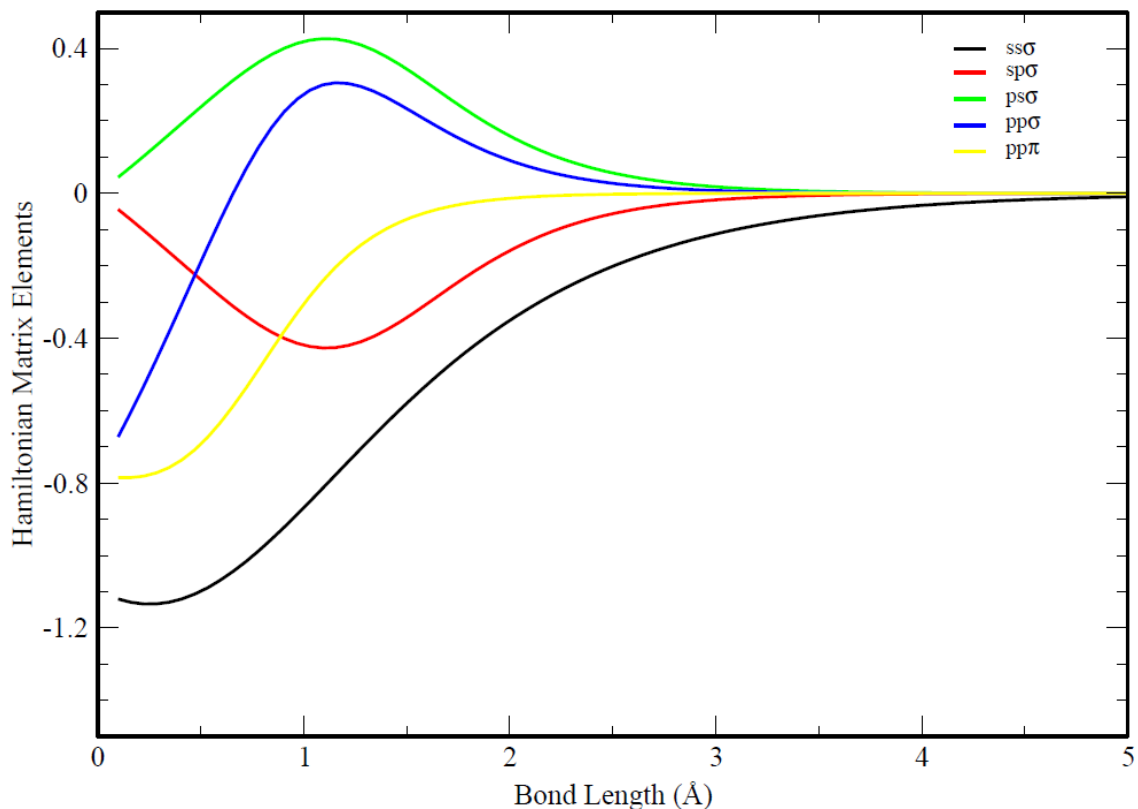
Figure 28. Hamiltonian matrix elements functions for Nitrogen element vs the bond lengths in Å. Color coding shown in the legend of the curves.

Figure 28 shows the Hamiltonian plots for Nitrogen element obtained with the first set of optimization and as expected all curves converged to zero around the cutoff point defined to be 5 Å. The results of the optimized parameters are summarized in table 6 below.

Hamiltonian Parameters for Nitrogen		Hamiltonian Parameters for Nitrogen	
$\varepsilon_s(eV)$	-26.23360	$U(eV)$	14.37890796
$\varepsilon_p(eV)$	-13.84240	$B_Z(\text{Å}^{-1})$	3.54620870
$\varepsilon_s'(eV)$	-29.80655145	$A_N(eV)$	-2.79304279
$\varepsilon_p'(eV)$	-21.13934210	$B_N(\text{Å}^{-1})$	2.01457266
$W_s^0(\text{Å}^{-1})$	0.58870680	$\alpha_N(\text{Å}^{-1})$	3.88124844
$W_p^0(\text{Å}^{-1})$	-0.35574524	$d_N(\text{Å})$	1.03590259
$\alpha_{s,w}(\text{Å}^{-1})$	1.48115559	$\alpha_{NC}(\text{Å}^{-1})$	0.43919196
$\alpha_{p,w}(\text{Å}^{-1})$	1.80524342	$\alpha_{NB}(\text{Å}^{-1})$	0.59121571
$\alpha_K(\text{Å}^{-1})$	0.35974085		
Overlap Parameters for Nitrogen		Overlap Parameters for Nitrogen	
$B_{ss\sigma}(\text{Å}^{-1})$	0.60241762	$B_{pp\sigma}(\text{Å}^{-1})$	-1.51869428
$\alpha_{ss\sigma}(\text{Å}^{-1})$	1.77820450	$\alpha_{pp\sigma}(\text{Å}^{-1})$	3.41293853
$d_{ss\sigma}(\text{Å})$	0.26212788	$d_{pp\sigma}(\text{Å})$	0.94860474
$B_{sp\sigma}(\text{Å}^{-1})$	0.46076751	$B_{pp\pi}(\text{Å}^{-1})$	0.03232676
$\alpha_{sp\sigma}(\text{Å}^{-1})$	3.01771075	$\alpha_{pp\pi}(\text{Å}^{-1})$	3.76990646
$d_{sp\sigma}(\text{Å})$	1.22199361	$d_{pp\pi}(\text{Å})$	0.70753711

Table 6. First set of SCED-LCAO Hamiltonian parameters for Nitrogen element.

Since the databases used in the fitting process included only the B_nN_m and C_nN_m clusters, to test the transferability of the optimized nitrogen parameters, we need to perform the robust test for the crystalline structures containing nitrogen atom. The first nitrogen based structure considered in our robust test is a monolayered *h*-BN sheet (Fig. 29). Lattice constant optimization of the structure was performed. Fig. 30 gives the optimization plot as function of the lattice constant. We found that our optimized lattice constant is about 3.5% overestimated compared to the experimental value of 2.5 Å [68]. Calculated electronic densities of states show a wide band gap behavior with the energy gap of 3.303 eV which is underestimated compared to both DFT results (4.04 *eV* and 4.64 *eV* using LDA and GGA, respectively, [69]) and experimental measurements (5.9 *eV* [70, 71] and

5.4 *eV* in [11], respectively). The average charge transfer from Boron to Nitrogen was 0.657 *e*.
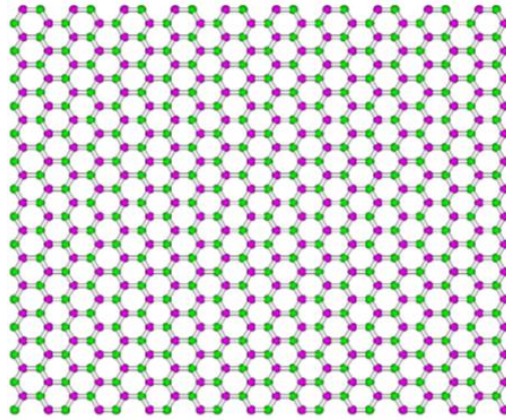
Figure 29. Top view of the optimized 15x10 *h*-BN monolayer using SCED-LCAO parameters for Boron and Nitrogen.
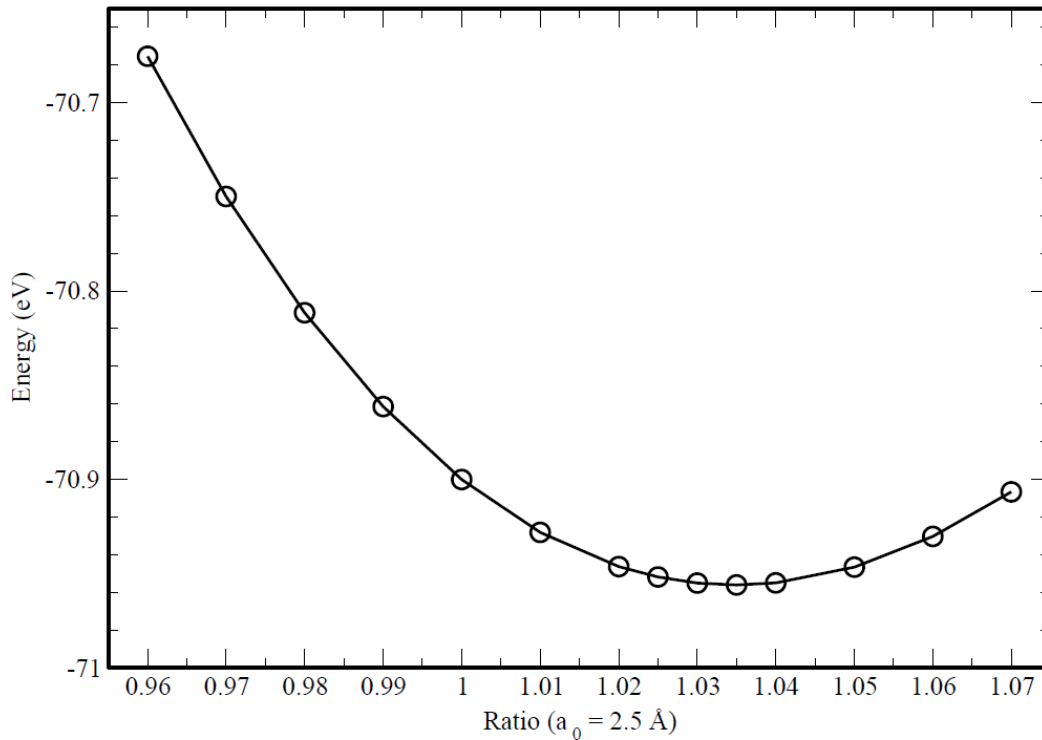
Figure 30. Lattice constant optimization of *h*-BN sheet with optimized lattice at a* = 1.035a_0

The second robust test was done for Wurtzite BN (*w*-BN) bulk structure. A 7x7x4

w-BN bulk was built with the lattice constants $a_0 = 2.55$ Å and $c_0 = \sqrt{\frac{8}{3}} a_0$ [68] (figure

31).
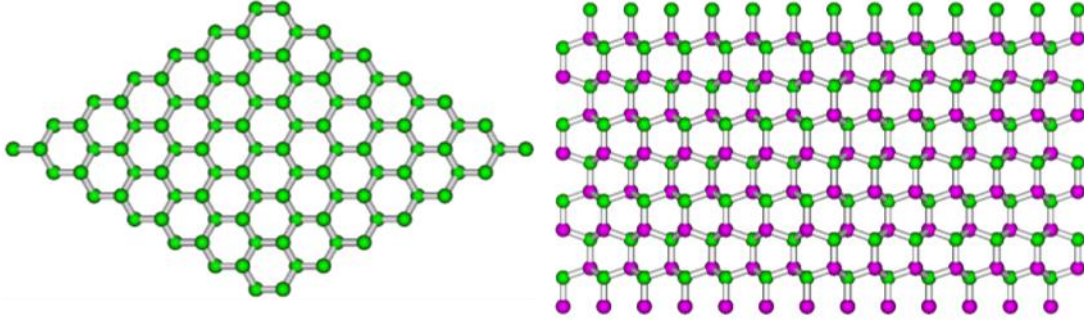
Figure 31. Top view (left panel) and side view (right panel) of the optimized and relaxed
w-BN using SCED-LCAO parameters for Boron and Nitrogen.

The optimized lattice constants were found to be 4% overestimated (see Fig. 32).

The energy gap was also investigated through the calculations of the electronic density of

states and a gap energy of $E_g = 3.7 eV$ was obtained. Similar to the case of *h*-BN sheet, the

calculated gap in the case of *w*-BN was also underestimated compared to the previously

reported values that lie in the range of 4.5 to 5.5 *eV* [68].
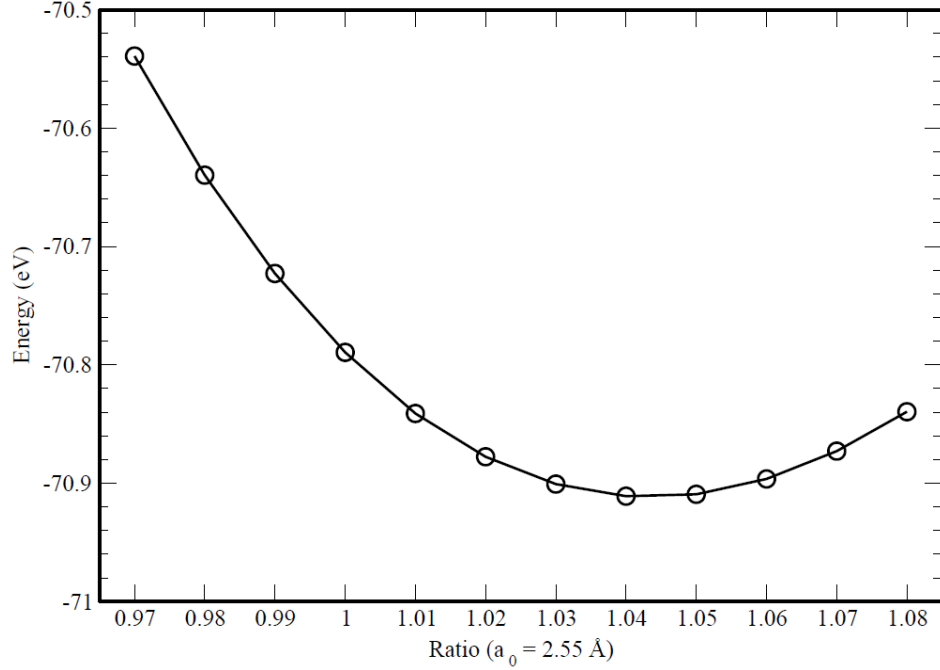
Figure 32. Lattice constant optimization of *w*-BN (7x7x4) bulk with the optimized lattice constants being $a^* = 1.04a_0$ and $c^* = 1.04c_0$, where a_0 and c_0 are defined in the text.

The amount of charges transferred between boron and nitrogen was calculated to be ≈ 0.499 electrons, slightly less charge transfer compared with the amount transferred *h*-BN sheet, indicating nitrogen gains less charge in the *w*-BN bulk than in the *h*-BN sheet.

Since the GaN clusters were not included in the database, it is a big challenge to test the transferability of the optimized SCED-LCAO Hamiltonian for nitrogen in GaN systems. Therefore, we chose Wurtzite GaN crystalline structures as the third structure used in our robust test of the nitrogen parameters. It has been reported that lattice parameters of *w*-GaN are given by [72] ($a_0 = 3.189$ Å and $c_0 = 5.208$ Å) and the energy gap is in the range of 3.23 to 3.457 *eV* at $300K$ [73-77] and 3.30 to 3.50 *eV* at $0K$ [73, 76, 78, 79]. Lattice constant optimization was performed on a 6x6x4 *w*-GaN structure as
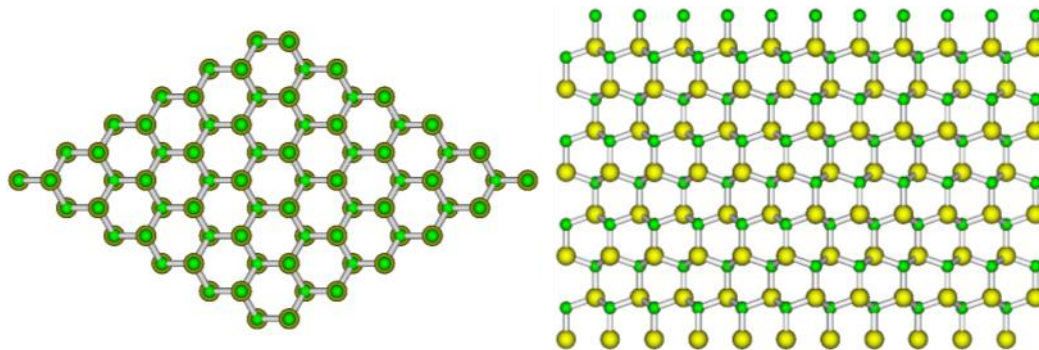
Figure 33. Top view (left panel) and side view (right panel) for the optimized and relaxed *w*-GaN using SCED-LCAO parameters for Gallium and Nitrogen.

shown by its top and side views in figure 33. The optimized lattices were found to be overestimated by 3% as can be seen in the optimization plot (Fig. 34). The optimized structure was then fully relaxed and the electronic density of states were calculated. Interestingly, the calculated energy gap for *w*-GaN bulk was found to be $E_g = 4.962 \ eV$, larger than the reported values, while the amount of charges transferred between the elements Gallium and Nitrogen was around 0.753 electrons.
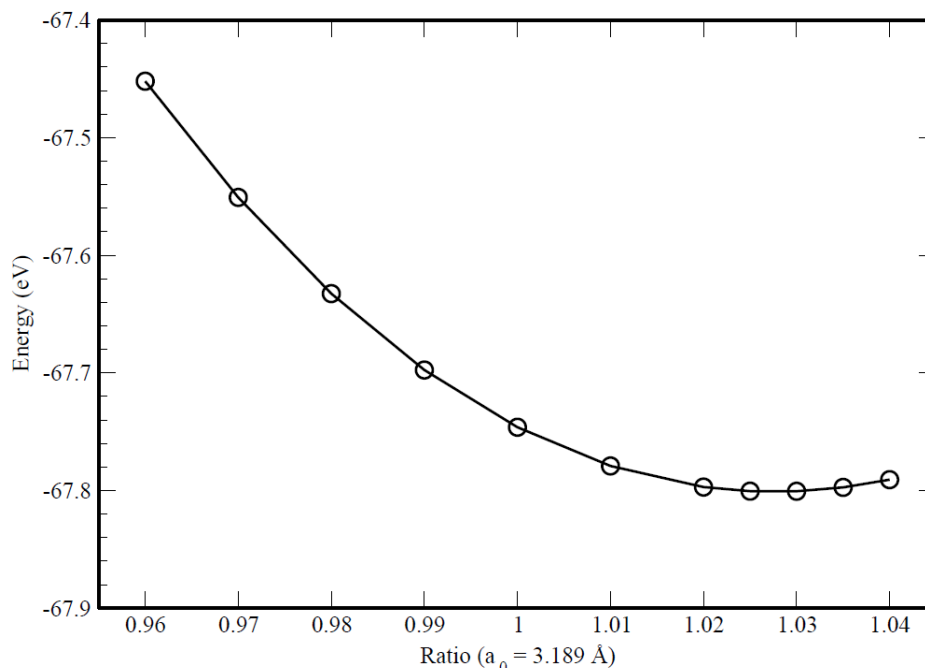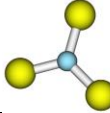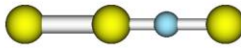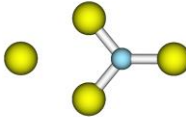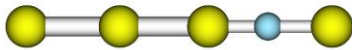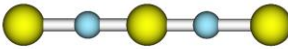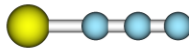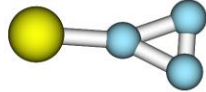
Figure 34. Lattice constant optimization of *w*-GaN (6x6x4) bulk with the optimized lattice constants being $a^* = 1.03a_0$ and $c^* = 1.03c_0$, where a_0 and c_0 are defined in the text.

4.1.2   Nitrogen parameters optimized with Ga_nN_m clusters.

The second strategy used for determining the parameters of SCED-LCAO Hamiltonian for nitrogen consisted of including only the properties of Ga_nN_m clusters in the database. A list of different clusters used in this fitting procedure and their properties are listed in Table 7. This database of properties was computed by Dr. Smith [25].

My work consisted of performing a robust test of the optimized SCED-LCAO nitrogen parameters for different hetero structures containing nitrogen, namely *h*-BN, *w*-BN and *w*-GaN.

Clusters Ga_nN_m	Symmetry	Database References Å, (eV) [25]	SCED-LCAO Results Å, (eV) [25]
	D_{3h}	1.915125 (-0.09120750)	1.91206761 (-0.06997367)
	C_{iha}	2.704187 1.725278 1.845941 (-0.07495350)	2.46234324 1.70791602 1.90968009 (-0.06486886)
	C_{2v}	3.700572 1.209966 1.902282 1.481297 (-0.07983020)	3.39992022 1.27831495 1.91893693 1.43383416 (-0.07004712)
	C_{iha}	2.686556 2.550218 1.719684 1.843453 (-0.06696020)	2.51709146 2.32957791 1.71133512 1.90520958 (-0.05932974)
	D_{iha}	1.740596 1.880500 (-0.08630740)	1.74979945 1.78835803 (-0.07944046)
	C_{ih}	1.912230 1.201475 1.136267 (-0.13104750)	2.01779008 1.22065495 1.16599979 -0.12997784
	C_{2vb}	1.896811 1.397985 0.594313 (-0.10365850)	1.96107874 1.29373921 0.62911387 (-0.09068114)
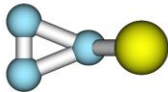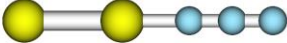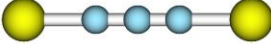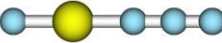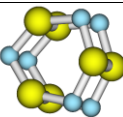
	P_y	1.190017 1.448884 0.589452 1.558995 (-0.10415450)	1.03573571 1.30329321 0.62478750 1.81052627 (-0.09621957)
	C_{iha}	2.744226 1.872233 1.198579 1.136618 (-0.10788460)	2.48401855 1.90510833 1.24739455 1.18046492 (-0.11399023)
	D_{iha}	1.173079 2.020915 (-0.10853960)	1.26334680 1.97744385 (-0.10199629)
	C_{ihb}	1.767594 1.782539 1.197856 1.130722 (-0.10910380)	1.81798028 1.86623543 1.24076908 1.16775707 (-0.13245292)
	D_{3d}	1.748908 2.025861 2.026850 (-0.10289000)	1.83431304 2.07768866 2.12729860 (-0.10981760)

Table 7. Ga_nN_m clusters in different symmetries with geometries and binding energies obtained by ab-initio and SCED-LCAO calculations [25]. Ga (yellow) and N (indigo)

As reported in ref. [25] these different Ga_nN_m clusters were used to determine the optimized nitrogen parameters for SCED-LCAO. Table 8 reports the SCED-LCAO Hamiltonian parameters for nitrogen obtained using this second strategy.

Hamiltonian Parameters for Nitrogen		Hamiltonian Parameters for Nitrogen	
$\varepsilon_s(eV)$	-26.23360	$U(eV)$	15.88403566
$\varepsilon_p(eV)$	-13.84240	$B_Z(\text{Å}^{-1})$	3.84869042
$\varepsilon'_s(eV)$	-34.67487053	$A_N(eV)$	-3.50765478
$\varepsilon'_p(eV)$	-20.28141541	$B_N(\text{Å}^{-1})$	1.78176908
$W_s^0(\text{Å}^{-1})$	0.24230389	$\alpha_N(\text{Å}^{-1})$	3.94697772
$W_p^0(\text{Å}^{-1})$	-0.40115070	$d_N(\text{Å})$	0.57207437
$\alpha_{s,w}(\text{Å}^{-1})$	1.38831534	$\alpha_{NC}(\text{Å}^{-1})$	
$\alpha_{p,w}(\text{Å}^{-1})$	1.45510897	$\alpha_{NB}(\text{Å}^{-1})$	
$\alpha_K(\text{Å}^{-1})$	0.25788710		
Overlap Parameters for Nitrogen		Overlap Parameters for Nitrogen	
$B_{ss\sigma}(\text{Å}^{-1})$	0.67554176	$B_{pp\sigma}(\text{Å}^{-1})$	-1.52123746
$\alpha_{ss\sigma}(\text{Å}^{-1})$	1.72525441	$\alpha_{pp\sigma}(\text{Å}^{-1})$	3.29562875
$d_{ss\sigma}(\text{Å})$	0.24987968	$d_{pp\sigma}(\text{Å})$	0.96429255
$B_{sp\sigma}(\text{Å}^{-1})$	0.47210819	$B_{pp\pi}(\text{Å}^{-1})$	0.03734260
$\alpha_{sp\sigma}(\text{Å}^{-1})$	3.08262899	$\alpha_{pp\pi}(\text{Å}^{-1})$	3.69029550
$d_{sp\sigma}(\text{Å})$	1.27079590	$d_{pp\pi}(\text{Å})$	0.74092947

Table 8. Second set of SCED-LCAO Hamiltonian parameters for Nitrogen element.

We next performed a robust test to check the transferability of these parameters to different cases. The first case considered was the structural optimization of *w*-GaN crystalline structure. The optimized lattice constant using this strategy was 3% underestimated and the energy gap was found to be $E_g = 4.510\ eV$, which is less than what was predicted using strategy #1. The amount of charge transferred between Ga and N elements, however, is 0.776 electrons, larger than that what was obtained using the first set of nitrogen parameters.

Since in this strategy, the database did not contain any properties about BN systems, it is a big challenge to test the transferability of the nitrogen parameters optimized in this case. Similar as we discussed in 4.1.1, we selected *h*-BN sheet and *w*-BN crystalline structures as the testing systems. We found the optimized lattice constant for *h*-BN sheet

to be 1% underestimated and the energy gap was $E_g = 3.396\ eV$ was slightly larger than that obtained from the first set of the nitrogen parameters (discussed in 4.1.1). The calculated charge transfer between boron and nitrogen was also a little bit lower (i.e., $0.609\ e$ in this case and $0.657\ e$ in the first case). In addition, we found from the robust test for w-BN structure that this set of nitrogen parameters underestimated the lattice constants by 4% and could not describe the w-BN system reasonably.

From the robust tests using these two sets of nitrogen parameters, we found that the first strategy overestimated the lattice constants of the crystalline structures, and the second set using only Ga_nN_m clusters in the database underestimated the lattice constants. We also found that these sets of parameters show different trends for energy band gap and charge transfers relative to experiments/DFT. Based on these two observations, we decided to develop a third strategy that expanded the database to include properties of all three clusters. In this third strategy, we considered two cases: (i) Start with optimized parameters as obtained in strategy #1 but add Ga_nN_m clusters and (ii) start with optimized parameters as obtained in strategy #2 but add both B_nN_m and C_nN_m clusters. The aim of using these two directions was to further improve the already tested sets of Nitrogen parameters.

4.2 Tuning the optimized Nitrogen SCED-LCAO parameters with an expanded database.

From these two sets of Nitrogen parameters already optimized, we decided to use a third strategy to tune the parameters. A database expansion was then proposed to include different C_nN_m, Ga_nN_m, and B_nN_m clusters. Table 9 lists the fitting results for these clusters.

Clusters (C_nN_m)	Symmetry	Database References Å, (eV) [25]	SCED-LCAO Results Å, (eV)
C_2N	C_{2v}	0.790381 1.032042 (-0.152305)	0.790381 1.032042 (-0.15518146)
C_2N_2	D_{ih}	1.375569 1.152190 (-0.200156)	1.22301805 1.27846555 (-0.18489171)
C_2N_2	D_{2h}	0.737351 1.147029 (-0.158600)	0.82984288 1.13598749 (-0.15046782)
C_3N_2	D_{ih}	1.309768 1.182964 (-0.195146)	1.21979439 1.29798459 (-0.21134173)
CN_3	C_{3v}	0.885050 1.078976 (-0.113750)	0.79515542 1.13669891 (-0.13064064)
C_3N_2	D_{3h}	1.020275 1.054562 (-0.145869)	0.95657128 1.16115683 (-0.16719341)

Table 9.1. C_nN_m clusters in different symmetries with geometries and binding energies obtained by ab-initio [25] and SCED-LCAO calculations after database expansion.

Clusters Ga_nN_m	Symmetry	Database References Å, (eV) [25]	SCED-LCAO Results Å, (eV)
Ga_3N	D_{3h}	1.915125 (-0.09120750)	1.87361838 (-0.08663734)
Ga_3N	C_{iha}	2.704187 1.725278 1.845941 (-0.07495350)	2.47736182 1.67076202 1.84528489 (-0.07482634)
Ga_4N	C_{2v}	3.700572 1.209966 1.902282 1.481297 (-0.07983020)	3.38277633 1.22367837 1.86912944 1.42566837 (-0.08208574)
Ga_4N	C_{iha}	2.686556 2.550218 1.719684 1.843453 (-0.06696020)	2.51905362 2.36993188 1.67331049 1.84135884 (-0.06706916)
Ga_3N_2	D_{iha}	1.740596 1.880500 (-0.08630740)	1.73058740 1.74189151 (-0.09351220)
GaN_3	C_{ih}	1.912230 1.201475 1.136267 (-0.13104750)	1.91742180 1.16673874 1.10542101 (-0.12854615)

Clusters (GanNm)	Symmetry	Database References Å, (eV) [25]	SCED-LCAO Results Å, (eV)
GaN₃	C₂ᵥᵦ	1.896811 1.397985 0.594313 (-0.10365850)	1.90284817 1.22141580 0.60404396 (-0.10011877)
GaN₃	Pᵧ	1.190017 1.448884 0.589452 1.558995 (-0.10415450)	1.10468489 1.23258292 0.59954052 1.67547238 (-0.10533089)
Ga₂N₃	Cᵢₕₐ	2.744226 1.872233 1.198579 1.136618 (-0.10788460)	2.50320345 1.82805717 1.20346261 1.12636389 (-0.11300815)
Ga₂N₃	Dᵢₕₐ	1.173079 2.020915 (-0.10853960)	0.11300815 1.89199829 (-0.10316715)
GaN₄	Cᵢₕᵦ	1.767594 1.782539 1.197856 1.130722 (-0.10910380)	1.79380063 1.83982536 1.18487897 1.10857809 (-0.13563672)
Ga₆N₆	D₃ᵈ	1.748908 2.025861 2.026850 (-0.10289000)	1.80544341 2.04050491 1.89766259 (-0.11403329)

Table 9.2. GaₙNₘ clusters in different symmetries with geometries and binding energies obtained by ab-initio [25] and SCED-LCAO calculations after database expansion.

Clusters (BₙNₘ)	Symmetry	Database References Å, (eV) [25]	SCED-LCAO Results Å, (eV)
BN	Dᵢₕ	0.659675 (-0.088449)	0.58475764 (-0.09790214)
BN₂	Dᵢₕ	1.323160 (-0.116296)	1.37397991 (-0.12384299)
BN₂	Cᵢᵥ	1.143163 1.456700 (-0.126543)	1.13742886 1.41503257 (-0.12216280)
BN₂	C₂ᵥ	0.648227 1.255078 (-0.126553)	0.62677059 1.25237169 (-0.12051271)
BN₃	C₂ᵥₐ	0.583497 1.272920 1.456654 (-0.142195)	0.57901677 1.30747910 1.46218033 (-0.13866398)
BN₃	C₂ᵥᵦ	1.156522 0.858636 0.671727 (-0.130590)	1.15301698 0.85569203 0.61335796 (-0.12817254)

BN$_3$	C$_{iva}$	1.369382 1.203877 1.122779 (-0.141462)	1.38188884 1.20209633 1.10809587 (-0.14536553)
BN$_3$	C$_{ivb}$	1.259239 1.395666 1.112110 (-0.154901)	1.27747138 1.43482542 1.10474971 (-0.15712812)
B$_2$N	D$_{ih}$	1.311856 (-0.141881)	-0.13866398 (-0.14695152)
B$_2$N$_2$	C$_{2v}$	0.615391 1.537884 1.341462 (-0.128828)	0.61740598 1.537884 1.28127546 (-0.12621733)
B$_2$N$_2$	D$_{2h}$	1.181049 0.798394 (-0.149559)	1.13862604 0.83127362 (-0.14931366)
B$_3$N	C$_{2v}$	1.077058 1.418147 0.864972 (-0.138497)	1.08464721 1.35134485 0.86671371 (-0.13448410)
B$_3$N	C$_{iva}$	1.30029500 1.57007800 1.54653100 (-0.11985725)	1.28027033 1.58258061 1.71816743 (-0.11787019)
B$_3$N	C$_{ivb}$	1.37794200 1.26515400 1.78043900 (-0.13633825)	1.35681047 1.24029226 1.75971302 (-0.13698039)

Table 9.3. B$_n$N$_m$ clusters in different symmetries with geometries and binding energies obtained by ab-initio [25] and SCED-LCAO calculations after database expansion.

It was found that with an extension of the database, all the structural properties and cohesive energies fitted better with the DFT calculations. Table 10 summarizes the new set of optimized parameters obtained by adding B$_n$N$_m$ and C$_n$N$_m$ clusters to the already optimized parameters of strategy #2.

Hamiltonian Parameters for Nitrogen		Hamiltonian Parameters for Nitrogen	
$\varepsilon_s(eV)$	-26.23360	$U(eV)$	16.35696834
$\varepsilon_p(eV)$	-13.84240	$B_Z(\text{Å}^{-1})$	4.28111905
$\varepsilon'_s(eV)$	-36.52887172	$A_N(eV)$	-2.75813588
$\varepsilon'_p(eV)$	-24.66565288	$B_N(\text{Å}^{-1})$	1.47863869
$W_s^0(\text{Å}^{-1})$	0.77960808	$\alpha_N(\text{Å}^{-1})$	3.91763769
$W_p^0(\text{Å}^{-1})$	-0.47307269	$d_N(\text{Å})$	0.61063727
$\alpha_{s,w}(\text{Å}^{-1})$	0.95204876	$\alpha_{NC}(\text{Å}^{-1})$	0.41618895
$\alpha_{p,w}(\text{Å}^{-1})$	1.47150765	$\alpha_{NB}(\text{Å}^{-1})$	0.51857326
$\alpha_K(\text{Å}^{-1})$	0.13359119		
Overlap Parameters for Nitrogen		Overlap Parameters for Nitrogen	
$B_{ss\sigma}(\text{Å}^{-1})$	0.57409702	$B_{pp\sigma}(\text{Å}^{-1})$	-1.51531003
$\alpha_{ss\sigma}(\text{Å}^{-1})$	0.04130860	$\alpha_{pp\sigma}(\text{Å}^{-1})$	3.23504242
$d_{ss\sigma}(\text{Å})$	0.33019252	$d_{pp\sigma}(\text{Å})$	1.07988300
$B_{sp\sigma}(\text{Å}^{-1})$	0.46233834	$B_{pp\pi}(\text{Å}^{-1})$	0.04130860
$\alpha_{sp\sigma}(\text{Å}^{-1})$	3.43835960	$\alpha_{pp\pi}(\text{Å}^{-1})$	3.37257746
$d_{sp\sigma}(\text{Å})$	1.44240327	$d_{pp\pi}(\text{Å})$	0.62455627

Table 10. Tuned SCED-LCAO Hamiltonian parameters for Nitrogen through database expansion.

Using these tuned nitrogen parameters, we conducted robust tests and found that for all three crystalline structures under consideration, the optimized lattice constants are in better agreement with the experimental results [68, 72]. For both *h*-BN sheet and *w*-GaN bulk, a small overestimation of 2% was found for the lattice constant, while for *w*-BN bulk the lattice constant was only overestimated by about 1%. Furthermore, the energy gaps corresponding to these cases are found as follows: (i) 5.26 *eV* for *w*-BN bulk that is consistent with the reported experimental values in Ref. 63 (see Table 11); (ii) 3.360 *eV* for *h*-BN sheet (underestimated) and (iii) 6.556 *eV* for *w*-GaN bulk (overestimated).

A summary of the three different sets of nitrogen parameters discussed above is given in table 11 with the structures used for the robust test, the optimized lattice constants, energy gap and the charge transfer to nitrogen from either boron or gallium. The three

different Hamiltonian parameters (ε_s', ε_p' and U) that were the most important parameters

controlling the chemical potential (and therefore, the charge transfers) and electron-

electron correlation (and therefore, the band gap) are also included in table 11 to show their

different evolutions with respect to the methods used.

Nitrogen parameters	First set			Second set		
Structures (super cell)	*h*-BN (15x10)	*w*-BN (7x7x4)	*w*-GaN (6x6x4)	*h*-BN (15x10)	*w*-BN (7x7x4)	*w*-GaN (6x6x4)
a* (Å)	1.035 x a_0	1.04 x a_0	1.03 x a_0	0.99 x a_0	No optimized lattice constant, smaller than radius	0.97 x a_0
c* (Å)	-	1.04 x c_0	1.03 x c_0	-		0.97 x c_0
E_{gap}(eV)	3.303	3.701	4.962	3.396		4.5096
Charge transfer N gains (e)	0.6568	0.4993 to 0.4994	0.7531 to 0.7532	0.60867		0.776
ε_s'	-29.80655145			-34.67487053		
ε_p'	-21.139342100			-20.28141541		
U	14.37890796			15.88403566		

Nitrogen parameters	Third set		
Structures	*h*-BN (15x10)	*w*-BN (7x7x4)	*w*-GaN (6x6x4)
a* (Å)	1.02 x a_0	1.01 x a_0	1.02 x a_0
c* (Å)	-	1.01 x a_0	1.02 x c_0
E_{gap}(eV)	3.360	5.26	6.556
Charge transfer N gains (e)	0.46547	0.306	0.547
ε_s'	-36.52887172		
ε_p'	-24.66565288		
U	16.35696834		

Table 11. Summary of robust test for Nitrogen SCED-LCAO Hamiltonian parameters obtained with first (top table left), second (top table right), third (bottom table) sets of optimization.

CHAPTER V

APPLICATIONS OF NITROGEN SCED-LCAO PARAMETERS FOR BAND GAP

ENGINEERING

5.0 Background.

With the advances made in synthesizing two-dimensional materials such as graphene and monolayer *h*-BN, there is unprecedented enthusiasm in the research on two-dimensional materials as they open the door to many technological innovations and provide a perfect playground to test the existing theories and models for two-dimensional systems. The properties of materials in reduced dimensions are different from their bulk counterparts because of effects arising from the quantum confinement of electrons and size-effects that profoundly alter the electronic, transport, optical, and other properties of 2D materials. Specifically, a fundamental research on 2D ternary systems is exciting because, by varying the percent composition of an element in a hybrid structure, one could tune the energy gap. Such materials design studies are necessary for the progress in photovoltaics research.

Graphene is known to have a unique band structure with a zero band gap at the Dirac point and a linear energy dispersion near its Fermi level [5], while *h*-BN is a wide band gap material with an energy gap of 5.9 *eV* [70, 71]. With synthesis of these materials via exfoliation or CVD becoming a routine, it is natural to ponder over the question: "whether it is possible to synthesize an atomic sheet composed of ternary elements B, N, and C? "If so, will it form an alloy sheet or will it phase separate into BN domains and

graphene domains? Recently, the Rice university group synthesized 2D hybrid structures of boron nitride and graphene domains using methane and ammonia-borane as precursors for BN and C in a thermal catalytic CVD method [11]. The experimental set-up allowed the carbon content in the hybrid structure to be controlled and thus allowing a study of the energy gap dependence as a function of the atomic percent composition of carbon (0%, 35%, 65%, 85%, etc.) in the hybrid structure. A variety of characterization tools ((AFM, HRTEM, Raman, XPS, EELS, and UV-visible absorption spectroscopy, *etc.*) was used to determine the atomic structure and bonding of hybrid ternary BNC films. Based on the results of these characterizations, the authors argue that the observed structure was neither an alloy nor a stacked structure of *h*-BN and graphene but a hybrid 2D structure composed of graphene and BN domains. Specifically, the absorption spectroscopy experiment conducted on the synthesized samples reveal a second absorption peak corresponding to carbon domains in the BNC sheet and, furthermore, the position of this peak shifted to higher wavelengths as the carbon content in the hybrid structure increased. More specifically, the optical gap shifted from 1.62 eV to 1.51 eV, as the carbon content in the hybrid BNC sheet increased from an atomic percentage of 65% to 85%. This experiment demonstrates that by controlling the domain size of graphene domains, one can tune the energy gap in a hybrid BNC sheet composed of BN and graphene domains.
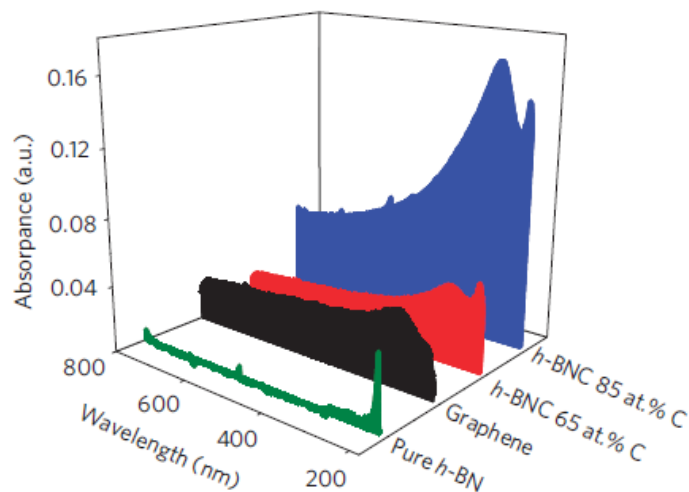
Figure 35. The absorption spectra in the ultraviolet-visible regions for different types of graphene-like films as reported in Ref. [11].

On the theoretical front, the literature reports a study that calculates the formation energies and energy gaps of circular shaped carbon quantum dots (QD) of different diameters embedded into h-BN sheets using the DFT method as implemented in the SIESTA code [80]. This study finds the formation energy to oscillate as a function of the size of the carbon quantum dots and concludes that the hybrid system has lower energy whenever the quantum dot contains complete aromatic rings. The density of states for the hybrid (QD + h-BN) system seems to indicate the existence of a strong hybridization among 2p orbitals of B, N and C. Fig. 36 shows the energy gap dependence as a function of the diameter of graphene QD, as obtained in ref. [80].
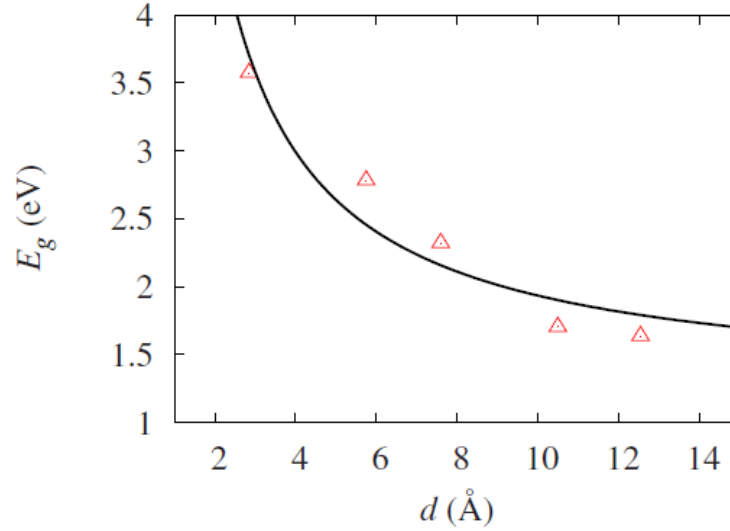
Figure 36. Energy gap E_g as a function of the diameter d of the graphene quantum dot as reported in Ref. [80].

It is worth noting that the theoretical study presented in ref. [80] is restricted to circular graphene quantum dots in h-BN sheets and the highest atomic percentage considered is less than 11%, while the BNC films investigated by the Rice group contain graphene domains and BN domains of random size and arbitrary shapes.

Motivated by the above two studies, I have performed a systematic study of different shaped (triangular, rectangular, circular, hexagonal) and sized graphene domains (up to an atomic percentage of 40%) in h-BN sheets to understand the energy gap-dependence of the ternary BNC sheet as a function of the size and shape of graphene domains. The following section will discuss the results obtained from such a study. In section 5.2, we have studied the stability of patterned graphene sheets containing holes of different shapes (circular, rectangular, hexagonal) and sizes. The goal of designing such patterned graphene sheets is to understand whether they will serve to open up the energy gap of graphene. A study of such patterned graphene with holes may hold promise as materials for supercapacitors [11-12, 82] and energy storage applications [13].

5.1 Band gap engineering by constructing *h*-BN sheet with various graphene domains.

Figure 37 depicts the four different types of graphene domains embedded in an *h*-BN sheet. In addition, the size of the graphene domains will be changed to understand the roles played by both size and shape of graphene domains in altering the band gap of pristine *h*-BN sheet. As a first step, we optimize the structure of a pristine *h*-BN sheet and determine the energy band gap as obtained by the SCED-LCAO method. The Hamiltonian parameters for nitrogen as obtained in chapter IV are used in constructing the SCED-LCAO Hamiltonian for the *h*-BN system. A supercell of size 15x10 containing 600 atoms and a vacuum of 1000 Å is used in our SCED-LCAO calculations. Simulations of pristine *h*-BN sheets were followed by simulations of 2D hybrid BNC system, containing graphene domains of different shapes (triangular, hexagonal, circular, and rectangular) and sizes embedded into the *h*-BN sheet. In the case of triangular graphene domains embedded into *h*-BN sheets, we distinguish two cases based on how the etching is performed. In the first case, the etching of *h*-BN sheets is such that we replaced all boron atoms falling along the perimeter of the triangular etch by carbon atoms (T-B type graphene domains) and in the second case, we replaced all nitrogen atoms falling along the perimeter of triangular etch by carbon atoms (T-N type graphene domains). In the former case, the interface between the graphene domain and the *h*-BN sheet will have C-N bonds while in the second case, the interface between the graphene domain and the *h*-BN sheet will have C-B bonds. It will be interesting to investigate how this difference in the bonding characteristics of the interface will influence the electronic density of states and the energy gaps.

88
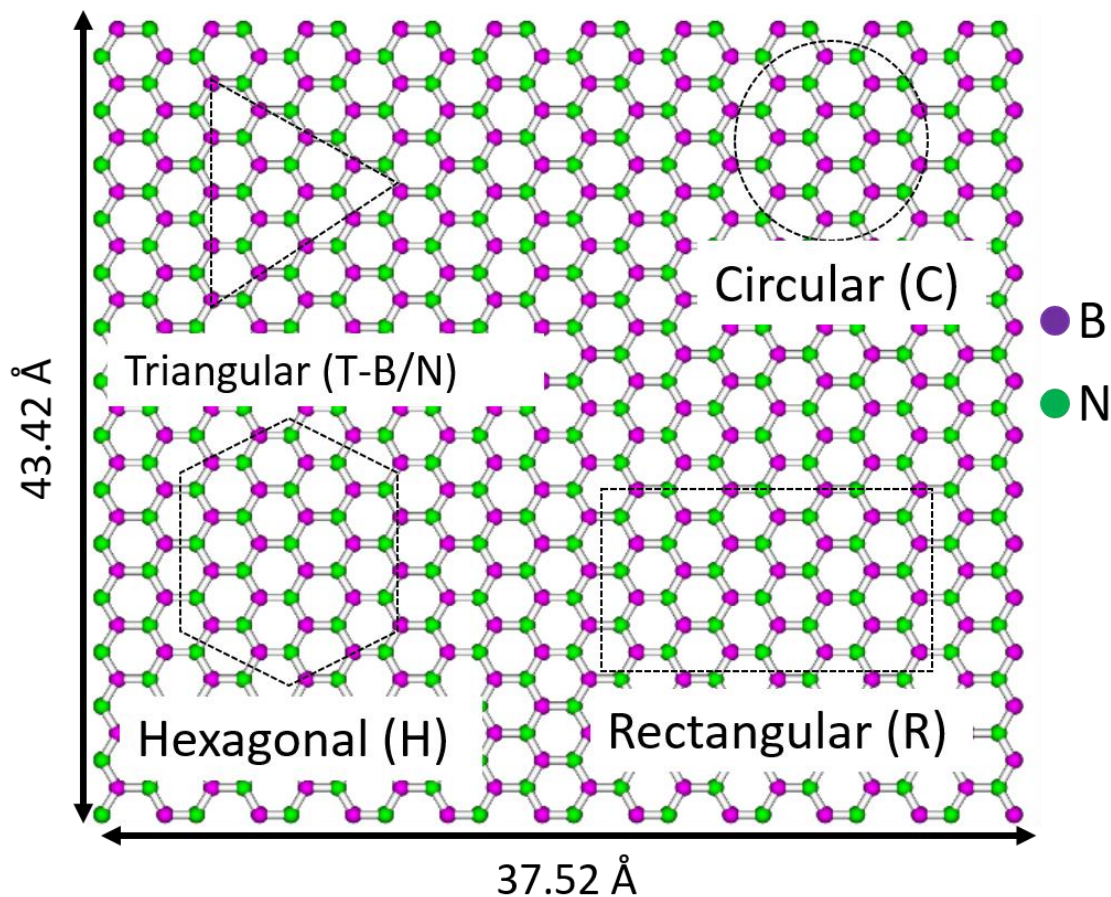
<u>Figure 37.</u> A schematic of a 15x10 *h*-BN sheet and the four types of graphene domains (triangular, circular, hexagonal and rectangular) to be created.

Prior to doing detailed simulations of graphene domains of different sizes in *h*-BN sheet, we had to decide on which parameter set to choose for the SCED-LCAO Hamiltonian for nitrogen. Therefore, we calculated the band gap of pristine *h*-BN sheet using both sets. We found that option #1 yielded a band gap of 3.303 eV and option #2 yielded an energy gap of 3.396 eV. We also found that the calculated electronic properties of *h*-BNC sheets were similar for both parameter sets of nitrogen. Therefore, in the rest of this work, we will use the first set of nitrogen parameters reported in Table10. The reliability of our SCED-LCAO calculations for *h*-BN sheets and hybrid *h*-BN/C sheet was also confirmed using DFT calculations performed using the VASP package [9] for selected

cases. In DFT calculations, we used a smaller supercell of size 10x5 since the total number of atoms handled by first-principles is limited. This imposed further restrictions on sizes and shapes of graphene domains in the first-principle simulations of hybrid h-BN/C system. Using DFT simulations, we were able to perform simulations only on the two smallest triangular and rectangular domains, and three circular graphene domains.

5.1.1 Triangular shaped graphene domains in hybrid h-BN/C sheets.

5.1.1.a Case 1: Graphene domains with C-N interface (T-B).

Triangular shaped graphene domains are embedded in the 15x10 h-BN sheets. A total of 4 different sizes for the triangular domains were considered with an increase number of Carbon atoms as the sizes increase. Triangular 1 (T-B_1) has a total of 3 Boron atoms replaced by Carbon and it is the smallest in size with the 3 atoms forming the triangular shape. The next size is triangular 2 (T-B_2), a total of 12 Boron is replaced along the boundaries of the triangle to form the 3 different sides with 5 atoms per side. The total number of carbon atoms is 21. Triangular 3 (T-B_3) accounts for 21 Boron replaced along the perimeter of the domain with the total 57 carbon atoms in the domain, and triangular 4 (T-B_4) has a total of 30 Carbon atoms replacing 30 Boron atoms along the perimeter with the total 111 carbon atoms in the domain. These four samples are fully optimized and relaxed using the SCED-LCAO method and only two of them (i.e., T-B_1 and T-B_2) are found stable. They were shown in the insets of Fig. 38 (a).

As already found in chapter IV, h-BN has a wide band gap with the Fermi level clearly shown between the top of the valence band (VB) and the bottom of the conduction band (CB) (see the black curve and black dashed line in Fig. 38 (a) and (b)). Embedding a

triangular graphene domain on the *h*-BN sheet changes the physiognomy of the density of states. For instance, in the cases of triangular Boron 1 and 2 (T-B_1 and T-B_2), even though the shapes and the positions of the VB and CB almost unchanged, there are a few 'impurity' states appearing within the gap of the pristine *h*-BN sheet and the larger the size of the graphene domain, the more the states, and therefore the narrower the band gap (see the dashed red and green curves in Fig. 38 (a)).
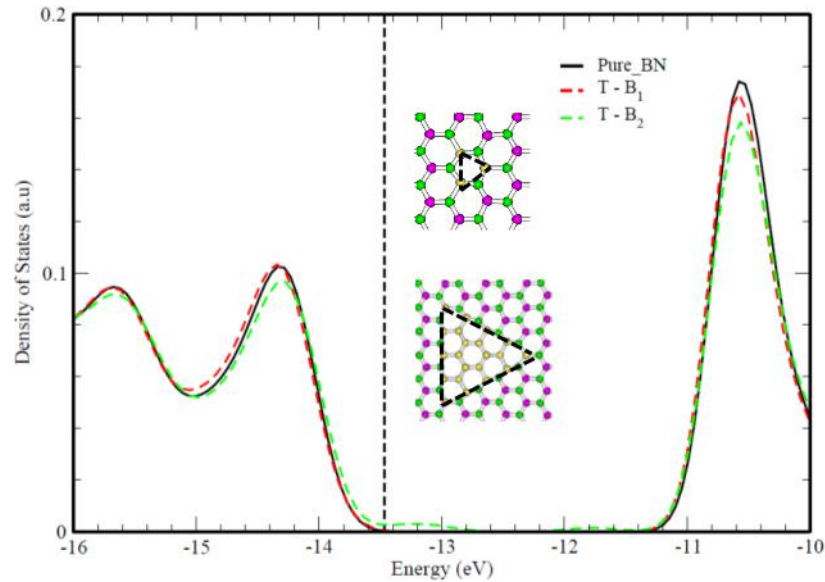
Figure 38. (a) The density of states of patterned *h*-BN sheets containing triangular graphene domains of two different sizes as calculated using the SCED-LCAO method. To design such patterned *h*-BN sheets (labeled T-B), we replaced both boron and nitrogen atoms within a triangular region by carbon atoms and the boron atoms along the perimeter by carbon atoms. The black dashed line denotes the Fermi level of the *h*-BN sheet. The insets shown in this figure correspond to relaxed structures of *h*-BN/C hybrid sheets containing 3- and 21- carbons domains (labeled T-B_1 and T-B_2, respectively).

With the appearances of some states between VB and CB of the DOS calculations, we were interested in finding the origin of such states hence it was proposed to calculate the local density of states (LDOS) located at the carbon domain. Fig. 38 (b) shows the LDOS (blue curve) for the biggest triangular domain (T-B_2) together with the total DOS for pristine *h*-BN (black curve) and T-B_2 (red curve) respectively. By comparing the total

DOS (red) with the LDOS (blue), we found that the states appearing between the VB and

CB are indeed contributions from the graphene domain.

Figure 38. (b) The local density of states located at the carbon domain for T-B$_2$ (blue) together with the total DOS for pristine h-BN (black) and T-B$_2$ (red) respectively. The dotted black line shows the Fermi level of pristine h-BN.

5.1.1.b Case 2: Triangular Nitrogen.

Similar as in triangular Boron, triangular Nitrogen also has four different sizes of triangular graphene domains. Triangular Nitrogen1 (T-N$_1$) were constructed with 3 nitrogen atoms replaced by 3 carbon atoms along the perimeter of the triangle which also is the smallest possible triangular domain; triangular nitrogen 2 (T-N$_2$) with 12 nitrogen atoms being replaced by carbon; triangular nitrogen 3 (T-N$_3$) in which 21 carbon atoms replaced 21 nitrogen atoms along the perimeter and finally triangular nitrogen 4 (T-N$_4$) where a total of 30 nitrogen atoms are replaced by carbon. These samples were optimized and fully relaxed using the SCED-LCAO, and the relaxed h-BN sheet with different size of triangular nitrogen graphene domains were shown in

the insets of Fig. 39 (a). The electronic density of states calculations for triangular Nitrogen show that the replacement of boron and nitrogen atoms by carbon atoms through embedding leads to the appearing of states both at the top of the valence band and the bottom of the conduction band (see Fig. 39 (a)) hence a decrease in the energy difference between the two bands. With increasing the size of the graphene domain, the shapes of VB and CB change, e.g., their peaks were broaden and their tails were extended towards the gap, leading to narrowing the band gap.
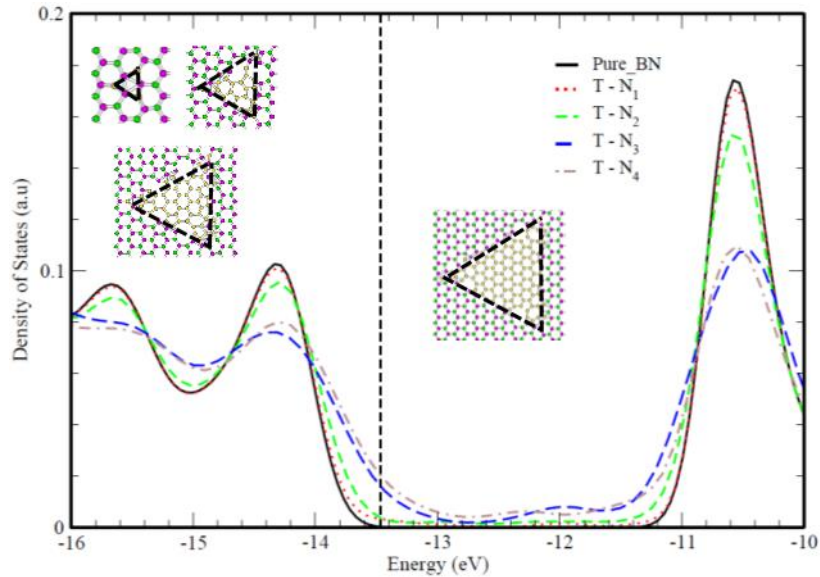
Figure 39. (a) The densities of states results corresponding to the second type of triangular graphene domains (T-N) embedded into h-BN sheets, where the interface now contains C-B bonds with all nitrogen atoms along the perimeter of the triangle replaced by carbon atoms and the interior B and N atoms replaced by carbon atoms. Insets show the relaxed structures corresponding to four different sizes of graphene domains embedded in *h*-BN sheets. The black dashed line denotes the Fermi level of the *h*-BN sheet.

The calculation of the LDOS located at the carbon domain for T-N_4 as an example is shown in Fig. 39 (b) and it reveals that the states appearing between the VB and CB are partially due to the presence of the carbon domain and partially due to the boron and nitrogen atoms at the boundary. The states are more pronounced as the size of the domain increases.
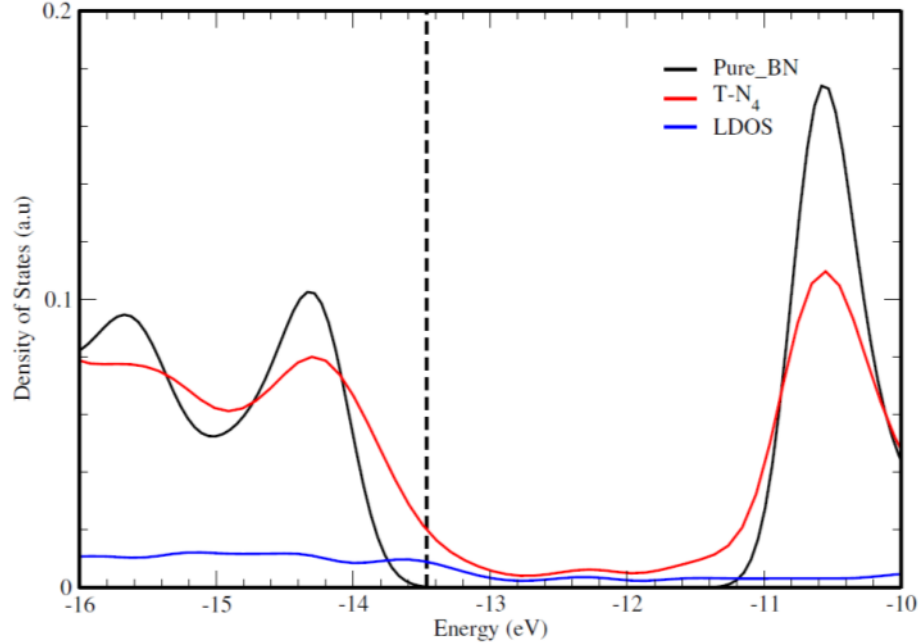
<u>Figure 39.</u> (b) The local density of states located at the carbon domain for T-N$_4$ (blue) together with the total DOS for pristine *h*-BN (black) and T-N$_4$ (red) respectively. The dotted black line shows the Fermi level of pristine *h*-BN.

5.1.2 Circular Shapes of graphene domains.

Circular graphene domains are constructed by creating the graphene domain with circular shapes embedded in our *h*-BN sheet. The possible smallest domain is circular1 (C-1) which is a complete hexagon of 3 boron and 3 nitrogen atoms which are all replaced by carbon hence a total of 6 carbon atoms. A total of 6 different sizes of circular shape (i.e., C-1, C-2, C-3, C-4, C-5, and C-6) were found to be possible to be embedded on our 15x10 BN sheet. The largest circle has a diameter of 23.97 Å. It was found that, during the relaxation, the graphene domain kept intact towards the center of the circle, while at the boundaries the strong interactions between the 3 different atoms lead to break of the hexagonal symmetries locally more noticeable in the smaller circular domains. The relaxed *h*-BN sheet with various circular graphene domains were shown in the insets of Fig. 40 (a). The electronic density of states shown

in Fig. 40 (a), predict the appearance of new states both at the top of the VB and also bottom of the CB similar to the cases found in the triangular domains. Through local density of states calculations (e.g., the blue curve of Fig. 40 (b) shows the LDOS for graphene domain C-6), the states were identified to be mainly contribution from the graphene domain which is also observable from the total DOS since as the diameter of the circles increase the states also appear more clearly together with a shift of the Fermi level towards to the conduction band in the h-BN sheet; suggesting a decrease in the energy gap.
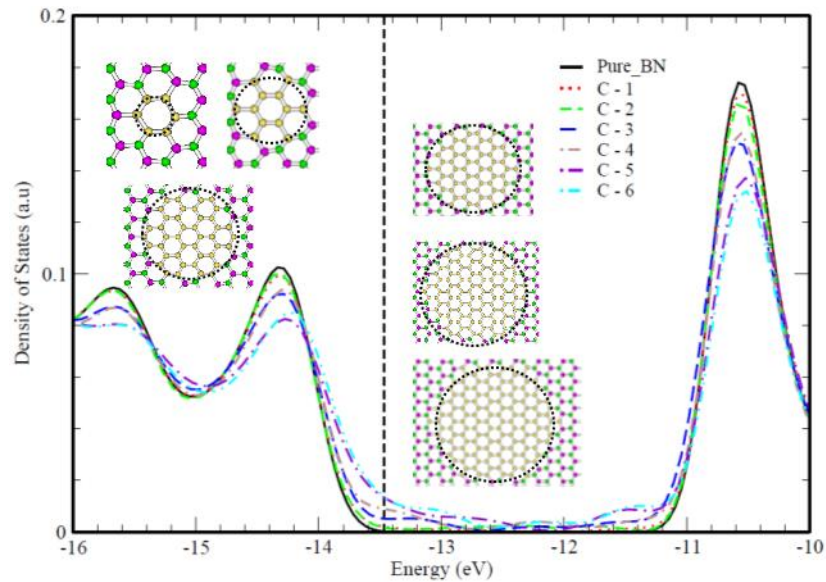
Figure 40. (a) The densities of states results for h-BN/C hybrid sheets corresponding to circular graphene domains of different sizes using the SCED-LCAO method. The Fermi level is denoted by the black dashed line. The insets show the relaxed structures of h-BN/C hybrid sheets corresponding to six different circular graphene domains of different sizes.
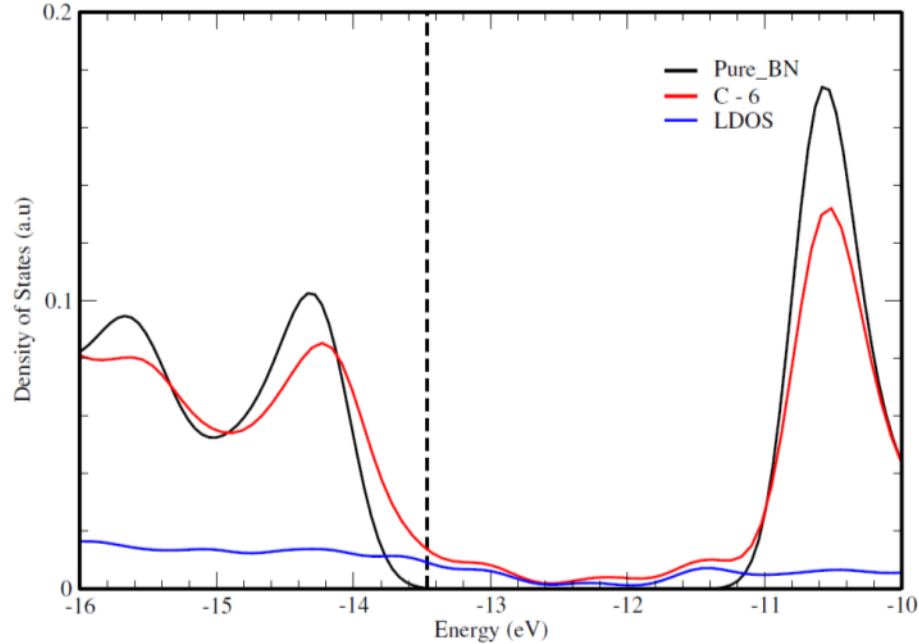
Figure 40. (b) The local density of states located at the carbon domain for C-6 (blue) together with the total DOS for pristine *h*-BN (black) and C-6 (red) respectively. The dotted black line shows the Fermi level of pristine *h*-BN.

5.1.3 Hexagonal Shapes of graphene domains.

Four hexagonal domains were considered which were constructed by the number of hexagons and are named as H-1, H-2, H-3, and H-4, respectively. The smallest hexagonal domain H-1 was formed by three nearest hexagons with thirteen carbon atoms. The second one, H-2 was constructed by seven nearest hexagons with six of them around the central one. When adding another twelve hexagons surrounded to the H-2, we formed H-3. The biggest hexagonal Carbon domain, H-4, was constructed by adding 18 hexagons at the boundary of H-3, with possible distance between two edges of the hexagon being 17.99 Å. We found that, at the center of a given domain the graphene structure is well-defined. But as one moves from the center towards the hexagonal boundaries, the interaction between the carbon atoms and boron or nitrogen atoms becomes stronger with different bonds between two types of carbon. The two types of carbon atoms identified at

the boundaries are C_1 and C_2. In C_1 the carbon is connected to two carbon atoms and a single nitrogen atom while in C_2 the carbon atom is connected to two carbon atoms and a single boron atom. These two types of carbon atoms are alternately distributed along the 6 edges of the hexagon domain. The relaxed *h*-BN sheet with different size of hexagonal graphene domains were shown in the insets of Fig. 41 (a). As in the previous discussions, the electronic density of states revealed the appearance of some hybrid states at the top of VB and the bottom of CB, leading to a decrease in their energy difference but the shape of the valence/conduction band almost remains the same as the pure *h*-BN.
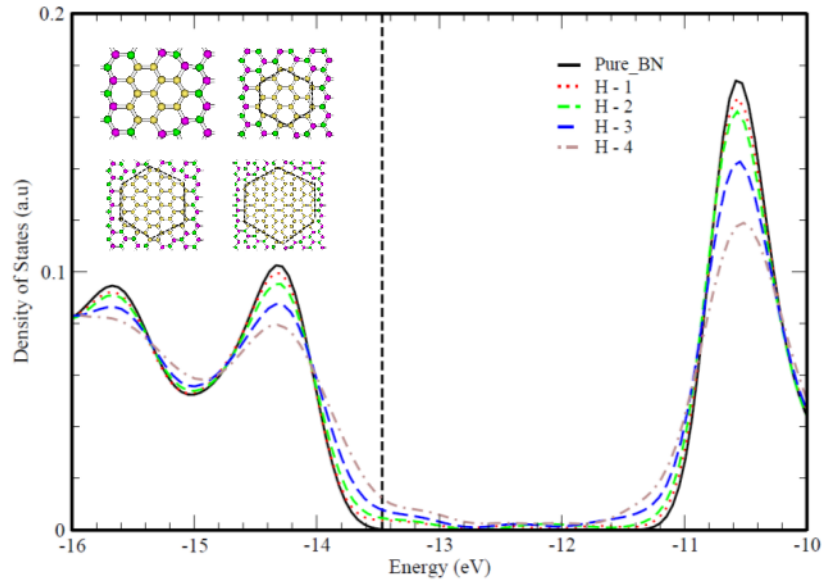
Figure 41. (a) The densities of states results for *h*-BN/C hybrid sheets corresponding to hexagonal graphene domains of different sizes as obtained using the SCED-LCAO method. The Fermi level of the *h*-BN sheet is denoted by the black dashed line. The insets show the relaxed *h*-BN/C hybrid sheet corresponding to hexagonal graphene domains of different sizes.

The calculation of the LDOS for the hexagonal graphene domain also revealed that the states are originating from the carbon domains of the different hexagonal shapes. Fig. 41 (b) as an example, shows the total DOS of both pristine BN (black curve) H-4 *h*-BNC (red curve) respectively, with the LDOS for H-4 domain (blue curve).
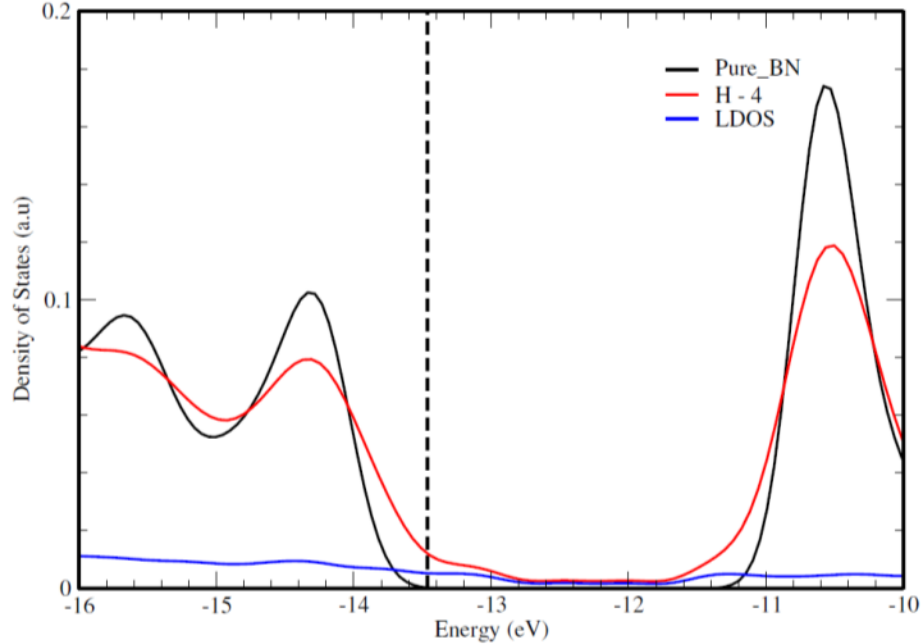
<u>Figure 41.</u> (b) The local density of states located at the carbon domain for H-4 (blue) together with the total DOS for pristine *h*-BN (black) and H-4 (red) respectively. The dotted black line shows the Fermi level of pristine *h*-BN.

5.1.4 Rectangular Shapes of graphene domains.

Rectangular shapes of graphene domains are constructed and embedded in the *h*-BN sheet to create the *h*-BNC sheets and subsequently check the effect on the gap energy. A total of 7 rectangular shaped graphene domains were created, named as R-1, R-2, R-3 R-4, R-5, R-6, and R-7. Note that CB and CN bonds are located at opposite sides of the rectangular and alternatively distributed at the other two sides. The smallest rectangular graphene domain is rectangular 1 (R-1), in which a total of 6 carbon atoms substitute 3 boron and 3 nitrogen atoms and form the perimeter. The largest possible rectangular carbon domain for which there is no interaction between the neighboring domains is rectangular 7 (R-7), where a total of 42 carbon atoms substitute 21 boron and 21 nitrogen atoms along the edges of the perimeter with lengths of 29.97 Å and 21.00 Å, respectively. At the boundaries the interactions between the carbon atoms and boron or nitrogen atoms are

strong but the symmetries are kept. The relaxed *h*-BN sheet with various rectangular graphene domains were shown in the insets of Fig. 42 (a). The electronic density of states calculations also revealed that the introduction of rectangular graphene domains within the *h*-BN sheet favored the appearance of some hybrid states at the top of the VB and the bottom of CB. As the area of the rectangular domains increases a decrease in the energy difference between the two bands was found when compared to the energy gap of pure *h*-BN sheet. The origin of the hybrid states between top of the VB and bottom of the CB were also confirmed to be from the carbon domains through calculations of the LDOS for the rectangular graphene domain (e.g., the blue curve in Fig. 42 (b) shows the LDOS for R-7 domain).
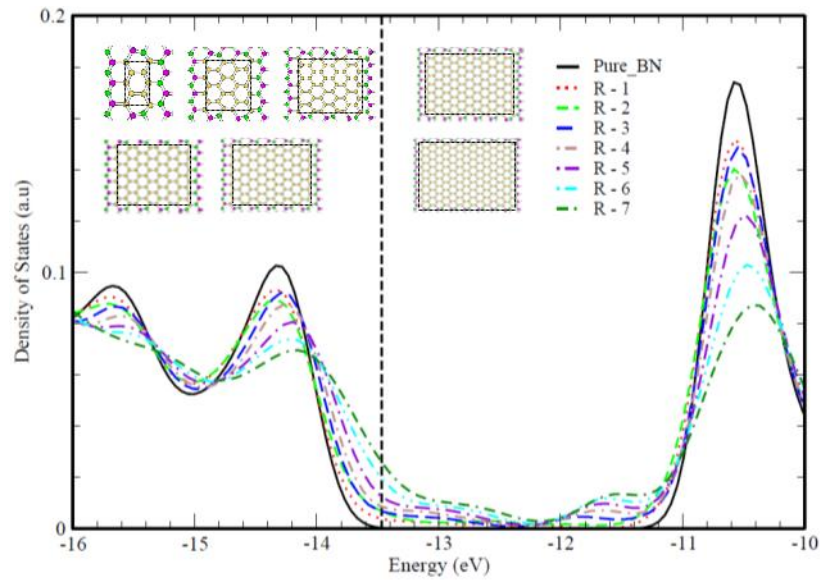
Figure 42. (a) The densities of states results for rectangular *h*-BN/C hybrid sheets sheet calculated using SCED-LCAO. The Fermi level of the *h*-BN sheet is denoted by the black dashed line. The insets show the relaxed structures corresponding to rectangular *h*-BN/C hybrid sheets for rectangular graphene domains of different sizes.
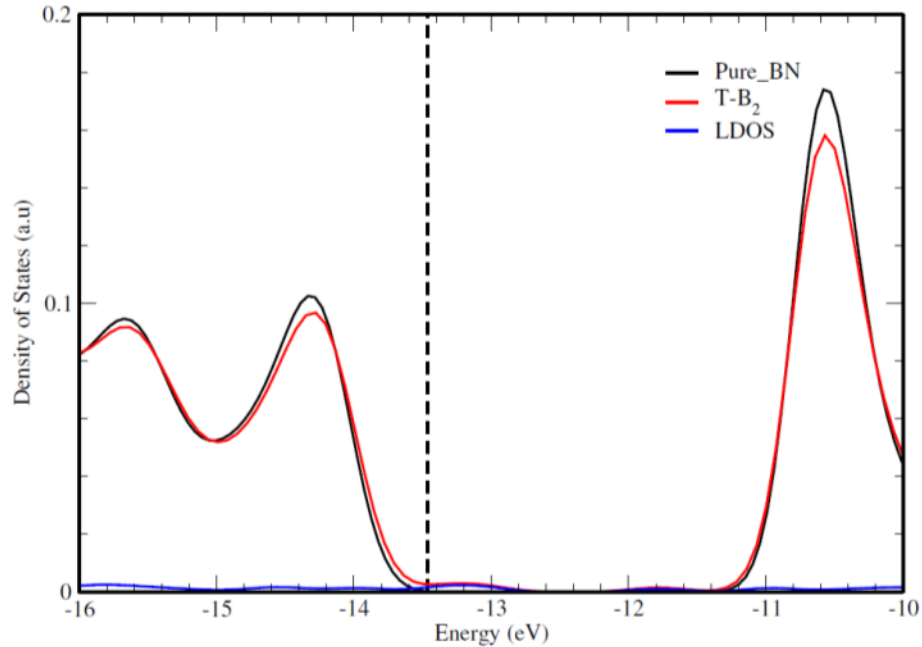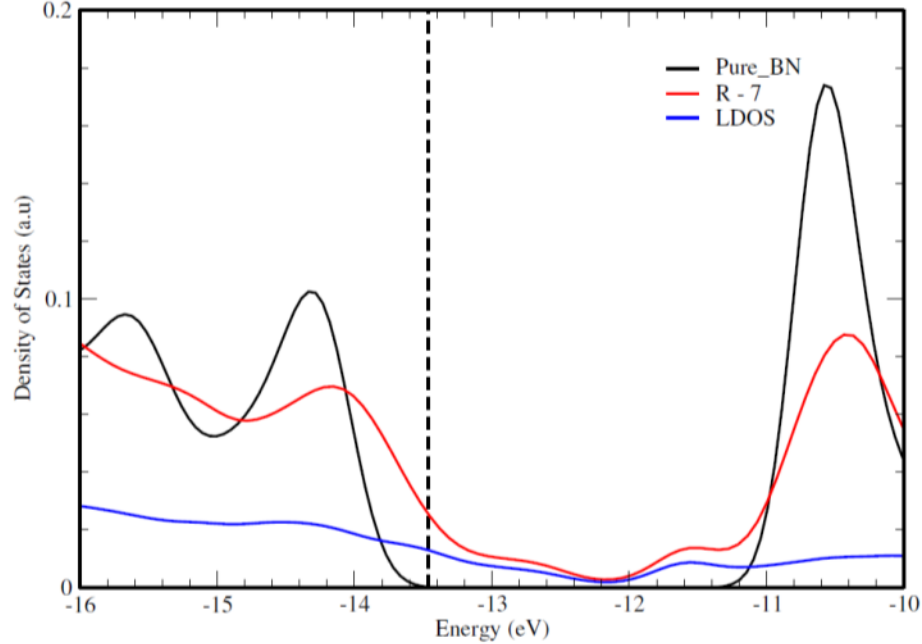
Figure 42. (b) The local density of states located at the carbon domain for R-7 (blue) together with the total DOS for pristine *h*-BN (black) and R-7 (red) respectively. The dotted black line shows the Fermi level of pristine *h*-BN.

5.1.5 Energy gap

Fig. 43 shows the calculated energy gap as a function of the area of graphene domains corresponding to different shapes in hybrid *h*-BN/C sheets. The values of the Fermi energy, energies for the highest valence and the lowest conduction bands, and the energy gap for all *h*-BN sheets with different shapes and sizes of graphene domains are listed in Table 12. For the case of Triangular-B graphene domains (black dots) with boron atoms at the boundary replaced by carbon, there exits only C-N bonds (~ 1.2 Å) at the boundary. On the other hand, since the bonds that exist within the boundary are C-C bonds (~1.46 Å), and those existing outside the boundary are B-N bonds (1.5 Å), a mismatch among the three types of bond lengths in the vicinity of the boundary causes a local strain in the system. This strain increases as the domain size increases, and we find that only the two smallest Triangular-B domains (i.e., T-B$_1$ and T-B$_2$) are stable in our SCED-LCAO

100

simulations. The energy gap corresponding to these cases are 3.0 eV and 0.7 eV, respectively. There is not much in the energy gap for the h-BN/C sheet labeled T-B$_1$ relative to the pristine h-BN sheet (3.3 eV), since the substitution of boron by carbon atoms takes place at only at three alternating locations of a hexagonal ring in the h-BN sheet. Essentially, a low % of carbon substitution into the h-BN sheet has little influence on the energy gap. On the other hand, the energy gap for the T-B$_2$ case shows a big reduction in the energy gap relative to the pristine h-BN sheet. The reduction in the energy gap is associated with slight distortions of hexagonal rings at the boundary of the domain that manifest as defect states in the density of states (see, Fig. 38 (a)).

For hybrid sheets with Triangular-N graphene domains (red squares), the carbon atoms at the boundary of the domain are bonded with boron atoms only. Since boron atoms are electron deficient, they do not prefer to form sp^2 type of C-B bonds, but prefers to form a three-center two-electron type of B-B bonds with the next nearest neighbor boron atoms upon relaxation of the structure. Consequently, the symmetry of the graphene domain is broken and the domain boundary exhibits distortion, creating many defect states at the top of VB and at the bottom of the CB. The energy gap in such hybrid h-BN sheets show a drastic reduction in the energy gap compared to pristine h-BN sheets with gap values ranging from $\sim$ 0.01-0.3 eV, except in the case of T-N$_1$ (E$_g$ $\sim$ 0.9 eV) where the smallest triangular domain is not a carbon domain but a triangular domain containing boron atoms.

For circular graphene domains (green diamonds), the initial unrelaxed structures have the same number of C-B bonds and C-N bonds at the boundary. Since their bond lengths are different, one expects local strains at the domain boundary. However, these bonds are distributed uniformly and, therefore, the local strain arising from the differences

in bond lengths is not that drastic upon relaxation. This may be the reason why the density of states is somewhat insensitive to the size of the circular graphene domain. The new states found in the gap must arise from states associated with C-B and C-N bonds along the boundary and the states associated with the graphene domains. For larger graphene domains, the contributions to these states come mainly from the carbon domain.

For the case of hexagonal hybrid h-BN/C sheets, the initial structures contain complete hexagonal carbon rings within the graphene domain. Since the six-fold symmetry of hexagonal rings is not broken upon relaxation, there are no symmetry-broken states within the gap. As the size of the carbon domain increases, the energy gap oscillates as the size of the graphene domain increases and this behavior is attributed to the aromaticity property of the carbon rings [75]. There are C-B bonds and C-N bonds along the domain boundary and the number of such bonds of each type are the same, and hence less distortions along the boundary. The contributions to the total density of states from C-B and C-N bonds are in general small compared to contributions from C-C bonds. The size of graphene domain dictates practically the energy gap.

For the case of rectangular graphene domains embedded in h-BN/C sheets, as the size of the domain increases, one observes the valence band edge to move towards the Fermi level and the conduction band edge moving away from the Fermi level. Additionally, one can see new shoulders near the conduction band edge. Since rectangular graphene domains are such that each of the opposite sides of the zig-zag domain have different bonds, namely, C-N and C-B bonds, respectively, and, therefore, the perimeter of this domain is under local strain. However, on the armchair side of the domain, the C-N bond and C-B bonds alternate with each other. The net strain exhibited by the domain

leads to the change of the energy gap of the hybrid *h*-BN/C sheet. The energy gap oscillates between 0.4 eV and .05 eV within a small energy window.

In summary, by embedding carbon domains in *h*-BN sheets, their energy gaps can be manipulated. Both the carbon domain size and its shape influence the energy gap of pristine *h*-BN sheets. Since the properties contained in the database of the SCED-LCAO method mimics that of the DFT method, the absolute value of the energy gap obtained here must be used cautiously, but the relative trend obtained for the energy gap as a function of shape and size provides useful guidelines for materials design. Our results suggest that for controlled tuning of the energy gap of *h*-BN sheets, circular and hexagonal carbon domains are preferable. A summary of the Fermi level, energy at the top of the valence band and energy at the bottom of the conduction band is given in Table 12. Our results for this study have been presented on the APS March Meeting in 2015 [81].
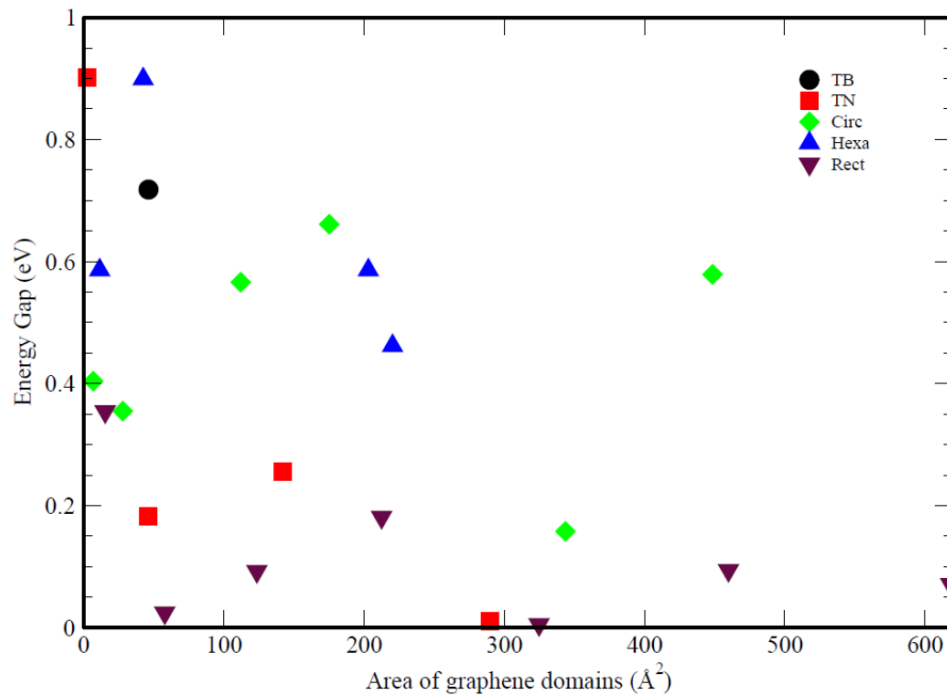
Figure 43. Energy gap versus area for graphene domains of different shapes and types (triangular, circular, hexagonal, or rectangular) embedded into *h*-BN sheets. An oscillatory behavior for E_g versus area is obtained.

Graphene domains	E_{VB} (eV)	E_F (eV)	E_{CB} (eV)	E_{gap} (eV)
T-B$_1$	-13.8610	-13.86944	-10.7392	3.122
T-B$_2$	-11.7117	-13.91695	-10.0034	0.718
T-N$_1$	-12.88285687	-12.88285686	-11.98153220	0.901
T-N$_2$	-13.106367	-12.9247937	-12.92479360	0.182
T-N$_3$	-12.71577220	-12.459977920	-12.45997791	0.256
T-N$_4$	-12.9777402	-12.9764216	-12.96775499	0.01
C-1	-13.212627	-13.001213	-12.808575	0.404
C-2	-12.78322	-12.59705	-12.42672	0.355
C-3	-12.98228	-12.67170	-12.41622	0.566
C-4	-13.02209	-12.82156	-12.360838	0.661
C-5	-12.72373	-12.64491	-12.56616	0.158
C-6	-12.88629	-12.48535	-12.307118	0.579
H-1	-13.09378	-12.508276	-12.50739	0.586
H-2	-13.1348	-12.66801	-12.2363	0.899
H-3	-13.0285	-12.7774	-12.44296	0.586
H-4	-12.94113	-12.76493	-12.478915	0.462
R-1	-13.13712	-12.93149	-12.7833	0.354
R-2	12.8533	-12.8401	-12.8288	0.025
R-3	-13.0057	-12.959597	-12.9134	0.092
R-4	-12.83747	-12.83316	-12.6565	0.181
R-5	-12.81360	-12.81097	-12.80833	0.005
R-6	-12.67457	-12.6648	-12.5804	0.094
R-7	-12.6439	-12.5736	-12.5732	0.071

Table 12. Fermi levels, energies for the highest valence and lowest conduction bands, and corresponding energy gaps of graphene domains on h-BN sheet. Triangular boron (T-B), triangular nitrogen (T-N), circular (C), hexagonal (H) and rectangular (R) graphene domains are listed respectively.

5.2 Band Gap Opening in Patterned Graphene Structures with Holes ("Holey Graphene")

In the last section, we focused on tuning the large band gap of h-BN down by embedding the graphene domains. Graphene is known to be a gapless material. In this section, we ask the question whether, by carving holes of different shapes and sizes, one can open a gap in graphene. We will use the SCED-LCAO method to determine whether holey graphene structures are stable. If stable structures are obtained, we will calculate the

electronic density of states to ascertain the dependence of shape and size of patterned holes in graphene on the energy gap.

For this study, we considered a supercell of size 15x10 and the largest size of the patterned hole in the graphene sheet was chosen carefully so that interactions between neighboring holes are avoided. The shapes of the holes proposed are triangular, rectangular and circular (see Fig. 44). Through SCED-LCAO molecular dynamics, we will investigate the effect of the different hole shapes and sizes on opening the energy gap of a graphene sheet.
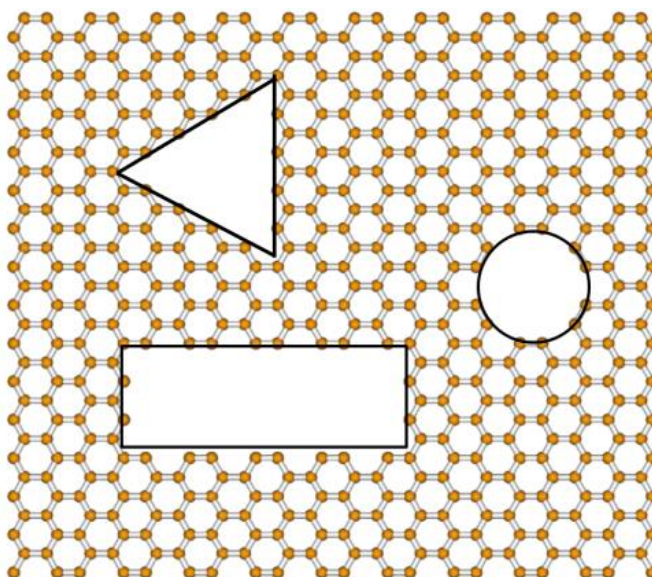
Figure 44. Patterned holes of different shapes etched into a graphene sheet referred hereafter as "holey [82] graphene."

5.2.1 Holey triangular graphene sheets

The first type holey graphene sheet considered in this work is patterned triangular holes. Five different triangular holey sheets were chosen. The triangular holey graphene sheets 1, 3 and 5 have zigzag boundaries with the apex regions of these triangular domains containing incomplete pentagons. The shortest distance between any two sides of these

105

triangular domains is2.484 Å. On the other hand, triangular holey graphene 2 and 4 have complete hexagons at the vertices. We found that after lattice optimization and complete relaxation, for the first three sets of holey triangular sheets mentioned above (1, 3 and 5) both holey graphene sheet 1 and holey 5 kept the incomplete pentagons at their respective vertices with their separations becoming closer, i.e., 1.89 to 2.0 Å for holey 1, and 1.83 to 1.85 Å for holey 5, respectively. On the other hand, for holey triangular 3, two of the pentagons at two of the vertices form complete pentagons with bond lengths of 1.586 and1.66 Å, respectively, and the third pentagon remains open with a separation of 1.873 Å. For holey triangular 2 and 4, the hexagons at the vertices are slightly deformed after relaxation but still intact (see the insets of Fig. 45). In terms of the effect from the different holey triangular sheets on the energy gap, as compared to that of pure graphene, we found that if the vertices of the holey triangles keep their incomplete pentagons with the separations becoming closer, a small gap of $E_g \approx 0.1\ eV$ gets opened (e.g., in holey triangular 1 and 5). But, if the vertices of the triangles are complete hexagons or at least one is a complete pentagon, such as in holey triangular 2, 3 and 4 (see Fig. 45), it is hard to see the gap opening.
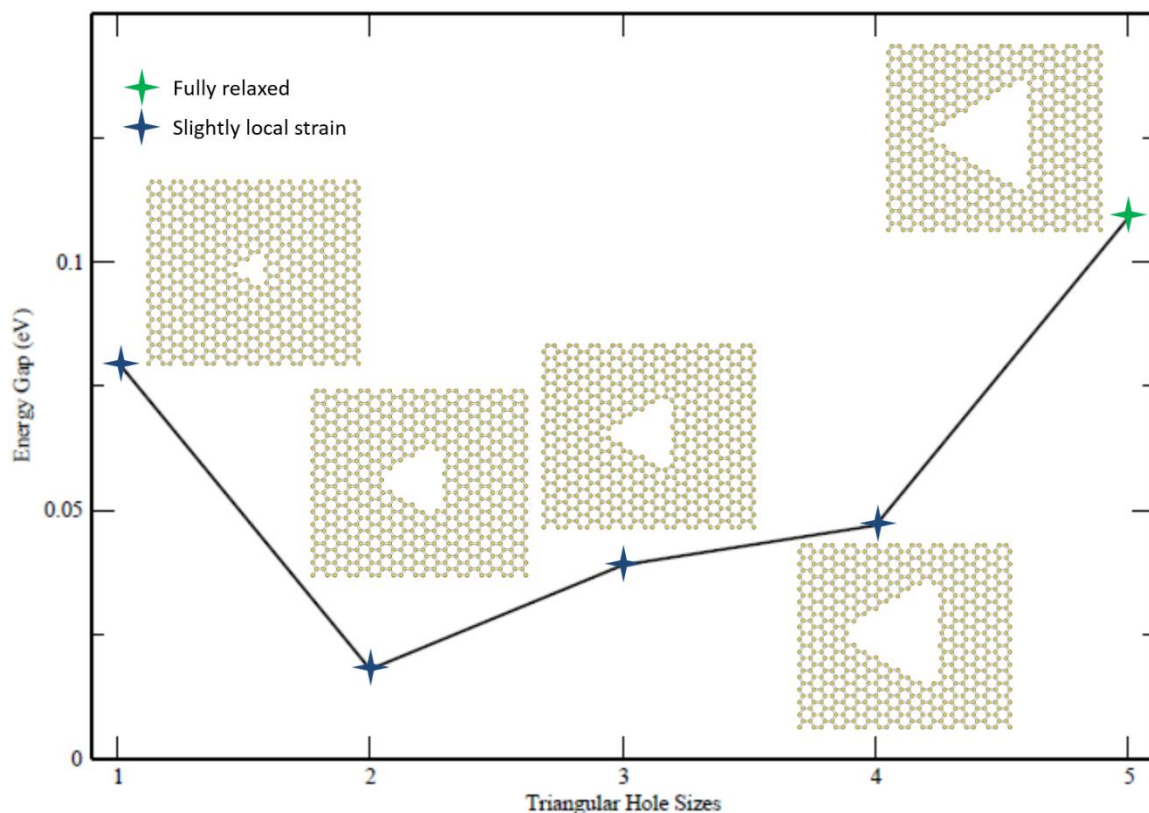
Figure 45. The calculated values of the energy gap of a graphene sheet embedded with triangular holes ("holey triangular graphene") of increasing sizes. The inset shows the relaxed structures corresponding to the different cases studied.

5.2.2 Holey circular graphene sheets

In this section, we study the effect of patterned graphene sheets with circular holes of different sizes. A total of four holey circular graphene sheets was considered with hole sizes corresponding to areas $103.43, 161.61, 316.77$ and $413.74 \, \text{Å}^2$, respectively. These circular holes were created by removing the carbon atoms inside a circle centered at the center of a hexagon. The unrelaxed structure of holey graphene 1 has its boundary formed by alternating hexagons and open polygons. In total, there are six hexagons and six incomplete polygons at the boundary. The incomplete polygons have separations of $2.485 \, \text{Å}$ and after MD relaxation, the separation distances become closer in the range of 2.15 to $2.19 \, \text{Å}$.

The holey circular graphene 2 also has 6 hexagons forming the circular holes, but in contrast to holey circular 1, in holey circular graphene 2 the 6 hexagonal carbon networks are separated by carbon atoms in zigzag structures and the distances between any two hexagons is $\approx 4.97\,\text{Å}$ before relaxation. After SCED-LCAO MD relaxation, we found the diameter of the circular hole to expand slightly and the hexagonal networks at the domain boundary to be distorted with the separation distance between some of the hexagon increasing to $6.11, 6.13$, and $7.45\,\text{Å}$ respectively while decreasing between 4.54 and $4.69\,\text{Å}$, respectively for the remaining hexagons.

For holey circular 3, there are two types of hexagonal networks at the boundary: (i) hexagons separated by arm-chair configurations and (ii) those separated by incomplete polygons. The hexagons, the incomplete polygons, and the arm-chair configurations alternate along the perimeter of the circular hole. The separation distance between hexagons separated by incomplete polygons is $2.486\,\text{Å}$. After relaxing the structure, the holey circular graphene 3 expands its diameter with the hexagons separated by arm-chair structures getting closer with a separation of 2.66 to $2.67\,\text{Å}$ while the ones separated by incomplete polygons have wider separations of $4.95\,\text{Å}$.

For holey circular 4, the hexagonal carbon networks are separated by either zigzag or arm-chair networks. The separation between hexagons due to arm-chair configuration before relaxation is $2.869\,\text{Å}$ while that due to the zigzag configurations are $4.969\,\text{Å}$. For the holey circular graphene 4, after relaxations the shortest separation between two hexagons is for hexagons separated by arm-chair networks and this separation ranges from 2.67 to $2.69\,\text{Å}$ while for the hexagons separated by zigzag networks, their separation

became wider and ranged between 7.42 to 7.43 Å. A small buckling was observed at the edges of the circular hole 4.

The energy gap opening corresponding to circular holes in graphene of different sizes is shown in Fig. 46. The amount of stress introduced in graphene due to different sized circular holes is different. For each case studied, the hole boundary has different types of edges and corners. A sharper boundary appears to facilitate the band gap opening more. Graphene sheets labeled holey circular 3 has the largest band gap opening (approximately, 0.32 eV).
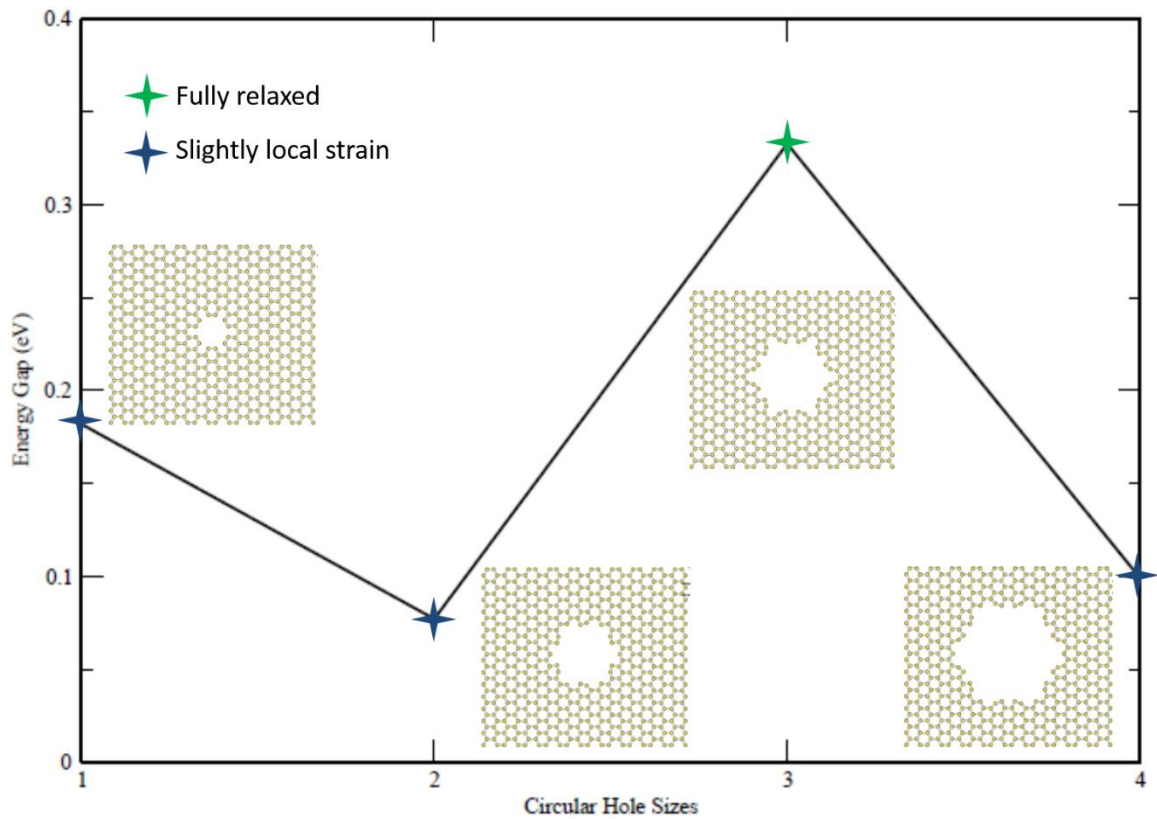
Figure 46. The calculated values of the energy gap of a graphene sheet embedded with circular holes ("circular holey graphene") of increasing sizes. The inset shows the relaxed structures corresponding to the different cases studied.

5.2.3 Holey rectangular graphene sheets.

A total of 16 different rectangular holes were constructed but 5 are considered to be in pairs of the same rectangular sizes with different configuration. A complete description for the different holey rectangular graphene sheets will be given in the appendix A. Using SCED-LCAO MD code all the holey rectangular graphene structures were fully relaxed. We found that structurally, the rectangular holes in which the area of the rectangles are free from the interference of any Carbon atom (as in holey rectangular 1, 2_2nd, 3, 4_2nd, 5, 6, 7_2nd, 8, 9_2nd, 10 and 11_2nd) have a reconstruction of the hexagons forming the boat configuration on the holey sides. The atoms closest to the corners of these two sides tend to push away from the corners and move towards the center of their respective sides. This leads to the distances between two hexagons on either side of a boat configuration becoming closer or moving away from each other if the boat configuration is around the center of the actual side. On the other hand, the holey rectangular structures having Carbon atoms within their respective area (as in holey rectangular 2_1st, 4_1st, 7_1st, 9_1st and 11_1st) have been found to have their atoms at each sides of a boat configuration to be getting closer to each other. For the structures with smaller rectangular area among this–group, the incomplete pentagons/hexagons tend to close up. But as the size of the rectangles increases, the incomplete nature is kept.

For all types of rectangular holes, the zigzag sides kept their initial configurations throughout the relaxation process. Through the electronic density of states calculations, we found that by creating rectangular holey graphene sheet can open an energy gap from the 0 *eV* gap known for graphene (See Figs. 47-48). The first set of holey rectangular graphene sheets mentioned above is divided into three groups: group (1) has no hexagon present (as

in holey rectangular 1 and 2_2nd), group (2) has an even number of hexagons (as in holey rectangular 5, 8 and 9_2nd), and group (3) has an odd number of hexagons (as in holey rectangular 3, 4_2nd, 6, 7_2nd, 10 and 11_2nd) along their respective boat configuration sides. It was found that, in group (1), the extension of the two zigzag sides leads to a decrease in energy gap as the area of the rectangular hole is increased; in group (2), the decrease in energy gap is also proportional to the extension of the zigzag sides but is indirectly proportional to the area of the holey. Such indirect proportionality between the area and energy gap was also observed in group (3), such as from the holey rectangular 3 to 4_2nd and from the holey rectangular 10 to 11_2nd; but an exception was detected such as from the holey rectangular 6 to 7_2nd where a significant opening of the energy gap with the extension of the zigzag sides was found. In general, we can however say that for this first set of holey rectangular sheets a possible bang gap opening is realistic and it is indirectly proportional to the extension/contraction of the zigzag sides of the holes within the graphene sheets.
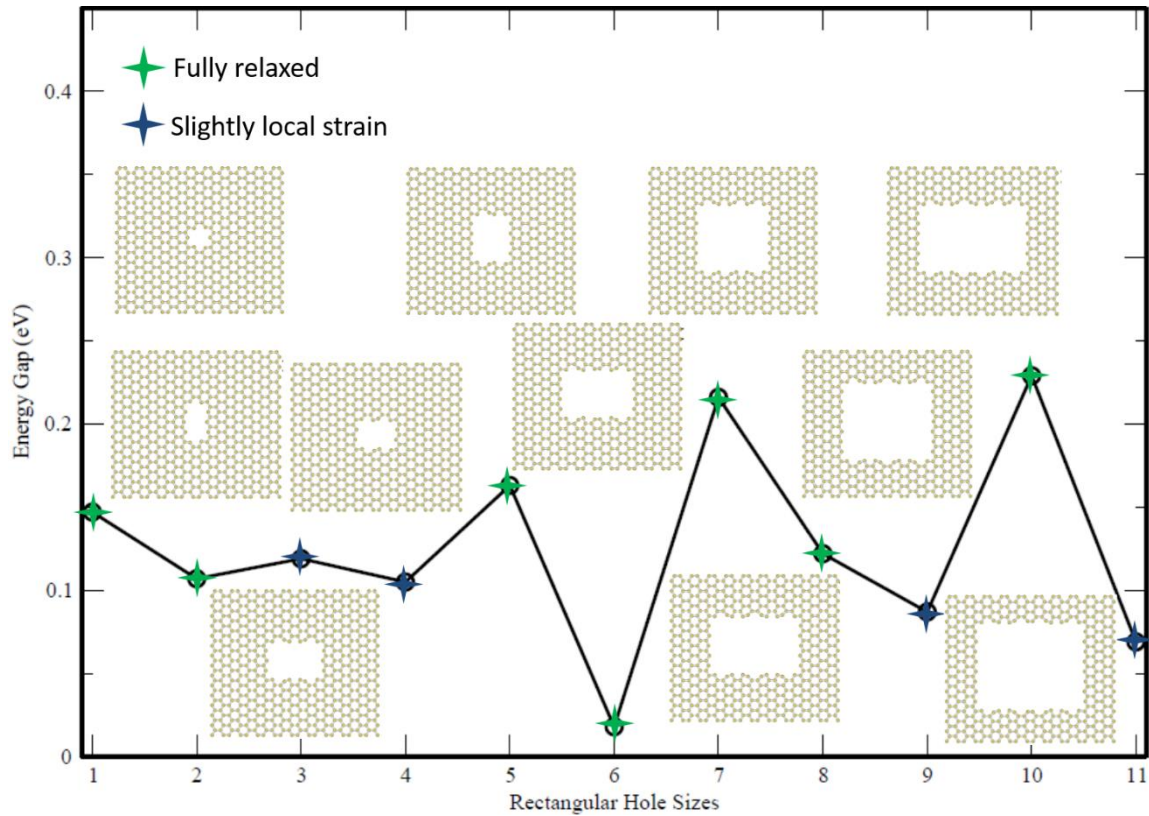
<u>Figure 47.</u> Energy gap dependence on the size of the rectangular holes for the first set of the rectangular holes. Insets show the different relaxed structures in the first set of rectangular holes (1, 2_2nd, 3, 4_2nd, 5, 6, 7_2nd, 8, 9_2nd, 10 and 11_2nd).

For the second set of rectangular holes, incomplete pentagons/hexagons are present at the four corners and Carbon atoms with dangling bonds are within the areas of the holes (holey rectangular 2_1st, 4_1st, 7_1st, 9_1st and 11_1st). We found a nearly linear proportionality between the energy gap and the area of the rectangular holes. The energy gap ranges between $E_g = 0.107$ to $E_g = 0.403\ eV$.
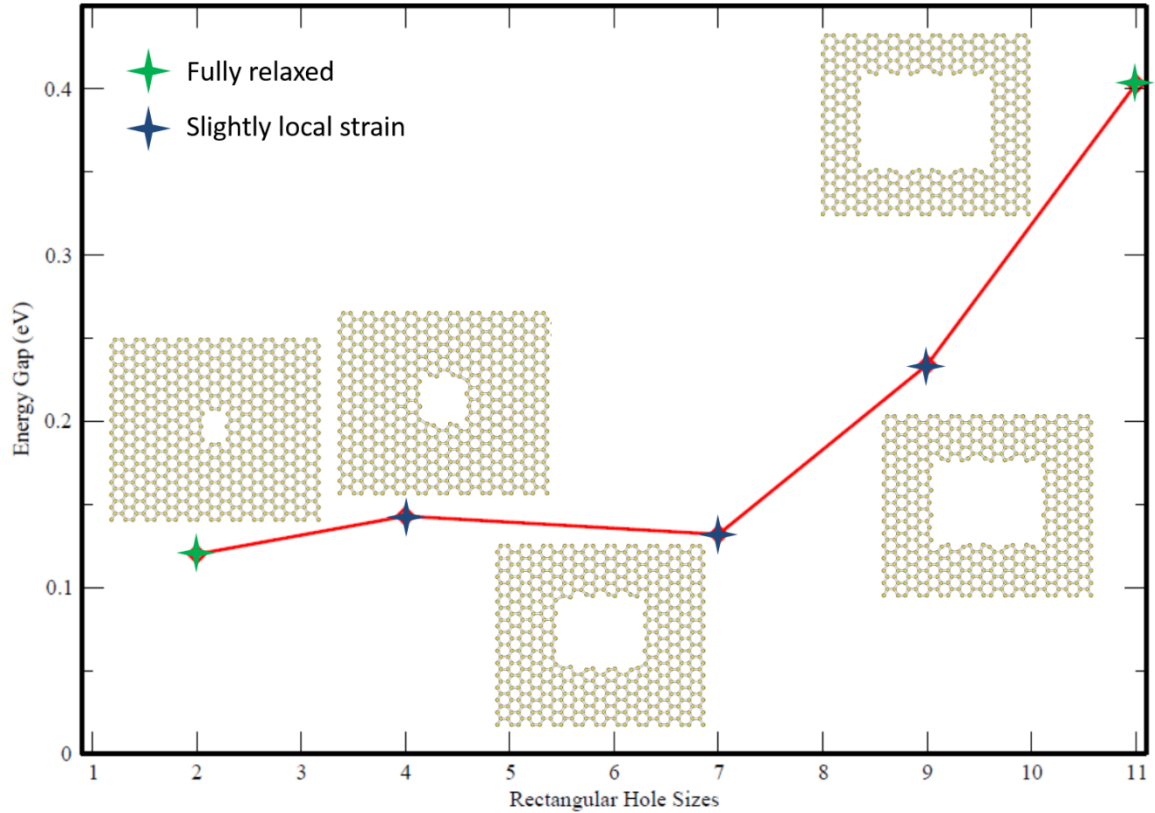
Figure 48. Energy gap dependence on the size of the rectangular holes for the second set of the rectangular holes. Insets show the different relaxed structures in the second set of rectangular holes (2_1st, 4_1st, 7_1st, 9_1st and 11_1st).

Based on our results discussed above, we found that it is possible to open the energy gap of graphene sheet by patterning holes of different shapes and sizes in a graphene sheet. In general, the energy gap versus size of the patterned hole curve shows an oscillating pattern but the envelope of this curve has a positive slope, indicating that a graphene sheet with larger holes will in general exhibit larger energy gaps. In order to have a clear understanding of the gap opening, we performed local analysis. The nearest neighbor and the charge transfer on the atoms at the boundary are analyzed and summarized in Appendix B. We found that most atoms located at the edge of the holes have dangling bonds and lost their charges (from 0.006 to 0.142 e), but must atoms located at the corners keep their 3 neighbors and most of them gain charges (from 0.001 to 0.057 e). Definitely the existence

113

of dangling bonds and charge transfer lead to the breaking of band structure symmetry at the Dirac point and hence a gap opening.

CHAPTER VI

SUMMARY AND OUTLOOK

This section highlights some of the major findings of this dissertation. Through a series of studies on complex low-dimensional boron nanostructures, patterned two-dimensional sheets of graphene "holey graphene", and patterned two-dimensional h-BN sheets with graphene domains, we have established that a semi-empirical approach based on the SCED-LCAO Hamiltonian is a powerful computational technique for designing materials with desired electronic properties. The projects undertaken in this dissertation demonstrate that the SCED-LCAO approach is quite robust for boron containing and nitrogen containing compounds and systems. Because of its complex chemistry, boron is notoriously difficult to describe in a semi-empirical approach. Since nitrogen is highly electronegative, unless charge transfers in an aggregate of heterogeneous clusters, are captured correctly, usually semi-empirical approaches tend to fail. The SCED-LCAO approach passes many of these stringent tests, making it a predictive computational tool for materials design.

The first application chosen for this stringent test was in predicting one- and two-dimensional structures of boron based on icosahedral B_{12} units. The infinite one-dimensional icosahedral B_{12} chains were stable and this system exhibited an energy gap of 0.74 eV. We also found a ring structure containing six icosahedral B_{12} units to be energetically stable with this structure exhibiting a semiconducting behavior. Encouraged

by these stable systems based on B_{12} icosahedra, we designed three types of two-dimensional sheets based on B_{12}icosahedra (δ_6, α, and δ_4). Both δ_6 and δ_4 boron sheets exhibited semiconducting properties while α icosahedral sheet exhibited metallic properties. Among the boron sheets investigated, the δ_6 sheet had the lowest energy, *i.e.,* the most stable B_{12}-based boron sheet.

Prompted by a recent research on the synthesis of ultrathin boron sheets (i.e., 8-12 nm or 20 layers) containing thin films of α-tetragonal B_{50}, we performed simulations based on the SCED-LCAO method to test the stability of monolayer α-tetragonal B_{50} sheet. We found this structure to be unable to keep the α-tetragonal B_{50} symmetry. We feel that only a study of a multi-layer α-tetragonal B_{50} sheet can confirm the experimental observation. This work is undertaking, and we do found, from our preliminary results, that the two/three/four layered α-tetragonal B_{50} sheets indeed are stable keeping the α-tetragonal B_{50} symmetry.

A significant amount of the effort on this dissertation was devoted to the development and parameterization of the SCED-LCAO Hamiltonian for nitrogen. The heart of any transferable semi-empirical approach is the database used for the parametrization. We generated a database for the structure and properties of nitrogen containing heterogeneous clusters (*e.g.,* C_nN_m, B_nN_m, and Ga_nN_m) using a first-principles method available within the Gaussian package. Three different sets of optimized parameters for nitrogen were generated, corresponding to different cluster properties included in the database. These optimized SCED-LCAO Hamiltonian parameters were tested by checking how well they reproduced the lattice constants and energy gaps of

different nitrogen containing structures such as h-BN sheet, crystalline w-BN bulk and crystalline *w*-GaN bulk.

The best parameterized set is expected to be readily transferable to different environments. One such optimized set for nitrogen was used in subsequent studies involving the band gap engineering *h*-BN sheets. In this dissertation, we patterned the *h*-BN by embedding graphene domains of different shapes (triangular, circular, hexagonal and rectangular) and studied how such domains would influence the energy gap of this hybrid 2D sheet. We found from the densities of states calculations that the valence and conduction bands of the *h*-BN sheet retain their basic shapes, but the energy gap between the valence band and the conduction band is strongly dependent on the shape and size of the graphene domains. The hybrid 2p orbitals between B and C, and N and C, appear at the band gap region, either mainly at the top of the valence band, or at the top of the conduction band, or both, depending on the shapes and the size of the graphene domains. We found that, in the domain range of < 600 Å^2, irrespective of the shape of the graphene domain, the energy gap oscillates as the domain size of graphene is increased. This gap oscillation is, perhaps, related to the ratio of the number of complete and incomplete hexagonal rings in a given graphene domain. In particular, the h-BND sheet with hexagonal domains containing complete hexagonal rings and circular domains show the trend to reduce the band gap when the domain size is over 600 Å^2.

In an effort to understand how the SCED-LCAO tool could be further utilized for band gap engineering of materials, we also studied the energy gap variation of graphene sheets embedded with different shapes and sizes of holes. It was found that it is possible to open the energy gap of an otherwise gapless graphene sheet by patterning holes of

different shapes and sizes in a graphene sheet. In general, the energy gap versus size of the patterned hole curve shows an oscillating pattern but the envelope of this curve has a positive slope, indicating that a graphene sheet with larger holes will in general exhibit larger energy gaps. It was also found that a graphene sheet with larger patterned holes was also energetically more stable. More specifically, it was found that: (i) triangular holey graphene sheets yielded the smallest possible energy gap opening (0.04 to $0.11\ eV$), (ii) the circular holey graphene sheets exhibited an energy gap in range of 0.1 to $0.35\ eV$, and (iii) the rectangular holey graphene sheets exhibited an energy gap in the range 0.1 to $0.4\ eV$.

The main findings of this dissertation are as follows:

- The SCED-LCAO method predicted a new family of low dimensional boron nanostructures based on B_{12} icosahedra.

- Monolayer boron sheets with α-tetragonal B_{50} symmetry cannot keep the symmetry but multilayered α-tetragonal B50 could keep the symmetry.

- By embedding graphene domains in h-BN sheets or by embedding holes in pristine graphene sheets, it is possible to engineer the energy gaps of a wide-band gap material and a gapless material, respectively.

We would like to remark that while holey graphene structures and hybrid h-BN sheets with graphene domains have been synthesized, there are no experiments on 2D boron sheets as proposed in this dissertation.

6.1 Ongoing work

As it was suggested in the introduction of this dissertation, we engaged into preliminary studies for two, three and four layers of α-tetragonal B_{50} structures and investigated their respective stabilities. Starting with a relaxation of the above stated multi-layered structures for α-tetragonal B_{50} we found that all three structures are stable. The icosahedrons that compose the structures are not deformed as was observed in the single layered α-tetragonal B_{50} and the presence of the boron atoms with dangling bond did not lead to a change in their overall bonding nature. Figure 49 below shows the top and side views for the relaxed two-layered and three-layered α-tetragonal B_{50} structures. We are now engaged in optimizing these different structures and investigate their respective structural and electronic properties.

(a)   (b)

(c)   (d)
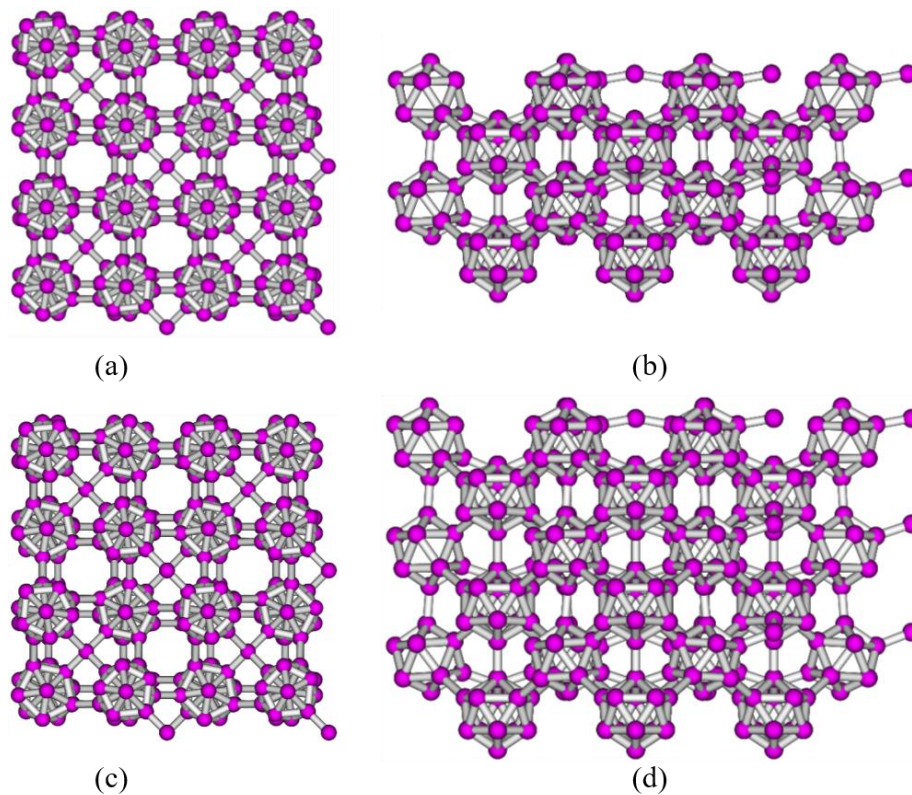
Figure 49. Relaxed structures for two-layered α-tetragonal B_{50} (top panel) and three-layered α-tetragonal B_{50} (bottom panel). (a) and (c) top views, (b) and (d) side views.

REFERENCES

1. Kohn, W. and L.J. Sham, *Self-Consistent Equations Including Exchange and Correlation Effects.* Physical Review, 1965. **140**(4A): p. A1133-A1138.
2. Leahy, C., et al., *Coherent treatment of the self-consistency and the environment-dependency in a semi-empirical Hamiltonian: Applications to bulk silicon, silicon surfaces, and silicon clusters.* Physical Review B, 2006. **74**(15).
3. Yu, M., S.Y. Wu, and C.S. Jayanthi, *A self-consistent and environment-dependent Hamiltonian for large-scale simulations of complex nanostructures.* Physica E: Low-dimensional Systems and Nanostructures, 2009. **42**(1): p. 1-16.
4. Tandy, P., et al., *Next generation of the self-consistent and environment-dependent Hamiltonian: Applications to various boron allotropes from zero- to three-dimensional structures.* J Chem Phys, 2015. **142**(12): p. 124106.
5. Novoselov, K.S., et al., *Electric Field Effect in Atomically Thin Carbon Films.* Science, 2004. **306**(5696): p. 666-669.
6. Wu, X., et al., *Two-Dimensional Boron Monolayer Sheets.* ACS Nano, 2012. **6**(8): p. 7443-7453.
7. Tang, H. and S. Ismail-Beigi, *First-principles study of boron sheets and nanotubes.* Physical Review B, 2010. **82**(11).
8. Parakhonskiy, G., et al., *Experimental pressure-temperature phase diagram of boron: resolving the long-standing enigma.* Sci Rep, 2011. **1**: p. 96.
9. Kresse, G. and J. Hafner, *Ab initiomolecular dynamics for open-shell transition metals.* Physical Review B, 1993. **48**(17): p. 13115-13118.
10. Xu, J., et al., *Ultrathin Single-Crystalline Boron Nanosheets for Enhanced Electro-Optical Performances.* Advanced Science, 2015. **2**(6): p. n/a-n/a.
11. Ci, L., et al., *Atomic layers of hybridized boron nitride and graphene domains.* Nat Mater, 2010. **9**(5): p. 430-5.
12. Bai, J., et al., *Graphene nanomesh.* Nat Nano, 2010. **5**(3): p. 190-194.
13. Oswald, W. and Z. Wu, *Energy gaps in graphene nanomeshes.* Physical Review B, 2012. **85**(11): p. 115431.
14. Jiang, L. and Z. Fan, *Design of advanced porous graphene materials: from graphene nanomesh to 3D architectures.* Nanoscale, 2014. **6**(4): p. 1922-1945.
15. Frauenheim, T., et al., *A Self-Consistent Charge Density-Functional Based Tight-Binding Method for Predictive Materials Simulations in Physics, Chemistry and Biology.* physica status solidi (b), 2000. **217**(1): p. 41-62.
16. Menon, M. and K.R. Subbaswamy, *Transferable nonorthogonal tight-binding scheme for silicon.* Physical Review B, 1994. **50**(16): p. 11577-11582.
17. Bernstein, N. and E. Kaxiras, *Nonorthogonal tight-binding Hamiltonians for defects and interfaces in silicon.* Physical Review B, 1997. **56**(16): p. 10488-10496.

18. Menon, M. and K.R. Subbaswamy, *Nonorthogonal tight-binding molecular-dynamics scheme for silicon with improved transferability.* Physical Review B, 1997. **55**(15): p. 9231-9234.

19. Papaconstantopoulos, D.A., et al., *Tight-Binding Hamiltonians for Carbon and Silicon.* MRS Online Proceedings Library Archive, 1997. **491**: p. null-null.

20. Wang, C.Z., B.C. Pan, and K.M. Ho, *An environment-dependent tight-binding potential for Si.* Journal of Physics: Condensed Matter, 1999. **11**(8): p. 2043.

21. Bernstein, N., et al., *Energetic, vibrational, and electronic properties of silicon using a nonorthogonal tight-binding model.* Physical Review B, 2000. **62**(7): p. 4477-4487.

22. Feldman, J.L., et al., *Tight-binding study of structure and vibrations of amorphous silicon.* Physical Review B, 2004. **70**(16): p. 165201.

23. Yu, M. 2012.

24. Tandy, P., *A semi-empirical Hamiltonian for boron, phosphorus and compounds containing boron, phosphorus and silicon.* 2013: Electronic Theses and Dissertations. p. 1417.

25. Smith, L., *Improved self-consistency for SCED-LCAO.* 2015: Electronic Theses and Dissertations. p. 2093.

26. Bullett, D.W., *Structure and bonding in crystalline boron and B 12 C 3.* Journal of Physics C: Solid State Physics, 1982. **15**(3): p. 415.

27. Boustani, I., *Systematic ab initio investigation of bare boron clusters:mDetermination of the geometryand electronic structures of ${\mathrm{B}}_{\mathrm{n}}$ (n=2\char21{}14).* Physical Review B, 1997. **55**(24): p. 16426-16438.

28. Atiş, M., C. Özdoğan, and Z.B. Güvenç, *Structure and energetic of Bn (n = 2–12) clusters: Electronic structure calculations.* International Journal of Quantum Chemistry, 2007. **107**(3): p. 729-744.

29. Boustani, I., *Structure and stability of small boron clusters. A density functional theoretical study.* Chemical Physics Letters, 1995. **240**(1–3): p. 135-140.

30. Boustani, I., *A comparative study of ab initio SCF-CI and DFT. Example of small boron clusters.* Chemical Physics Letters, 1995. **233**(3): p. 273-278.

31. Boustani, I., *New quasi-planar surfaces of bare boron.* Surface Science, 1997. **370**(2–3): p. 355-363.

32. Boustani, I., *New Convex and Spherical Structures of Bare Boron Clusters.* Journal of Solid State Chemistry, 1997. **133**(1): p. 182-189.

33. Boustani, I., Z. Zhu, and D. Tománek, *Search for the largest two-dimensional aggregates of boron: Anab initiostudy.* Physical Review B, 2011. **83**(19).

34. Romanescu, C., et al., *Probing the structures of neutral boron clusters using infrared/vacuum ultraviolet two color ionization: B11, B16, and B17.* J Chem Phys, 2012. **137**(1): p. 014317.

35. Piazza, Z.A., et al., *Planar hexagonal B(36) as a potential basis for extended single-atom layer boron sheets.* Nat Commun, 2014. **5**: p. 3113.

36. Zhai, H.J., et al., *Observation of an all-boron fullerene.* Nat Chem, 2014. **6**(8): p. 727-31.

37. Gonzalez Szwacki, N., *Boron Fullerenes: A First-Principles Study.* Nanoscale Research Letters, 2007. **3**(2): p. 49-54.

38. Gonzalez Szwacki, N., A. Sadrzadeh, and B.I. Yakobson, *B80 fullerene: an Ab initio prediction of geometry, stability, and electronic structure.* Phys Rev Lett, 2007. **98**(16): p. 166804.

39. Baruah, T., M.R. Pederson, and R.R. Zope, *Vibrational stability and electronic structure of aB80fullerene.* Physical Review B, 2008. **78**(4).

40.   Ceulemans, A., et al., *Chemical bonding in the boron buckyball.* Chemical Physics Letters, 2008. **461**(4-6): p. 226-228.

41.   Gonzalez Szwacki, N., A. Sadrzadeh, and B.I. Yakobson, *Erratum:B80Fullerene: AnAb InitioPrediction of Geometry, Stability, and Electronic Structure [Phys. Rev. Lett.98, 166804 (2007)].* Physical Review Letters, 2008. **100**(15).

42.   Gopakumar, G., M.T. Nguyen, and A. Ceulemans, *The boron buckyball has an unexpected Th symmetry.* Chemical Physics Letters, 2008. **450**(4-6): p. 175-177.

43.   Zhao, J., et al., *B80 and Other Medium-Sized Boron Clusters: Core–Shell Structures, Not Hollow Cages.* The Journal of Physical Chemistry A, 2010. **114**(37): p. 9969-9972.

44.   Gunasinghe, R.N., et al., *Dispersion corrections in the boron buckyball and nanotubes.* Applied Physics Letters, 2011. **98**(26): p. 261906.

45.   Li, F., et al., *B80 and B101-103 clusters: remarkable stability of the core-shell structures established by validated density functionals.* J Chem Phys, 2012. **136**(7): p. 074302.

46.   Otten, C.J., et al., *Crystalline Boron Nanowires.* Journal of the American Chemical Society, 2002. **124**(17): p. 4564-4565.

47.   Zhang, Y., et al., *Synthesis of crystalline boron nanowires by laser ablation.* Chemical Communications, 2002(23): p. 2806-2807.

48.   Meng, X.M., et al., *Boron nanowires synthesized by laser ablation at high temperature.* Chemical Physics Letters, 2003. **370**(5-6): p. 825-828.

49.   Boustani, I., et al., *New boron based nanostructured materials.* The Journal of Chemical Physics, 1999. **110**(6): p. 3176.

50.   Kunstmann, J. and A. Quandt, *Broad boron sheets and boron nanotubes: Anab initiostudy of structural, electronic, and mechanical properties.* Physical Review B, 2006. **74**(3).

51.   Lau, K.C. and R. Pandey, *Stability and Electronic Properties of Atomistically-Engineered 2D Boron Sheets.* The Journal of Physical Chemistry C, 2007. **111**(7): p. 2906-2912.

52.   Tang, H. and S. Ismail-Beigi, *Novel precursors for boron nanotubes: the competition of two-center and three-center bonding in boron sheets.* Phys Rev Lett, 2007. **99**(11): p. 115501.

53.   Singh, A.K., A. Sadrzadeh, and B.I. Yakobson, *Probing Properties of Boron α-Tubes by Ab Initio Calculations.* Nano Letters, 2008. **8**(5): p. 1314-1317.

54.   Yang, X., Y. Ding, and J. Ni, *Ab initioprediction of stable boron sheets and boron nanotubes: Structure, stability, and electronic properties.* Physical Review B, 2008. **77**(4).

55.   Penev, E.S., et al., *Polymorphism of Two-Dimensional Boron.* Nano Letters, 2012. **12**(5): p. 2441-2445.

56.   Kah, C.B., Tandy, P., Yu, M, Jayanthi, C. S., Wu, S. Y., *The Structure, Stability and Electronic Properties of a One-Dimensional Boron α-B12 Structure.* , in *APS March Meeting*. 2013.

57.   Golikova, O.A., et al., *Electrophysical properties of α-rhombohedral boron.* physica status solidi (a), 1984. **86**(1): p. K51-K54.

58.   Kah, C.B., et al., *Low-dimensional boron structures based on icosahedron B(1)(2).* Nanotechnology, 2015. **26**(40): p. 405701.

59.   Kah, C.B., Yu, M., Jayanthi, C. S., Wu, S. Y., *Structural Stability and Electronic Properties of Two-Dimensional Boron α-B12 Structures.*, in *APS March Meeting*. 2014: Denver.

60.   Vanderbilt, D., *Soft self-consistent pseudopotentials in a generalized eigenvalue formalism.* Physical Review B, 1990. **41**(11): p. 7892-7895.

61.   Kresse, G. and D. Joubert, *From ultrasoft pseudopotentials to the projector augmented-wave method.* Physical Review B, 1999. **59**(3): p. 1758-1775.

62.   Perdew, J.P., *Electronic Structures of Solids '91 ed P Ziesche and H Eschrig (Berlin: Akademie Verlag).* 1991: p. 11.

63.   Evgeny, A.E. and P.Z. Igor, *High-pressure high-temperature synthesis and structure of α-tetragonal boron.* Science and Technology of Advanced Materials, 2011. **12**(5): p. 055009.

64.   Li, D., Y.-N. Xu, and W.Y. Ching, *Electronic structures, total energies, and optical properties of \ensuremath{\alpha}-rhombohedral ${\mathrm{B}}_{12}$ and \ensuremath{\alpha}-tetragonal ${\mathrm{B}}_{50}$ crystals.* Physical Review B, 1992. **45**(11): p. 5895-5905.

65.   Blöchl, P.E., *Projector augmented-wave method.* Physical Review B, 1994. **50**(24): p. 17953-17979.

66.   Perdew, J.P., K. Burke, and M. Ernzerhof, *Generalized Gradient Approximation Made Simple.* Physical Review Letters, 1996. **77**(18): p. 3865-3868.

67.   Hoard, J.L., R.E. Hughes, and D.E. Sands, *The Structure of Tetragonal Boron1.* Journal of the American Chemical Society, 1958. **80**(17): p. 4507-4515.

68.   *Basic Parameters for Wurtzite BN Crystal Structure* [cited 2016; Available from: http://www.ioffe.ru/SVA/NSM/Semicond/BN/basic.html.

69.   Topsakal, M., E. Aktürk, and S. Ciraci, *First-principles study of two- and one-dimensional honeycomb structures of boron nitride.* Physical Review B, 2009. **79**(11).

70.   Watanabe, K., T. Taniguchi, and H. Kanda, *Direct-bandgap properties and evidence for ultraviolet lasing of hexagonal boron nitride single crystal.* Nat Mater, 2004. **3**(6): p. 404-9.

71.   Kubota, Y., et al., *Deep Ultraviolet Light-Emitting Hexagonal Boron Nitride Synthesized at Atmospheric Pressure.* Science, 2007. **317**(5840): p. 932-934.

72.   *Basic Parameters for Wurtzite GaN Crystal Structure.* [cited 2016; Available from: http://www.ioffe.ru/SVA/NSM/Semicond/GaN/basic.html.

73.   Monemar, B., *Fundamental energy gap of GaN from photoluminescence excitation spectra.* Physical Review B, 1974. **10**(2): p. 676-681.

74.   Koide, Y., et al., *Energy band-gap bowing parameter in an AlxGa1−x N alloy.* Journal of Applied Physics, 1987. **61**(9): p. 4540-4543.

75.   Logothetidis, S., et al., *Optical properties and temperature dependence of the interband transitions of cubic and hexagonal GaN.* Physical Review B, 1994. **50**(24): p. 18017-18029.

76.   Ramírez-Flores, G., et al., *Temperature-dependent optical band gap of the metastable zinc-blende structure \ensuremath{\beta}-GaN.* Physical Review B, 1994. **50**(12): p. 8433-8438.

77.   Su, C.-H., et al., *Energy gap in GaN bulk single crystal between 293 and 1237 K.* Journal of Crystal Growth, 2002. **235**(1–4): p. 111-114.

78.   Dingle, R., et al., *Absorption, Reflectance, and Luminescence of GaN Single Crystals.* Physical Review B, 1971. **3**(2): p. 497-500.

79.   Brandt, O., et al., *Surface reconstructions of zinc-blende GaN/GaAs(001) in plasma-assisted molecular-beam epitaxy.* Physical Review B, 1995. **52**(4): p. R2253-R2256.

80.   Li, J. and V.B. Shenoy, *Graphene quantum dots embedded in hexagonal boron nitride sheets.* Applied Physics Letters, 2011. **98**(1): p. 013105.

81.   Kah, C.B.K., S.; Smith, L.; Yu, M; Jayanthi, C. S.; Wu, S. Y., *Graphene islands embedded in hexagonal Boron-Nitride sheet: structural and electronic properties study.*, in *APS March Meeting*. 2015: San Antonio.

82.   Xu, Y., et al., *Holey graphene frameworks for highly efficient capacitive energy storage.* Nat Commun, 2014. **5**.

APPENDIX A

HOLEY RECTANGULAR GRAPHENE SHEETS.

Holey rectangular 1 is the smallest in size and its sides are made of zigzag configurations for two parallel sides and boat configuration for the other two sides. Holey rectangular 2 was identified as holey rectangular 2_1st. The structural configuration for this sheet was obtained in a way that 2 parallel sides have zigzag configurations while the other two sides have a complete hexagon hence contributing 2 Carbon atoms within the area of the rectangle and also 4 apparent incomplete pentagons at the corners of the rectangle hole. In total, 10 Carbon atoms are removed to form this structure. Holey rectangular 2_2nd was the second type in this pair and it was obtained by further removing the four Carbon atoms within the area of the previous rectangular hole. Hence two parallel sides have zigzag configuration while the other two parallel sides have boat configurations. A total of 20 Carbon atoms are removed to form holey rectangular Carbon 3 which has zigzag configurations in two parallel sides and boat configurations in the other two sides. The two sides with boat configurations are longer than the zigzag sides. Holey rectangular 4 also has two types as in holey rectangular 2. The first type which is holey rectangular 4_1st has 4 incomplete pentagons/hexagons at the corners of the rectangular hole and 4 complete hexagons, 2 on each one of the two parallel sides. The presence of these complete hexagons will lead to the presence of a total of 8 Carbon atoms within the area of the rectangle. A total of 28 Carbon atoms were removed to create holey rectangular 4_1st. By removal of the 8 atoms present within the area of rectangular 4_1st, holey rectangular 4_2nd will be created with a total of 36 Carbon atoms being removed. Rectangular holey Carbon sheet 5

was built through the removal of 42 Carbon atoms in the graphene sheet and it has the two distinct configurations: zigzag and boat on two parallel sides. On the sides with boat configurations, there is 2 complete hexagons on each side. Holey rectangular 6 was built by removal of a total of 72 Carbon atoms. It has two parallel sides with zigzag configuration and other two parallel sides with boat configurations. On these two sides, 6 complete hexagons are identified with 3 on each side. For holey rectangular 7 two different types are obtained: holey rectangular 7_1st in which the 4 corners have an incomplete pentagon/hexagon and the two sides having boat configuration have 4 visible hexagons which contribute a total of 16 Carbon atoms within the area of the rectangle. The other type of holey rectangular 7 is holey rectangular 7_2nd which is constructed by further removal of the 16 atoms within the area of the rectangle in type one. Hence for holey rectangular 7_2nd, a total of 104 Carbon atoms are removed. The two parallel sides having the boat configuration now has 3 distinct hexagons in each side within the perimeter of the rectangle. To build holey rectangular 8, 110 atoms of Carbon have been removed from the graphene sheet. This structure has a total of 8 complete hexagons 4 on each of the sides having the boat configurations as part of its perimeter. Holey rectangular 9 also is the 4th member of these rectangular hole domains having two types holey rectangular 9_1st and holey rectangular 9_2nd. In the first mentioned type of holey rectangular 9, 5 complete hexagons are identified on each side holding boat configuration which lead to a total of 20 Carbon atoms within the area of the triangle and also it leads to the formation of incomplete pentagons/hexagons at the corners of the rectangle. To get rid of the incomplete pentagons/hexagons at the corners of the rectangle, the 20 Carbon atoms found within the area of the first type are removed which gives a total of 130 Carbon atoms being removed

from the original graphene sheet. The two sides with configurations on holey rectangular 9_2nd now have 4 hexagons each as part of the perimeter of the rectangle. Holey rectangular 10 was built up by removal of 156 Carbon atoms from the graphene sheet. It has two parallel sides with zigzag configuration as in the previous structures and also two other parallel sides with boat configuration. In each of these two sides, 5 Carbon hexagons are counted along the perimeter of the rectangle formed by the hole. Holey rectangular 11 also has two types, in the first one a total of 180 atoms of Carbon are removed from graphene, and was identified as holey rectangular 11_1st. In this first type, 24 Carbon atoms are located within the area of the rectangle creating 4 incomplete pentagons/hexagons. The removal of these 24 Carbon atoms leads to a total of 204 atoms being removed from the original graphene structure. On the sides having boat configuration 5 hexagons are observed on each to be part of the perimeter of holey rectangular 11_2nd.

APPENDIX B

HOLEY GRAPHENE SHEETS – LOCAL ANALYSIS

We have performed local analysis for the holey graphene sheets with different shapes and sizes of holes. The Figures B.1 to B.25 show the relaxed holey graphene structures with the emphasis around the holes. The numbers in the figures denote the atom numbers. Tables B.1 to B.25 list a summary of the local analysis for the different holey graphene structures discussed in Chapter V of this dissertation. The second column gives the atom # which indicates the atoms located at the boundaries of the different holes. The * sign next to the atom numbers in the respective tables indicates (i) the atoms at the three vertices for the holey triangular graphene structures, (ii) the atoms at the edge of zigzag configurations separating two hexagons in the cases of the holey circular graphene structures, and (iii) the four atoms at the different corners for the holey rectangular graphene structures. The third column gives the nearest neighbors associated with the atoms listed in column 2 (within the cutoff 1.55 Å). Since the carbon atom in pristine graphene has 3 neighbors, there must be dangling bonds on the atoms around the boundary if they have less than 3 neighbors. The last column of each table shows the average charge gained (+) or lost (-) by the atom.

Figure B.1 Relaxed holey triangular graphene 1 near the hole area. The numbers identify the different atoms.

Structures	Atom #	Nearest Neighbors	Charge (e)
	218*	3	-0.012
	258	2	-0.087
	259	2	-0.087
	261	2	-0.023
	297	2	-0.023
Holey Triangular Graphene 1	298	2	-0.088
	300*	3	-0.013
	332	2	-0.087
	333	2	-0.023
	335	2	-0.088
	369*	3	-0.013
	371	2	-0.087

Table B.1 The atom numbers (2nd column), the nearest neighbors (3rd column), and the net charge (4th column) of atoms at the boundary of the holey triangular graphene 1.

Figure B.2 Relaxed holey triangular graphene 2 near the hole area. The numbers identify the different atoms.

Structures	Atom #	Nearest Neighbors	Charge (e)
	217*	2	+0.011
	218	2	-0.117
	220	2	-0.064
	254	2	-0.082
	255	2	-0.132
	257	2	-0.046
	287	2	-0.084
Holey Triangular Graphene 2	288*	2	-0.089
	317	2	-0.088
	318	2	-0.045
	348	2	-0.089
	349	2	-0.085
	351	2	-0.132
	384*	2	+0.002
	387	2	-0.115

Table B.2 The atom numbers (2nd column), the nearest neighbors (3rd column), and the net charge (4th column) of atoms at the boundary of the holey triangular graphene 2.

Figure B.3 Relaxed holey triangular graphene 3 near the hole area. The numbers identify the different atoms.

Structures	Atom #	Nearest Neighbors	Charge (e)
	176*	3	+0.049
	178	2	-0.029
	216	2	-0.061
	217	2	-0.090
	219	2	-0.096
	253	2	-0.019
	254	2	-0.140
	256	2	-0.044
	286	2	-0.127
	287	2	-0.085
Holey Triangular Graphene 3	289*	3	-0.004
	315	2	-0.080
	316	2	-0.040
	318	2	-0.084
	346	2	-0.075
	347	2	-0.083
	349	2	-0.135
	381	2	-0.035
	382	2	-0.038
	384	2	-0.085
	420*	3	+0.057

Table B.3 The atom numbers (2nd column), the nearest neighbors (3rd column), and the net charge (4th column) of atoms at the boundary of the holey triangular graphene 3.

Figure B.4 Relaxed holey triangular graphene 4 near the hole area. The numbers identify the different atoms.

Structures	Atom #	Nearest Neighbors	Charge (e)
	135*	2	-0.045
	138	2	-0.052
	174	2	-0.051
	175	2	-0.121
	177	2	-0.083
	209	2	-0.119
	210	2	-0.129
	212	2	-0.085
	240	2	-0.084
	241	2	-0.118
	243	2	-0.053
Holey Triangular Graphene 4	267	2	-0.130
	268*	2	-0.040
	291	2	-0.084
	292	2	-0.053
	316	2	-0.119
	317	2	-0.085
	319	2	-0.118
	345	2	-0.051
	346	2	-0.083
	348	2	-0.129
	379*	2	-0.045
	380	2	-0.052
	382	2	-0.121

Table B.4 The atom numbers (2nd column), the nearest neighbors (3rd column), and the net charge (4th column) of atoms at the boundary of the holey triangular graphene 4.

Figure B.5 Relaxed holey triangular graphene 5 near the hole area. The numbers identify the different atoms.

Structures	Atom #	Nearest Neighbors	Charge (e)
Holey Triangular Graphene 5	94*	3	+0.005
	134	2	-0.085
	135	2	-0.077
	137	2	-0.036
	173	2	-0.043
	174	2	-0.043
	176	2	-0.086
	208	2	-0.137
	209	2	-0.129
	211	2	-0.082
	239	2	-0.084
	240	2	-0.134
	242	2	-0.043
	266	2	-0.129
	267	2	-0.079
	269*	3	+0.008
	289	2	-0.087
	290	2	-0.044
	292	2	-0.079
	314	2	-0.136
	315	2	-0.081
	317	2	-0.134

	343	2	-0.038
	344	2	-0.089
	346	2	-0.129
	376	2	-0.083
	377	2	-0.031
	379	2	-0.136
	413*	3	+0.008
	415	2	-0.076

Table B.5 The atom numbers (2nd column), the nearest neighbors (3rd column), and the net charge (4th column) of atoms at the boundary of the holey triangular graphene 5.

Figure B.6 Relaxed holey circular graphene 1 near the hole area. The numbers identify the different atoms.

Structures	Atom #	Nearest Neighbors	Charge (e)
Holey Circular Graphene 1	258	2	-0.041
	259	2	-0.049
	260	2	-0.05
	261	2	-0.045
	295	2	-0.040
	296	2	-0.043
	329	2	-0.043
	330	2	-0.045
	331	2	-0.041
	332	2	-0.040
	368	2	-0.050
	369	2	-0.049

Table B.6 The atom numbers (2nd column), the nearest neighbors (3rd column), and the net charge (4th column) of atoms at the boundary of the holey circular graphene 1.

Figure B.7 Relaxed holey circular graphene 2 near the hole area. The numbers identify the different atoms.

Structures	Atom #	Nearest Neighbors	Charge (e)
	217*	2	-0.010
	218	2	-0.073
	219	2	+0.085
	220*	2	-0.055
	251	2	+0.085
	252	2	-0.080
	253	2	-0.070
	254	2	+0.049
Holey Circular Graphene 2	282*	2	-0.108
	283*	2	-0.020
	311	2	+0.089
	312	2	+0.059
	342	2	-0.080
	343	2	-0.065
	375*	2	-0.007
	378	2	-0.074
	379	2	-0.084
	382*	2	-0.064

Table B.7 The atom numbers (2nd column), the nearest neighbors (3rd column), and the net charge (4th column) of atoms at the boundary of the holey circular graphene 2.
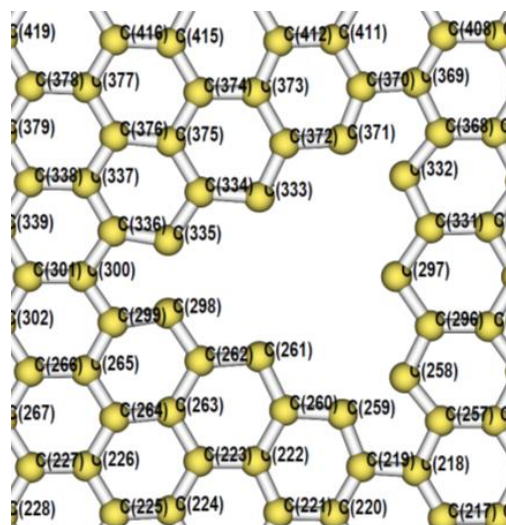
Figure B.8 Relaxed holey circular graphene 3 near the hole area. The numbers identify the different atoms.

Structures	Atom #	Nearest Neighbors	Charge (e)
	178	2	-0.067
	179	2	+0.069
	182	2	+0.069
	183	2	-0.067
	215	2	+0.071
	216	2	-0.067
	217	2	-0.066
	218	2	+0.071
	246	2	+0.070
	247	2	+0.070
	273	2	-0.067
	274	2	-0.067
Holey Circular Graphene 3	299	2	-0.067
	300	2	+0.070
	301	2	+0.070
	302	2	-0.067
	329	2	+0.071
	330	2	+0.071
	360	2	-0.066
	361	2	-0.066
	362	2	+0.069
	363	2	+0.069
	364	2	-0.067
	365	2	-0.067

Table B.8 The atom numbers (2nd column), the nearest neighbors (3rd column), and the net charge (4th column) of atoms at the boundary of the holey circular graphene 3.
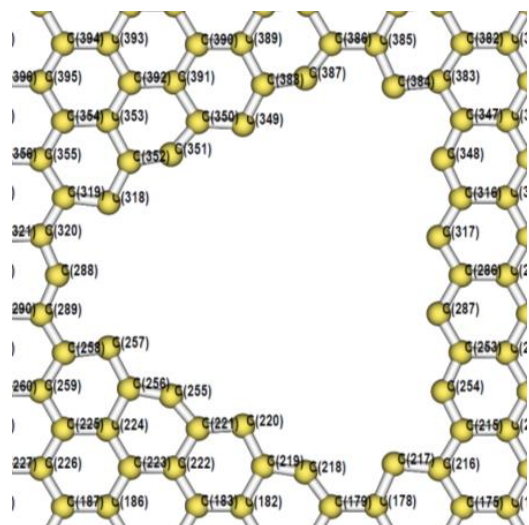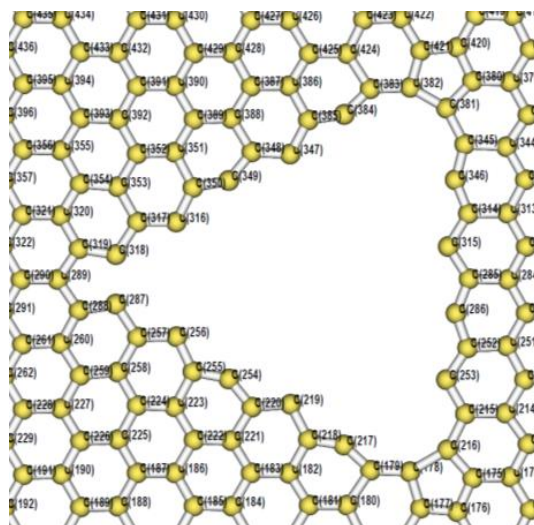
Figure B.9 Relaxed holey circular graphene 4 near the hole area. The numbers identify the different atoms.

Structures	Atom #	Nearest Neighbors	Charge (e)
	135*	2	-0.036
	138	2	-0.061
	139	2	+0.071
	142	2	+0.071
	143	2	-0.062
	146*	2	-0.036
	174	2	-0.062
	175	2	-0.061
	201	2	+0.076
	202	2	+0.074
	225	2	-0.063
	226	2	+0.069
	227	2	+0.072
	228	2	-0.062
Holey Circular Graphene 4	248*	2	-0.037
	249*	2	-0.029
	269	2	-0.063
	270	2	-0.062
	292	2	+0.069
	293	2	+0.072
	317	2	+0.076
	318	2	-0.061
	319	2	-0.061
	320	2	+0.074
	347*	2	-0.036
	348	2	-0.061

	349	2	+0.072
	350	2	+0.071
	351	2	-0.061
	352*	2	-0.035

Table B.9 The atom numbers (2nd column), the nearest neighbors (3rd column), and the net charge (4th column) of atoms at the boundary of the holey circular graphene 4.
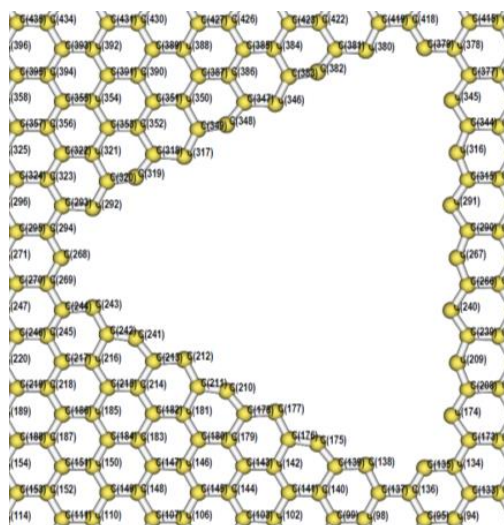

Figure B.10 Relaxed holey rectangular 1 near the hole area. The numbers identify the different atoms.

Structures	Atom #	Nearest Neighbors	Charge (e)
	258*	3	+0.040
	259	2	-0.087
	262	2	-0.024
	263*	3	+0.044
Holey Rectangular Graphene 1	298	2	-0.024
	299	2	-0.086
	334*	3	+0.040
	335	2	-0.087
	336	2	-0.026
	337*	3	+0.045

Table B.10 The atom numbers (2nd column), the nearest neighbors (3rd column), and the net charge (4th column) of atoms at the boundary of the holey rectangular graphene 1.

Figure B.11 Relaxed holey rectangular graphene 2_2nd near the hole area. The numbers identify the different atoms.

Structures	Atom #	Nearest Neighbors	Charge (e)
	218*	3	+0.036
	219	2	-0.010
	222	2	-0.087
	223*	3	+0.036
	258	2	-0.112
	259	2	-0.048
Holey Rectangular graphene 2_2nd	294	2	-0.049
	295	2	-0.129
	330	2	-0.112
	331	2	-0.047
	366*	3	+0.036
	367	2	-0.010
	368	2	-0.087
	369*	3	+0.037

Table B.11 The atom numbers (2nd column), the nearest neighbors (3rd column), and the net charge (4th column) of atoms at the boundary of the holey rectangular graphene 2_2nd.
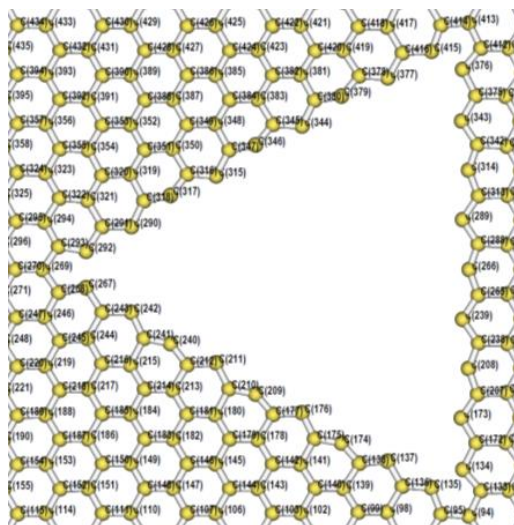
Figure B.12 Relaxed holey rectangular graphene 3 near the hole area. The numbers identify the different atoms.

Structures	Atom #	Nearest Neighbors	Charge (e)
	256*	3	+0.041
	257	2	-0.101
	258	2	+0.096
	259	2	-0.080
	260	2	-0.003
	261*	3	+0.037
	292	2	-0.051
Holey Rectangular Graphene 3	293	2	-0.109
	324	2	-0.109
	325	2	-0.045
	356*	3	+0.037
	357	2	-0.001
	360	2	-0.076
	361	2	+0.099
	364	2	-0.096
	365*	3	+0.040

Table B.12 The atom numbers (2nd column), the nearest neighbors (3rd column), and the net charge (4th column) of atoms at the boundary of the holey rectangular graphene 3.
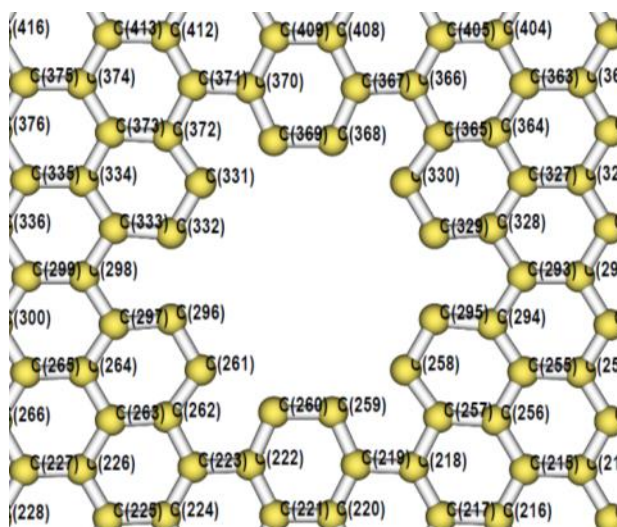
Figure B.13 Relaxed holey rectangular graphene 4_2nd near the hole area. The numbers identify the different atoms.

Structures	Atom #	Nearest Neighbors	Charge (e)
	216*	3	+0.040
	217	2	-0.098
	218	2	+0.096
	219	2	-0.076
	220	2	-0.004
	221*	3	+0.038
	252	2	-0.057
	253	2	-0.092
	284	2	-0.136
	285	2	-0.100
Holey Rectangular Graphene 4_2nd	316	2	-0.095
	317	2	-0.101
	348	2	-0.099
	349	2	-0.092
	380*	3	+0.044
	381	2	-0.044
	384	2	+0.095
	385	2	-0.060
	388	2	-0.016
	389*	3	+0.039

Table B.13 The atom numbers (2nd column), the nearest neighbors (3rd column), and the net charge (4th column) of atoms at the boundary of the holey rectangular graphene 4_2nd.
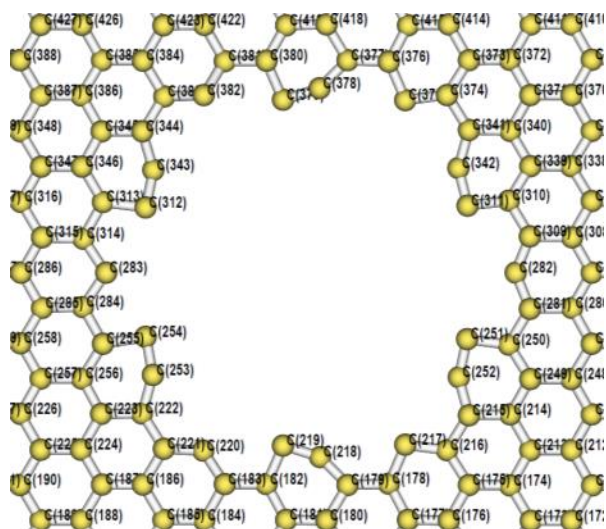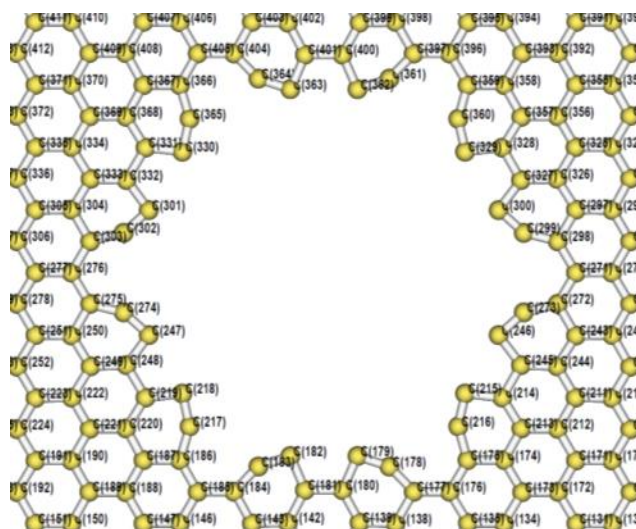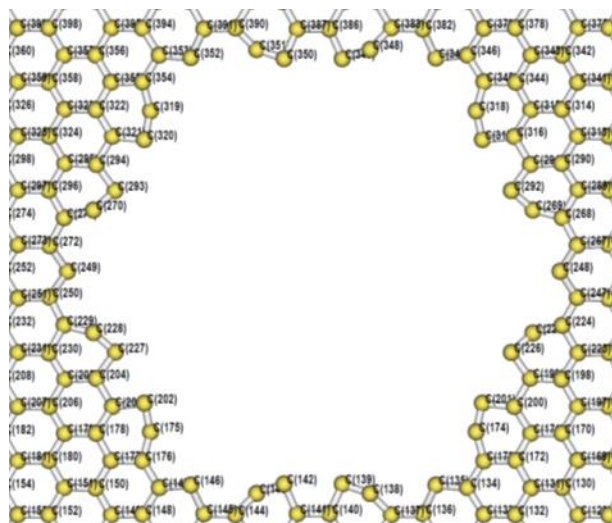
Figure B.14 Relaxed holey rectangular graphene 5 near the hole area. The numbers identify the different atoms.

Structures	Atom #	Nearest Neighbors	Charge (e)
	214*	3	+0.036
	215	2	-0.006
	218	2	-0.061
	219	2	+0.079
	222	2	+0.079
	223	2	-0.061
	226	2	-0.006
	227*	3	+0.036
	254	2	-0.115
	255	2	-0.115
	282	2	-0.064
	283	2	-0.064
Holey Rectangular Graphene 5	310	2	-0.113
	311	2	-0.113
	338*	3	+0.036
	339	2	-0.011
	340	2	-0.060
	341	2	+0.078
	342	2	+0.078
	343	2	-0.060
	344	2	-0.011
	345*	3	+0.036

Table B.14 The atom numbers (2nd column), the nearest neighbors (3rd column), and the net charge (4th column) of atoms at the boundary of the holey rectangular graphene 5.

<u>Figure B.15</u> Relaxed holey rectangular graphene 6 near the hole area. The numbers identify the different atoms.

Structures	Atom #	Nearest Neighbors	Charge (e)
	212*	3	+0.034
	213	2	-0.023
	214	2	-0.073
	215	2	+0.049
	216	2	+0.059
	217	2	+0.040
	218	2	+0.051
	219	2	-0.074
	220	2	-0.021
	221*	3	+0.035
	244	2	-0.071
	245	2	-0.073
	268	2	-0.130
	269	2	-0.128
Holey Rectangular Graphene 6	292	2	-0.100
	293	2	-0.100
	316	2	-0.104
	317	2	-0.103
	340*	3	+0.039
	341	2	-0.015
	344	2	-0.068
	345	2	+0.058
	348	2	+0.021
	349	2	+0.078
	352	2	+0.053
	353	2	-0.065

| | 356 | 2 | -0.017 |
| | 357* | 3 | +0.039 |

Table B.15 The atom numbers (2nd column), the nearest neighbors (3rd column), and the net charge (4th column) of atoms at the boundary of the holey rectangular graphene 6.
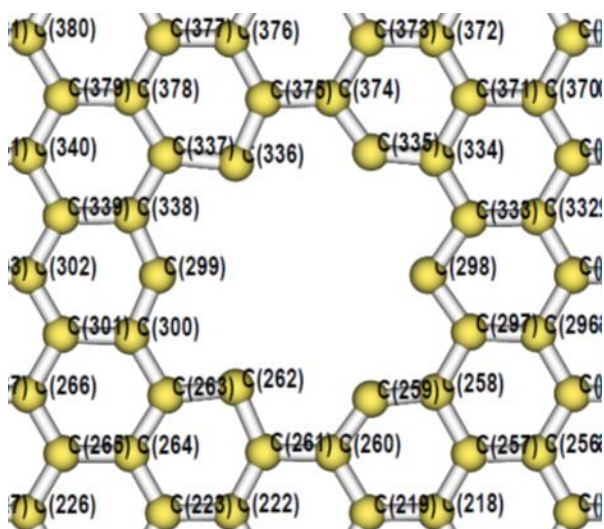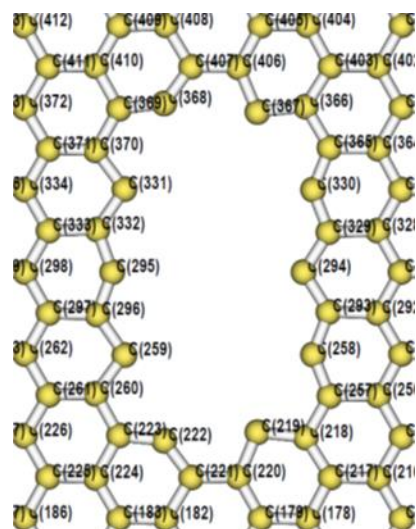

Figure B.16 Relaxed holey graphene 7_2nd near the hole area. The numbers identify the different atoms.

Structure	Atom #	Nearest Neighbors	Charge (e)
	172*	3	+0.039
	173	2	-0.008
	174	2	-0.060
	175	2	+0.060
	176	2	+0.086
	177	2	+0.065
	178	2	+0.095
	179	2	-0.065
	180	2	-0.007
	181*	3	+0.038
	204	2	-0.093
	205	2	-0.094
Holey Rectangular Graphene 7_2nd	228	2	-0.085
	229	2	-0.084
	252	2	-0.095
	253	2	-0.095
	276	2	-0.117
	277	2	-0.117
	300	2	-0.075
	301	2	-0.076

	324	2	-0.108
	325	2	-0.108
	348*	3	+0.038
	349	2	-0.007
	352	2	-0.066
	353	2	+0.094
	356	2	-0.070
	357	2	+0.070
	360	2	+0.084
	361	2	-0.060
	364	2	-0.009
	365*	3	+0.039

Table B.16 The atom numbers (2nd column), the nearest neighbors (3rd column), and the net charge (4th column) of atoms at the boundary of the holey rectangular graphene 7_2nd.
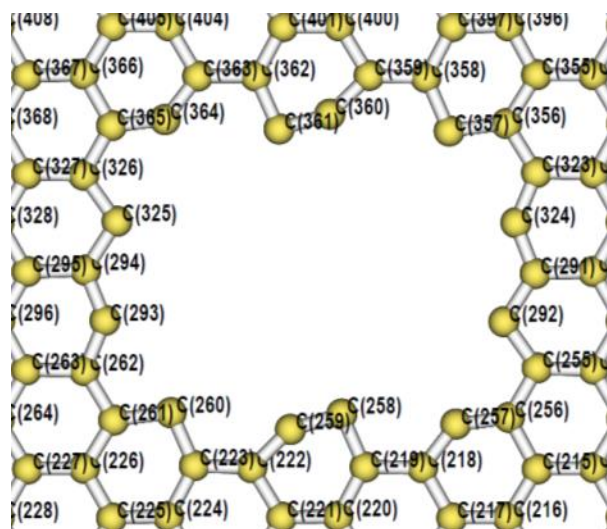

Figure B.17 Holey rectangular graphene 8 near the hole area. The numbers identify the different atoms.

Structure	Atom #	Nearest Neighbors	Charge (e)
	170*	3	+0.042
	171	2	-0.025
	174	2	-0.060
	175	2	+0.084
	178	2	+0.076
	179	2	-0.062
	182	2	-0.061
	183	2	+0.076
	186	2	+0.086
	187	2	-0.060

	190	2	-0.017
	191*	3	+0.042
	210	2	-0.099
	211	2	-0.105
	230	2	-0.092
	231	2	-0.092
Holey Rectangular Graphene 8	250	2	-0.133
	251	2	-0.136
	270	2	-0.095
	271	2	-0.095
	290	2	-0.095
	291	2	-0.097
	310*	3	+0.043
	311	2	-0.029
	312	2	-0.061
	313	2	+0.083
	314	2	+0.077
	315	2	-0.062
	316	2	-0.062
	317	2	+0.077
	318	2	+0.083
	319	2	-0.061
	320	2	-0.027
	321*	3	+0.043

Table B.17 The atom numbers (2nd column), the nearest neighbors (3rd column), and the net charge (4th column) of atoms at the boundary of the holey rectangular graphene 8.
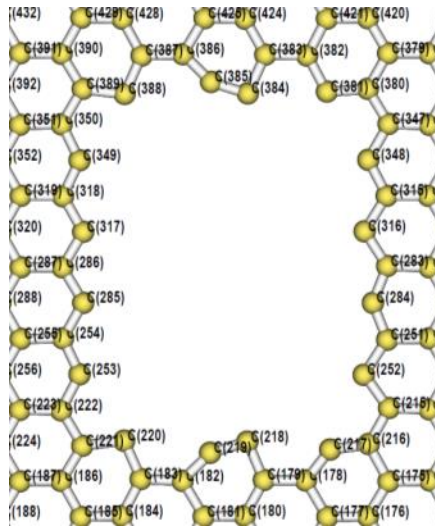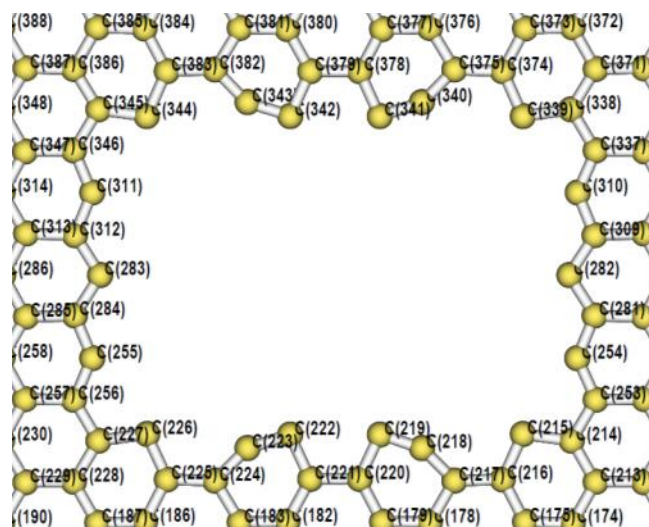
Figure B.18 Holey rectangular graphene 9_2nd near the hole area. The numbers identify the different atoms.

Structure	Atom #	Nearest Neighbors	Charge (e)
	130*	3	+0.034
	131	2	-0.023
	134	2	-0.069
	135	2	+0.080
	138	2	+0.079
	139	2	-0.063
	142	2	-0.063
	143	2	+0.079
	146	2	+0.080
	147	2	-0.069
	150	2	-0.023
	151*	3	+0.034
	170	2	-0.061
	171	2	-0.061
	190	2	-0.113
	191	2	-0.113
Holey Rectangular Graphene 9_2nd	210	2	-0.088
	211	2	-0.088
	230	2	-0.126
	231	2	-0.125
	250	2	-0.088
	251	2	-0.089
	270	2	-0.112
	271	2	-0.112
	290	2	-0.061
	291	2	-0.061

310*	3	+0.034
311	2	-0.023
312	2	-0.070
313	2	+0.080
314	2	+0.079
315	2	-0.063
316	2	-0.063
317	2	+0.079
318	2	+0.080
319	2	-0.069
320	2	-0.022
321*	3	+0.035

Table B.18 The atom numbers (2nd column), the nearest neighbors (3rd column), and the net charge (4th column) of atoms at the boundary of the holey rectangular graphene 9_2nd.
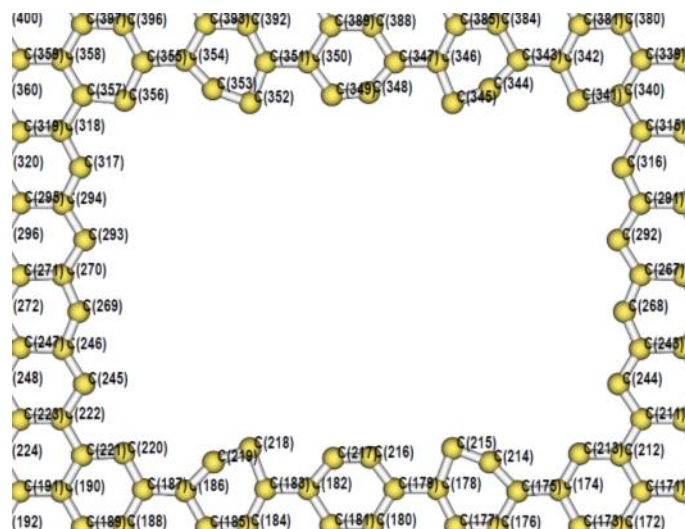

Figure B.19 Relaxed holey rectangular graphene 10 near the hole area. The numbers identify the different atoms.

Structure	Atom #	Nearest Neighbors	Charge (e)
	168*	3	+0.038
	169	2	-0.006
	170	2	-0.059
	171	2	+0.098
	172	2	+0.043
	173	2	-0.070
	174	2	+0.054
	175	2	+0.053
	176	2	-0.070
	177	2	+0.043

	178	2	+0.098
	179	2	-0.059
	180	2	-0.007
	181*	3	+0.038
	196	2	-0.102
	197	2	-0.105
	212	2	-0.077
	213	2	-0.075
Holey Rectangular Graphene 10	244	2	-0.104
	245	2	-0.099
	260	2	-0.077
	261	2	-0.080
	276	2	-0.098
	277	2	-0.095
	292*	3	+0.039
	293	2	-0.010
	296	2	-0.066
	297	2	+0.095
	300	2	-0.075
	301	2	+0.072
	304	2	+0.076
	305	2	-0.062
	308	2	-0.062
	309	2	+0.063
	312	2	+0.088
	313	2	-0.061
	316	2	-0.009
	317*	3	+0.039

Table B.19 The atom numbers (2nd column), the nearest neighbors (3rd column), and the net charge (4th column) of atoms at the boundary of the holey rectangular graphene 10.
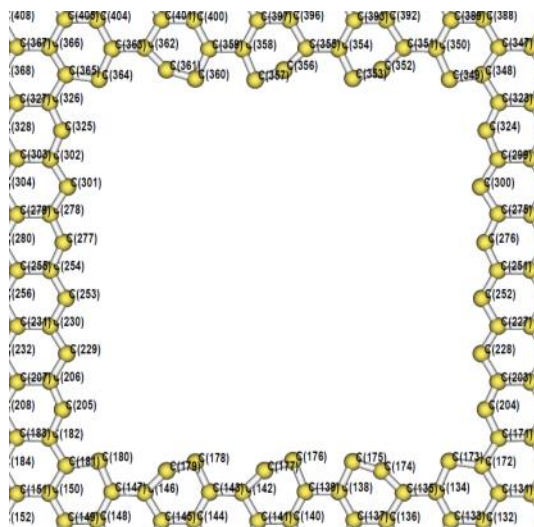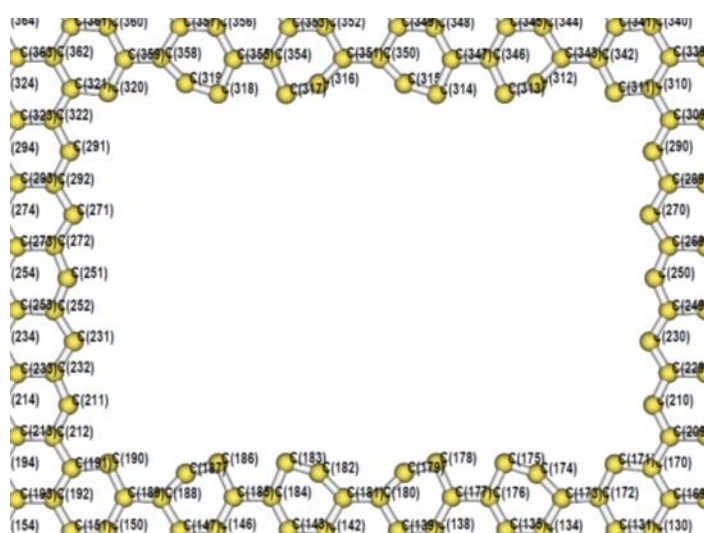
Figure B.20 Relaxed holey rectangular graphene 11_2nd near the hole area. The numbers identify the different atoms.

Structure	Atom #	Nearest Neighbors	Charge (e)
	128*	3	+0.042
	129	2	-0.019
	130	2	-0.055
	131	2	+0.096
	132	2	+0.053
	133	2	-0.071
	134	2	+0.059
	135	2	+0.054
	136	2	-0.070
	137	2	+0.053
	138	2	+0.098
	139	2	-0.055
	140	2	-0.014
	141*	3	+0.040
	156	2	-0.107
Holey Rectangular Graphene 11_2nd	157	2	-0.104
	172	2	-0.092
	173	2	-0.092
	188	2	-0.123
	189	2	-0.121
	204	2	-0.086
	205	2	-0.085
	220	2	-0.086
	221	2	-0.085
	236	2	-0.123
	237	2	-0.121

	Atom #	Nearest Neighbors	Charge (e)
	252	2	-0.092
	253	2	-0.092
	268	2	-0.107
	269	2	-0.104
	284*	3	+0.042
	285	2	-0.019
	288	2	-0.055
	289	2	+0.096
	292	2	+0.053
	293	2	-0.071
	296	2	+0.056
	297	2	+0.058
	300	2	-0.070
	301	2	+0.052
	304	2	+0.098
	305	2	-0.054
	308	2	-0.014
	309*	3	+0.040

Table B.20 The atom numbers (2nd column), the nearest neighbors (3rd column), and the net charge (4th column) of atoms at the boundary of the holey rectangular graphene 11_2nd.
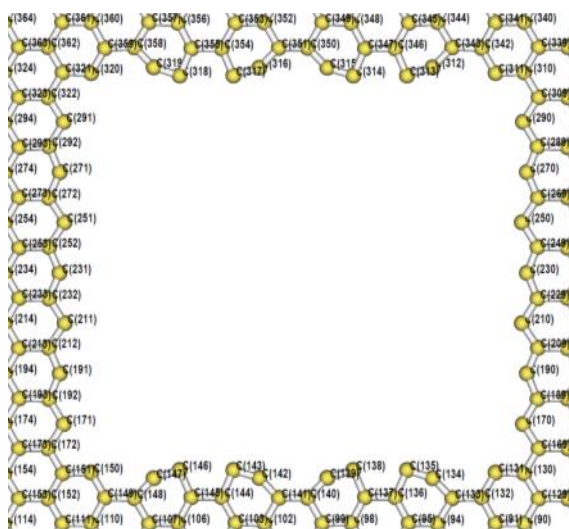

Figure B.21 Relaxed holey rectangular graphene 2_1st near the hole area. The numbers identify the different atoms.

Structure	Atom #	Nearest Neighbors	Charge (e)
	218*	3	-0.018
	219	3	+0.046
	222	3	+0.052
	223*	3	-0.003

Structure	Atom #	Nearest Neighbors	Charge (e)
Holey Rectangular Graphene 2_1st	258	2	-0.099
	259	2	-0.041
	260	2	-0.072
	261	2	-0.054
	296	2	+0.014
	297	2	-0.090
	332	2	-0.099
	333	2	-0.053
	368*	3	-0.018
	369	3	+0.046
	370	2	-0.041
	371	2	-0.071
	372	3	+0.052
	373*	3	-0.003

Table B.21 The atom numbers (2nd column), the nearest neighbors (3rd column), and the net charge (4th column) of atoms at the boundary of the holey rectangular graphene 2_1st.
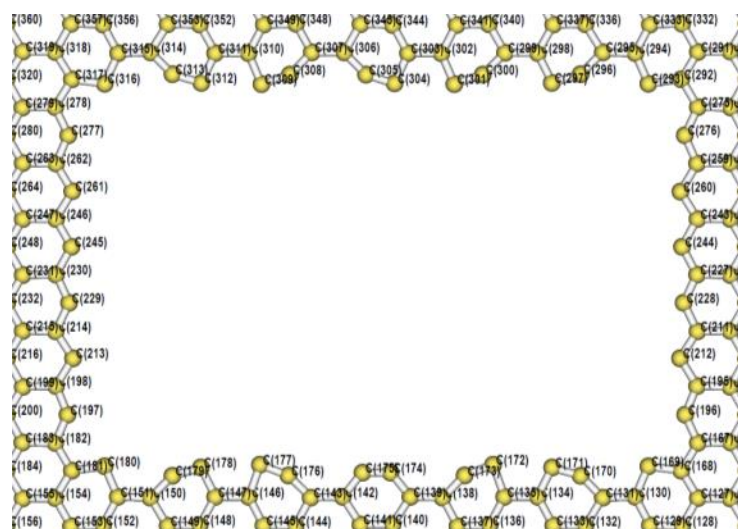

Figure B.22 Holey rectangular graphene 4_1st near the hole area. The numbers identify the different atoms.

Structure	Atom #	Nearest Neighbors	Charge (e)
	216*	3	-0.031
	217	3	+0.054
	218	2	-0.073
	219	2	+0.140
	220	3	-0.081
	221	3	+0.028
	222	2	-0.141
	223	2	-0.010

	224	3	+0.016
	225*	3	+0.001
	256	2	-0.053
	257	2	-0.109
	288	2	-0.132
Holey Rectangular Graphene 4_1st	289	2	-0.025
	320	2	-0.025
	321	2	-0.132
	352	2	-0.106
	353	2	-0.012
	354	2	-0.142
	355	2	+0.142
	356	2	-0.072
	357	2	-0.052
	388*	3	+0.003
	389	3	+0.015
	392	3	+0.029
	393	3	-0.083
	396	3	+0.052
	397*	3	-0.031

Table B.22 The atom numbers (2nd column), the nearest neighbors (3rd column), and the net charge (4th column) of atoms at the boundary of the holey rectangular graphene 4_1^{st}.
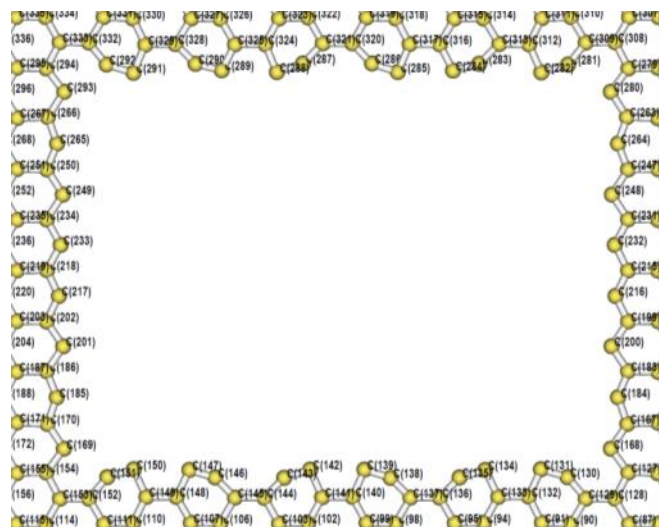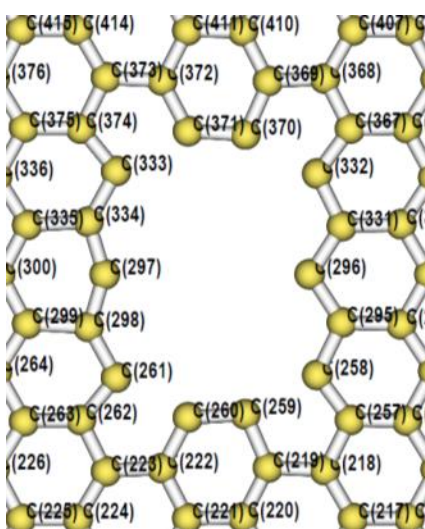

Figure B.23 Holey rectangular graphene 7_1^{st} near the hole area. The numbers identify the different atoms.

153

Structure	Atom #	Nearest Neighbors	Charge (e)
	172*	3	+0.005
	173	3	+0.013
	174	2	-0.018
	175	2	-0.140
	176	3	+0.037
	177	3	-0.087
	178	2	+0.137
	179	2	-0.048
	180	3	+0.012
	181	3	-0.050
	182	2	+0.118
	183	2	-0.025
	184	3	-0.002
	185	3	+0.011
	186	2	-0.049
	187	2	+0.037
	188	3	+0.055
	189*	3	+0.026
	212	2	-0.097
	213	2	-0.085
	236	2	-0.009
	237	2	-0.110
Holey Rectangular Graphene 7_1st	260	2	-0.116
	261	2	-0.101
	284	2	-0.081
	285	2	-0.135
	308	2	-0.039
	309	2	-0.044
	332	2	-0.118
	333	2	+0.032
	334	2	-0.111
	335	2	+0.123
	336	2	-0.075
	337	2	+0.117
	338	2	-0.026
	339	2	-0.040
	340	2	+0.030
	341	2	-0.102
	364*	3	-0.015
	365	3	-0.005
	368	3	+0.036
	369	3	-0.069
	372	3	+0.029
	373	3	-0.055

	376	3	-0.003
	377	3	+0.007
	380	3	+0.053
	381*	3	+0.012

Table B.23 The atom numbers (2nd column), the nearest neighbors (3rd column), and the net charge (4th column) of atoms at the boundary of the holey rectangular graphene 7_1st.
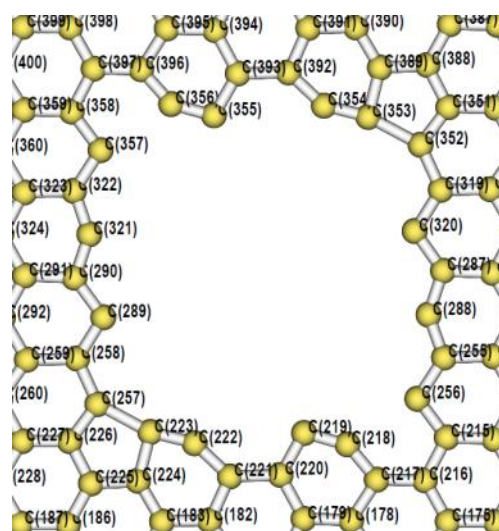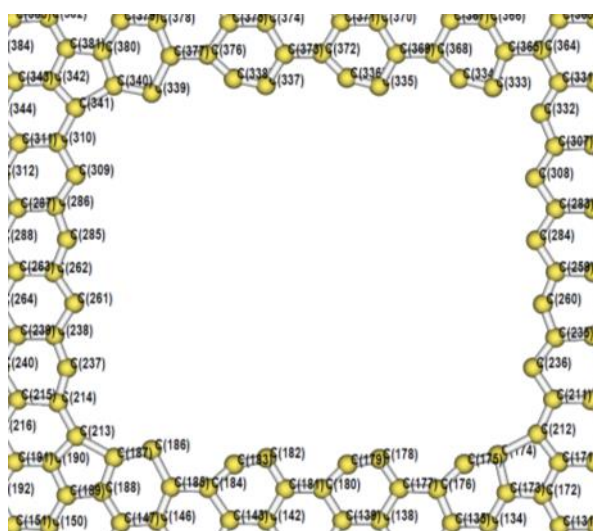

Figure B.24 Relaxed holey rectangular graphene 9_1st near the hole area. The numbers identify the different atoms.

Structure	Atom #	Nearest Neighbors	Charge (e)
	130*	3	-0.025
	131	3	+0.048
	134	3	-0.035
	135	3	-0.043
	138	3	+0.008
	139	3	+0.024
	142	3	-0.029
	143	3	-0.045
	146	3	+0.026
	147	3	-0.051
	150	3	+0.051
	151*	3	-0.023
	170	2	-0.044
	171	2	-0.055
	172	2	+0.084
	173	2	+0.091
	174	2	-0.051
	175	2	-0.063

Holey Rectangular Graphene 9_1st	176	2	+0.064
	177	2	+0.103
	178	2	-0.055
	179	2	+0.087
	180	2	-0.062
	181	2	-0.045
	200	2	-0.132
	201	2	-0.125
	220	2	-0.097
	221	2	-0.094
	240	2	-0.149
	241	2	-0.145
	260	2	-0.100
	261	2	-0.098
	280	2	-0.135
	281	2	-0.125
	300	2	-0.046
	301	2	-0.053
	320*	3	-0.024
	321	3	+0.052
	322	2	-0.063
	323	2	+0.088
	324	3	-0.051
	325	3	+0.027
	326	2	-0.056
	327	2	+0.102
	328	3	-0.045
	329	3	-0.029
	330	2	+0.065
	331	2	-0.062
	332	3	+0.023
	333	3	+0.009
	334	2	-0.052
	335	2	+0.089
	336	3	-0.042
	337	3	-0.037
	338	2	+0.084
	339	2	-0.056
	340	3	+0.047
	341*	3	-0.026

Table B.24 The atom numbers (2nd column), the nearest neighbors (3rd column), and the net charge (4th column) of atoms at the boundary of the holey rectangular graphene 9_1st.
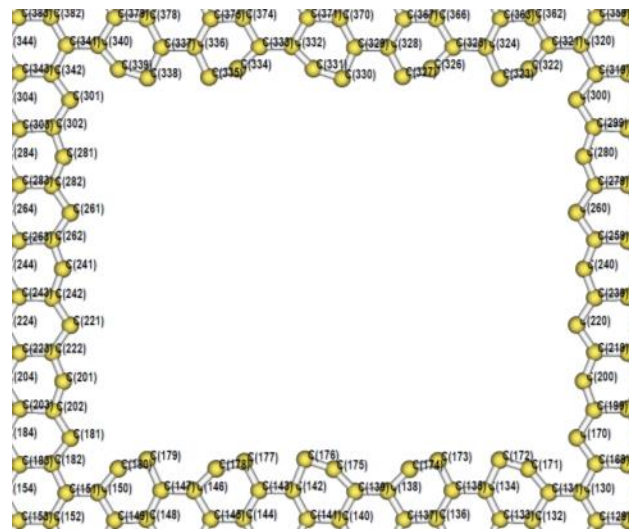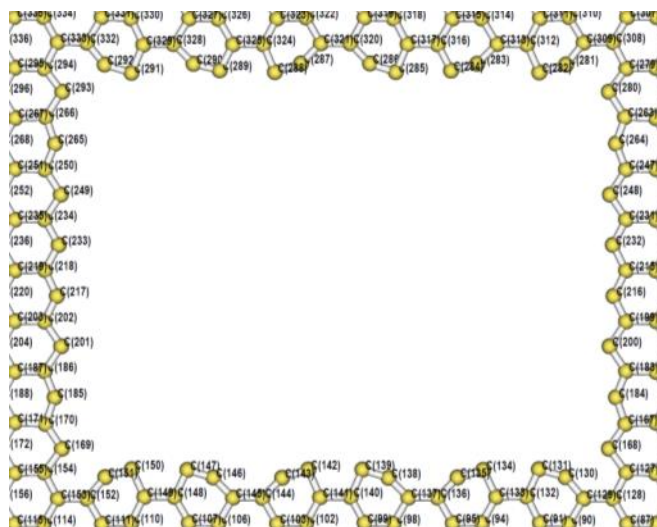
Figure B.25 Holey rectangular graphene 11_1st near the hole area. The numbers identify the different atoms.

Structure	Atom #	Nearest Neighbors	Charge (e)
	128*	3	-0.037
	129	3	+0.056
	130	2	-0.064
	131	2	+0.084
	132	3	-0.035
	133	3	-0.043
	134	2	+0.083
	135	2	-0.055
	136	3	+0.012
	137	3	+0.020
	138	2	-0.067
	139	2	+0.077
	140	3	-0.036
	141	3	-0.037
	142	2	+0.077
Holey Rectangular Graphene 11_1st	143	2	-0.066
	144	3	+0.020
	145	3	+0.013
	146	2	-0.056
	147	2	+0.082
	148	3	-0.042
	149	3	-0.036
	150	2	+0.085
	151	2	-0.064
	152	3	+0.055
	153*	3	-0.037

168	2	-0.056
169	2	-0.056
184	2	-0.132
185	2	-0.133
200	2	-0.088
201	2	-0.092
216	2	-0.099
217	2	-0.102
232	2	-0.090
233	2	-0.089
248	2	-0.094
249	2	-0.090
264	2	-0.128
265	2	-0.127
280	2	-0.060
281	2	-0.070
282	2	+0.083
283	2	-0.059
284	2	+0.100
285	2	+0.065
286	2	-0.063
287	2	-0.063
288	2	+0.064
289	2	+0.102
290	2	-0.057
291	2	+0.082
292	2	-0.069
293	2	-0.056
308*	3	-0.036
309	3	+0.060
312	3	-0.049
313	3	+0.026
316	3	-0.044
317	3	-0.029
320	3	+0.018
321	3	+0.018
324	3	-0.028
325	3	-0.045
328	3	+0.024
329	3	-0.047
332	3	+0.061
333*	3	-0.036

Table B.25 The atom numbers (2nd column), the nearest neighbors (3rd column), and the net charge (4th column) of atoms at the boundary of the holey rectangular graphene 11_1st.

CURRICULUM VITAE

Name: Cherno Baba Kah

Address: 15826 Wisteria Hill Street, Houston Texas 77073.

Department of Physics and Astronomy, University of Louisville.

Telephone: 1-502-310-3676

Email: cbkah001@louisville.edu

chernobaba@gmail.com

Education: Doctoral Candidate 08/2013 – Expected to graduate 08/2106

Department of Physics and Astronomy, University of Louisville, Louisville, Kentucky

Masters of Science in Physics 2013

Department of Physics and Astronomy, University of Louisville, Louisville, Kentucky

Masters of Science in Physics 2011

Department of Physics, Clark Atlanta University, Atlanta Georgia

Bachelors of Science in Physics/Chemistry 2009

Department of Science and Technology, University of The Gambia, The Gambia

University Experience: University of Louisville

Graduate Teaching Assistant 08/2014 – 07/2015

Taught introductory Physics Laboratory courses to undergraduate students in science and engineering. Grading and also taught some large classes on behalf of a professor.

Graduate Research Assistant 08/2011 – Present

Condensed Matter Theory Group:

- Investigate structural and electronic properties of Boron nanomaterials,

- Band gap engineering in both hexagonal BN and graphene and

- Construction of new sets of Nitrogen Parameters for our Semi Empirical method (SCED – LCAO)

Clark Atlanta University

Graduate Teaching Assistant 08/2009 – 05/2011

Taught introductory Physics Laboratory courses to non-physics undergraduate students.

Graduate Research Assistant 08/2009 – 07/2011

Center for Functional and Nanoscale Materials

- Investigated structural and electronic stability of stuffed C80 fullerene

- Effects of dispersion correction on Boron fullerenes and nanotubes

University of The Gambia

Graduate Assistant 09/2007 – 07/2009

- Tutored Physics courses to Physics major students and Calculus to first and second year science students.

- Physics and Mathematics instructor to pre-university students who were planning to major in Physics or Mathematics

- Mathematics instructor to high school graduates who did not have the required grades in mathematics to be accepted in the university and were supposed to retake the entry exam.

Research Assistant 09/2006 – 07/2009

Data collection using NilUV instrument to investigate UV radiation from the sun. This was done in collaboration with the University of Bergen in Norway.

Publications:

1. Low dimensional Boron Structures based on Icosahedron B12; C. B. Kah, M. Yu, P. Tandy, C. S. Jayanthi and S. Y. Wu; **Nanotechnology** 26 (2015) 405701

2. Icosahedra Boron chain and sheets: new boron allotropic structures; C. B. Kah, M. Yu, P. Tandy, C. S. Jayanthi and S. Y. Wu; **arXiv:1409.7457v1** [cond-mat.mtrl-sci]

3. Dispersion Corrections in the Boron buckyball and nanotubes; R. N. Gunasinghe, C. B. Kah, K. D. Quarles and X. Q. Wang; **Appl. Phys. Lett.** 98 (2011) 261906

4. Filled Pentagons and Electron Counting Rule for Boron Fullerenes; K. D. Quarles, C. B. Kah; R. N. Gunasinghe; R. N. Musin and X. Q. Wang; J. **Chem. Theo. Comp.** 2011 7 (7), pp 2017–2020

5. Electronic shell structures of Russian-doll-style Sc4C2@C80; Z. Chen, C. B. Kah and X. Q. Wang; **Chem. Phys. Letters**, 506 2011 (230-232)

6. Structural and Electronic Stability of Russian-Doll-Structured Sc4C2@C80; C. B. Kah, J. Nathaniel, K. Suggs and X. Q. Wang; **J. Phys. Chem. C**, 2010 114 (30)

Presentations and Conferences:

1. Structural and Electronic Properties of a single layered α-tetragonal B_{50} sheet C. B. Kah, M. Yu, C. S. Jayanthi and S. Y. Wu; Graduate Student Council Regional Research Conference, University of Louisville, April 2, 2016

2. Structural Stability and Electronic Properties of a single layered α-tetragonal B_{50} sheet C. B. Kah, M. Yu, C. S. Jayanthi and S. Y. Wu; APS March Meeting, Baltimore MD, 2016

3. Graphene islands embedded in hexagonal Boron-Nitride sheet: structural and electronic properties study; C. B. Kah, S. Kirigeehanage, L. Smith, M. Yu, C. S. Jayanthi and S. Y. Wu; APS March Meeting, San Antonio TX, 2015 F17.00008

4. Structural Stability and Electronic Properties of Decorated Two-Dimensional Sheets of Icosahedral B12 Units: A Molecular Dynamics Study. C. B. Kah, M. Yu, C. S. Jayanthi and S. Y. Wu GEM Grad Lab hosted by SIGS of Uni. Of Louisville September 19 2014

5. Structural Stability and Electronic Properties of Two-Dimensional Boron α-B12 Structures. C. B. Kah, M. Yu, C. S. Jayanthi and S. Y. Wu; APS March Meeting, Denver CO, 2014

6. The Structure, Stability and Electronic Properties of a One-Dimensional Boron α-B12 Structure. C. B. Kah; P. Tandy; M. Yu; C. S. Jayanthi and S. Y. Wu; APS March Meeting, Baltimore MD, 2013

Honors and Awards

- Doctoral Dissertation Completion Award Summer 2016 University of Louisville, Louisville KY 06/2016 – 08/2016

- Dillon Fellowship from the Department of Physics and Astronomy, University of Louisville, Louisville KY 08/2015 – 05/2016

- Graduate Teaching Assistantship, Department of Physics and Astronomy, University of Louisville, Louisville KY 08/2014 – 07/2015

- McSweeney Fellowship, School of Arts and Sciences, University of Louisville, Louisville KY 08/2011 – 07/2014

- Graduate Teaching Assistantship from Department of Physics, Clark Atlanta University, Atlanta GA 08/2009 – 07/2011

- Graduate Assistantship from the University of The Gambia, The Gambia 09/2007 – 07/2009

- Gambian Government Award, Government of The Gambia 09/2003 – 07/2007

- Organisation Internationale de la Francophonie Award 07/2002

Language Skills:

English (fluent), French (fluent), Fulani (native), Wolof (fluent), Arabic (reading)